

Optically Visible Post-AGB Stars, Post-RGB Stars and Young Stellar Objects in the Large Magellanic Cloud

D. Kamath^{1*}, P. R. Wood² and H. Van Winckel¹

¹*Instituut voor Sterrenkunde, K.U.Leuven, Celestijnenlaan 200D bus 2401, B-3001 Leuven, Belgium*

²*Research School of Astronomy and Astrophysics, Mount Stromlo Observatory, Weston Creek, ACT 2611, Australia*

Accepted ... Received ...; in original form 2012 February 1

ABSTRACT

We have carried out a search for optically visible post-Asymptotic Giant Branch (post-AGB) stars in the Large Magellanic Cloud (LMC). First, we selected candidates with a mid-IR excess and then obtained their optical spectra. We disentangled contaminants with unique spectra such as M-stars, C-stars, planetary nebulae, quasi-stellar objects and background galaxies. Subsequently, we performed a detailed spectroscopic analysis of the remaining candidates to estimate their stellar parameters such as effective temperature, surface gravity ($\log g$), metallicity ($[\text{Fe}/\text{H}]$), reddening and their luminosities. This resulted in a sample of 35 likely post-AGB candidates with late-G to late-A spectral types, low $\log g$, and $[\text{Fe}/\text{H}] < -0.5$. Furthermore, our study confirmed the existence of the dusty post-Red Giant Branch (post-RGB) stars, discovered previously in our SMC survey, by revealing 119 such objects in the LMC. These objects have mid-IR excesses and stellar parameters (T_{eff} , $\log g$, $[\text{Fe}/\text{H}]$) similar to those of post-AGB stars except that their luminosities ($< 2500 L_{\odot}$), and hence masses and radii, are lower. These post-RGB stars are likely to be products of binary interaction on the RGB. The post-AGB and post-RGB objects show SED properties similar to the Galactic post-AGB stars, where some have a surrounding circumstellar shell, while some others have a surrounding stable disc similar to the Galactic post-AGB binaries. This study also resulted in a new sample of 162 young stellar objects, identified based on a robust $\log g$ criterion. Other interesting outcomes include objects with an UV continuum and an emission line spectrum; luminous supergiants; hot main-sequence stars; and 15 B[e] star candidates, 12 of which are newly discovered in this study.

Key words: stars: AGB and post-AGB — stars: fundamental parameters — Magellanic Clouds — Methods: observational — Techniques: photometric — Techniques: spectroscopic — planetary nebulae: general

1 INTRODUCTION

Post asymptotic giant branch (post-AGB) stars are low- to intermediate-mass stars that have evolved off the asymptotic giant branch (AGB) because a strong dusty mass loss has removed almost the whole stellar envelope. For single stars, this mass loss occurs during a phase of very high mass-loss rates called the superwind phase (e.g., Vassiliadis & Wood 1993). During the post-AGB phase, which lasts for around $\sim 10^2 - 10^5$ years (depending on the core mass), the radius of the star decreases and the star evolves to higher temperatures (from 3×10^3 K to $> 2 \times 10^4$ K) with a constant luminosity (e.g., Vassiliadis & Wood 1993, 1994). When the hot central star ionizes the surrounding mass-loss shell, the

object is referred to as a planetary nebula (PN, Balick & Frank 2002). During the post-AGB phase, the warm stellar photosphere makes it possible to quantify the chemical abundances in post-AGB stars for a very wide range of elements from CNO up to the most heavy *s*-process elements, well beyond the Ba peak (Reyniers & Van Winckel 2003), that are brought to the stellar surface during the AGB phase (Karakas & Lattanzio 2007, 2014).

For low- to intermediate-mass AGB stars in binary systems, mass loss can be induced via binary interaction (e.g., Waters et al. 1997; Chen et al. 2011; Nie et al. 2012; Abate et al. 2013; Soker 2014). A significant fraction of the ejected matter may end up in a circumbinary disc of dust and gas, and inside the disc is a binary system containing the post-AGB star (e.g., de Ruyter et al. 2006). Binary interaction alters the intrinsic properties (such as: chemical composition,

* E-mail: Devika.Kamath@ster.kuleuven.be (DK)

pulsation, mass-loss, dust-formation, circumstellar envelope morphology etc.) of the star and plays a dominant role in determining its ultimate fate. A variety of peculiar objects such as barium stars and bipolar planetary nebulae result from such binary interactions. Therefore, an in-depth study using post-AGB stars is essential to constrain both single and binary stellar evolution and to study the evolutionary connection to possible precursors and progeny.

Owing to their dusty circumstellar environments, a large mid-infrared (mid-IR) excess is a characteristic feature of post-AGB stars and a detection of cold circumstellar material using mid-IR photometry can be used to identify these objects. The first extensive search for these objects was initiated in the mid-80's using results from the Infrared Astronomical Satellite (Neugebauer et al. 1984) which enabled the identification of post-AGB stars in our Galaxy (Kwok 1993). The Toruń catalogue (Szczerba et al. 2007) for Galactic post-AGB stars lists around 391 very likely post-AGB objects. The Galactic sample of post-AGB stars have been found to be a very diverse group of objects (Van Winckel 2003). Studies showed that the majority of the optically visible Galactic post-AGB stars could be classified based on their spectral energy distributions (SEDs) into two groups: shell-sources and disc-sources (Van Winckel 2003). The shell-sources show a double-peaked SED with the hot central star peaking at shorter wavelengths while the cold, detached, expanding dust shell peaks at longer wavelengths. This type of SED is considered to be characteristic of objects that follow the single star evolution scenario mentioned above. The disc-sources do not show two distinct flux peaks in the mid-IR but they do display a clear near-infrared (near-IR) excess indicating that circumstellar dust must be close to the central star, near sublimation temperature. It is now well established that this feature in the SED indicates the presence of a stable compact circumbinary disc, and therefore these sources are referred to as disc-sources (de Ruyter et al. 2006; Deroo et al. 2007; Gielen et al. 2011b; Hillen et al. 2013). The rotation of the disc was resolved with the ALMA array (Bujarrabal et al. 2013b) in one object and using single dish observations Bujarrabal et al. (2013a) confirmed that disc rotation is indeed widespread. Moreover, these disc-sources are confirmed to be binaries and show orbital periods between 100 and 2000 days (Van Winckel et al. 2009; Gorlova et al. 2014). In contrast, for the Galactic shell-sources long-term radial velocity monitoring efforts have not yet resulted in any clear detected binary orbit (Hrivnak et al. 2011), which either confirms the single-star nature of these objects or introduces a possibility that these systems can have companions on very wide orbits.

The Galactic post-AGB stars show a large diversity in their chemical composition. Some objects are the most *s*-process enriched objects known to date (Reyniers et al. 2004) while others are not enriched at all. These *s*-process rich objects are considered to be progeny of carbon stars that have had *s*-process enrichment while on the AGB. Studies also show that many of the binary Galactic post-AGB stars are depleted in refractory elements (e.g., Giridhar et al. 2005; Maas et al. 2005; Rao et al. 2012).

Though the Galactic post-AGB sample is observationally well studied, the poorly constrained distances pose a severe limitation on our ability to fully exploit this assorted group of objects. For instance, unknown distances

(and hence luminosities and initial masses) hampers the interpretation of the diversity in the chemical abundances of these objects as a function of luminosity and mass. Also, for the binary post-AGB stars, it is not possible to associate the binary orbital parameters to the luminosity or mass.

To overcome this limitation and to better understand the post-AGB evolution, we need to exploit populations of post-AGB stars with known distances like those in the Magellanic Clouds [MCs]. Until recently, in the Small Magellanic Cloud (SMC), only 5 post-AGB candidates had been identified (Whitelock et al. 1989; Kučinskas et al. 2000; Kraemer et al. 2006; Volk et al. 2011; De Smedt et al. 2012). Similarly, in the Large Magellanic Cloud (LMC), Wood & Cohen (2001) had identified around 25 post-AGB stars based on a near-IR photometric and optical spectroscopic study of point sources from the Midcourse Space Experiment (MSX) IR survey (Egan et al. 2001). Subsequently, based on mid-IR and optical photometry, van Aarle et al. (2011) constructed a catalogue of 1337 optically visible post-AGB candidates in the LMC. They carried out a classification based on visual analysis of optical spectra of 105 of these candidates which resulted in 70 post-AGB candidates in the LMC. Recently, Matsuura et al. (2014) confirmed the evolutionary nature of seven post-AGB stars that were previously identified by Wood & Cohen (2001) and van Aarle et al. (2011). Based on polycyclic aromatic hydrocarbon (PAH) features that were found in Spitzer Space Telescope (SST) IRS spectra of these objects, they characterised the circumstellar dust which resulted in five objects being classified as C-rich post-AGB stars and two being classified as O-rich post-AGB stars.

To fully understand the post-AGB star population in the Magellanic Clouds and to provide constraints for stellar evolutionary and nucleosynthesis models, a more complete sample of these objects is definitely required. Therefore, in our recent studies, we exploited the release of the mid-IR SST surveys SAGE for the LMC (Meixner et al. 2006; Blum et al. 2006) and S³MC (Bolatto et al. 2007) and SAGE-SMC (Gordon et al. 2011) for the SMC to identify post-AGB stars in the MCs with mid-IR excesses indicative of a past history of heavy dusty mass loss. We also performed an extensive low-resolution optical spectroscopic survey to systematically characterise the optically bright post-AGB stars in the SMC and LMC.

The results of our SMC study are presented in Kamath et al. (2014) (hereafter referred to as Paper I). That study provided the first extensive spectroscopically verified catalogue of optically visible post-AGB candidates in the SMC. We were able to find a sample of 21 likely post-AGB candidates. These objects showed SED properties similar to the Galactic post-AGB stars mentioned above. The SMC study also resulted in the discovery of a sample of 42 new, low-luminosity, dusty objects that are likely to be post-RGB candidates. These objects have mid-IR excesses, stellar parameters and SEDs similar to post-AGB stars (late-G to late-A spectral types, low $\log g$ values, and low metallicities with $[\text{Fe}/\text{H}] \lesssim -1.0$). However, their luminosities ($\approx 100 - 2500 L_{\odot}$), and hence masses and radii, are much lower than that expected for post-AGB stars. Since RGB stars are known to have luminosities $\gtrsim 2500 L_{\odot}$ ¹, it is

¹ Based on observational studies in the Magellanic Clouds (e.g.,

likely that these objects are evolved, dusty post-RGB stars. Such objects have, so far, not been identified in the Galaxy, because of the unknown distance and hence luminosities to the Galactic objects. Furthermore, our study also resulted in the identification of other interesting contaminating objects with similar IR colours to post-AGB stars, such as: M-stars, C-stars, red-shifted galaxies, planetary nebulae (PNe), quasi-stellar objects (QSOs), objects with strong emission lines, and luminous young stellar objects (YSOs). All objects but the YSOs have unique spectra that allow them to be easily identified. However, disentangling the YSOs from the post-AGB/post-RGB stars is not very easy as YSOs are also surrounded by large amounts of circumstellar material and have SEDs, luminosities and spectral types similar to post-AGB/post-RGB stars. Therefore, we devised a rather robust separation criterion based on the $\log g$ of the central star which resulted in a sample of 40 likely YSO candidates. Our SMC survey revealed a rich sample of post-AGB objects similar to the Galactic post-AGB stars, a new class of dusty post-RGB objects, a significant YSO population and other interesting contaminants with similar IR colours.

To complement our above mentioned SMC study and to extend the photometric classification of optically visible post-AGB stars in the LMC by van Aarle et al. (2011), we carried out an extensive low-resolution optical spectroscopic survey to identify and characterise optically visible post-AGB stars. In this paper, we present the results of our LMC survey.

The structure of this paper is as follows: In Section 2 we present an overview of the selection criteria used to obtain an initial sample of post-AGB/post-RGB candidates in the LMC. The sample of objects considered for the spectroscopic analysis, along with the specifications of the optical spectra, the data reduction procedure and a preliminary spectral classification are presented in Section 3 and Section 4. In Section 5 we present the results of the radial velocity study used to establish LMC membership of the objects. In Section 6 we present our detailed spectroscopic analysis to estimate the stellar parameters (T_{eff} , $\log g$, $[\text{Fe}/\text{H}]$) from the spectra, and the reddening ($E[B - V]$) from SED fitting. Subsequently, in Section 7 we present the final catalogues of the spectroscopically verified post-AGB, post-RGB and YSO candidates. In Sections 8 – 10 we analyse different characteristics of these objects by examining their SEDs, their optical spectra and the evolutionary phase of the individual candidates. The completeness of the survey is presented in Section 11. In Section 12, we empirically estimate the evolutionary rates of the post-AGB and post-RGB phase. Finally, we conclude with an evaluation and summary of our survey.

2 INITIAL SAMPLE SELECTION

To obtain an initial sample selection for our spectroscopic survey, we adopted the sample selected by van Aarle et al. (2011), who identified optically visible post-AGB star candidates in the LMC based on photometry. Full details of

their selection of objects can be found in van Aarle et al. (2011). In brief, the post-AGB candidates were selected from the $\sim 4 \times 10^6$ sources in the SST SAGE LMC survey (Meixner et al. 2006; Blum et al. 2006), such that they possess a mid-IR excess compared to the mid-IR flux estimated from their optical fluxes. The selection criteria required the sources to have both $24\mu\text{m}$ and $8\mu\text{m}$ magnitudes which satisfy $F_{24\mu\text{m}} > 0.4 \times F_{8\mu\text{m}}$, (where, $F_{24\mu\text{m}}$ and $F_{8\mu\text{m}}$ are the fluxes at $24\mu\text{m}$ and $8\mu\text{m}$, respectively) or $[8] - [24] > 1.384$, (where $[24]$ and $[8]$ are the $24\mu\text{m}$ and $8\mu\text{m}$ magnitudes, respectively). Furthermore, the objects were also required to have a catalogued U, B, V, R , or I magnitude from either the Massey U, B, V, R CCD survey of the Magellanic Clouds (Massey 2002), the LMC stellar catalogue (Zaritsky et al. 2004), or the Guide Star Catalogue Version 2.3.2 (Lasker et al. 2008). The resulting sample consisted of 8628 objects. This initial sample selection was further refined by imposing a luminosity criterion based on luminosities calculated from blackbody fits (L_{bb}) to the raw photometry. The first luminosity cut (1000 to 35000 L_{bb}/L_{\odot}) was based on the expected luminosity range of post-AGB stars from evolutionary tracks of Blöcker (1995) and was aimed at removing contaminating objects such as massive young stellar objects (YSOs) and the supergiants. This luminosity cut resulted in a sample of 1517 objects. We gave these objects a priority 1 when assigning objects for spectroscopic observations. To relax the selection criteria, we included objects from van Aarle et al. (2011) with $L_{\text{bb}}/L_{\odot} < 1000$. This luminosity cut resulted in a further sample of 6823 objects. We gave these objects a priority 2 when assigning objects for spectroscopic observations. Finally, the luminosity cut of $L_{\text{bb}}/L_{\odot} > 35000$ was removed to allow the inclusion of supergiants. This luminosity cut removal resulted in a further sample of 286 stars. We gave these objects a priority 3 when assigning objects for observations.

Our total initial sample consisted of 8626 objects within which we expect to find post-AGB and post-RGB candidates. Note that in the SMC survey (see Paper I), the spectroscopically verified likely dusty post-RGB stars were discovered from an initial sample selection that was related to the sample selection of van Aarle et al. (2011). Therefore, we expect to find similar dusty, evolved, low-luminosity post-RGB systems in the LMC as well. The positions of the initial sample of objects are marked on the $[8] - [24]$ versus $[3.6] - [4.5]$ colour–colour plot shown in Figure 1. The photometric magnitudes along with the blackbody luminosities (L_{bb}/L_{\odot}) calculated from blackbody fits of all the 8626 objects in the initial sample can be found in van Aarle et al. (2011).

3 SPECTROSCOPIC OBSERVATIONS

We obtained low-resolution spectra of stars selected from the initial sample of objects. The spectra were taken using the AAOmega double-beam multi-fibre spectrograph (Sharp et al. 2006) mounted on the 3.9m Anglo Australian Telescope (AAT) at Siding Spring Observatory (SSO). AAOmega allows for the simultaneous observation of 392 targets (including science objects, sky-positions, and fiducial guide stars) over a 2 degree field using the 2dF fibre positioner (Lewis et al. 2002). The projected diameter of

Frogel et al. 1983; Wood et al. 1999; Cioni et al. 1999) and evolutionary tracks of Bertelli et al. (2008) corresponding to LMC and SMC metallicities

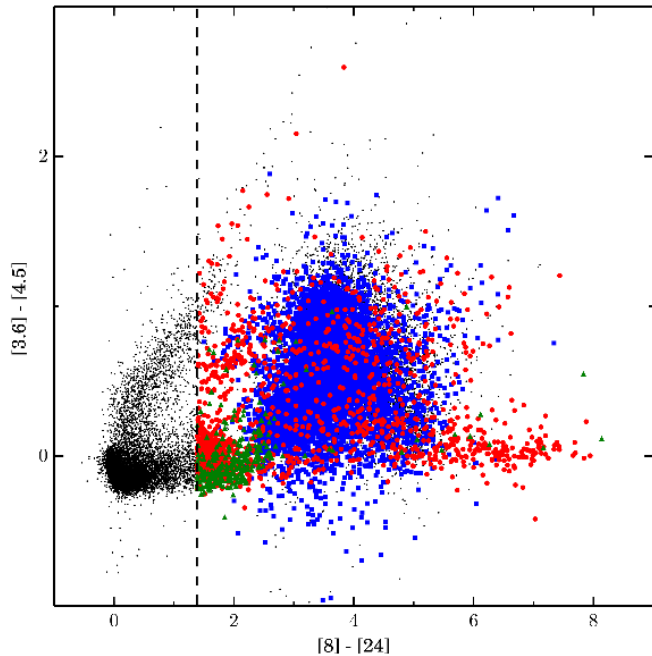


Figure 1. The colour–colour plot of $[8] - [24]$ versus $[3.6] - [4.5]$. The small black dots in the background represent the entire field LMC population with a valid $24\mu\text{m}$ magnitude from the SAGE catalogue. The red filled circles represent the priority 1 candidates. The blue filled squares represent the priority 2 objects and the green filled triangles represent the priority 3 objects. We note that some of the priority 1, priority 2 and priority 3 objects do not show detections at $[3.6]$ or $[4.5]$ microns, and therefore do not appear in this plot. The region to the right of the black dashed line defines the selection criterion in the $[8] - [24]$ plane. The black dots in this region fail one or more of our selection criteria. See text for further details.

each fibre is 2 arcsec. Within each configuration there is a minimum target separation of ~ 30 arcsec imposed by the physical size of the fibres and positioner (Miszalski et al. 2006). The field centers of the LMC observations in our survey are given in Table 1 and they are shown in Figure 2. A Ne-Ar arc and a quartz lamp flat field exposure were taken per field for calibration. We used the 580V grating with a central wavelength of 4800\AA and the 385R grating with a central wavelength of 7250\AA . This combination provides a maximum spectral coverage of $3700\text{--}8800\text{\AA}$ at a resolution of 1300. The AAOmega raw data were reduced using a combination of the AAOmega-2dFDR reduction pipeline² supplied and maintained by the Anglo-Australian Observatory and IRAF³ routines. The spectral observations and the data reduction method used in this study is the same as that of the SMC survey (Paper I) and full details can be found therein.

We obtained a total of 2262 spectra. Not all of the 8626 candidates could be observed due to limited observational

Table 1. The field centers of the LMC observations in our survey and the corresponding exposure times.

Field	RA (2000)	Dec (2000)	Exposure
LMC1	05 16 48.00	-69 42 00.0	$4 \times 900\text{s}$
LMC2	05 36 00.00	-70 54 00.0	$3 \times 900\text{s}$
LMC3	05 04 48.00	-68 18 00.0	$3 \times 900\text{s}$
LMC4	04 48 00.00	-69 30 00.0	$3 \times 900\text{s}$
LMC5	04 58 12.00	-66 36 00.0	$4 \times 900\text{s}$
LMC6	05 45 00.00	-69 24 00.0	$4 \times 900\text{s}$
LMC7	05 28 48.00	-68 06 00.0	$4 \times 900\text{s}$
LMC8	05 22 12.00	-72 06 00.0	$4 \times 900\text{s}$
LMC9	05 01 48.00	-71 00 00.0	$4 \times 900\text{s}$

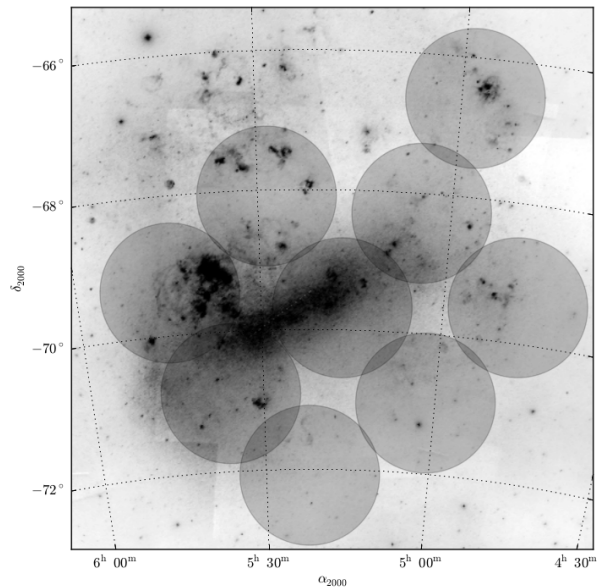


Figure 2. A Digitalised Sky Survey (DSS) image of a 8 degree field of view centered on the LMC. The circles represent the observed 2 degree fields in the LMC, with field centers listed in Table 1, that were covered in our survey.

time. Moreover, some of the stars from the initial sample selection were out of the fields that were observed while some objects were spatially too close for fibre assignments to be done simultaneously. Furthermore, as shown in Figure 2, some of the target sources were observed more than once due to overlap in the observed fields. For such sources, we either averaged the multiple observations or rejected the observation with low signal. In the end we were left with spectra of 2102 unique candidates from the initial sample of 8626 objects. Out of these 2102 objects, 885 were priority 1 objects, 1173 were priority 2 objects and 49 were priority 3 objects. Figure 3 shows the positions of these 2102 objects, marked on the $[8] - [24]$ versus $[3.6] - [4.5]$ colour–colour plot used for our initial sample selection (see Section 2).

In Table 2, we provide photometric magnitudes for the first five candidates from the group of 2102 unique candidates for which spectra were obtained. The full table which contains the photometry of the 2102 candidates is available as online supporting information. As mentioned in Section 2, the selection criteria for the candidates that we adopted from van Aarle et al. (2011) in our survey involve optical, near-IR and mid-IR photometry. Photometry in the U, V, B, R and

² http://www.aao.gov.au/AAO/2df/aaomega/aaomega_software.html

³ IRAF is distributed by the National Optical Astronomy Observatory, which is operated by the Association of Universities for Research in Astronomy (AURA) under cooperative agreement with the National Science Foundation

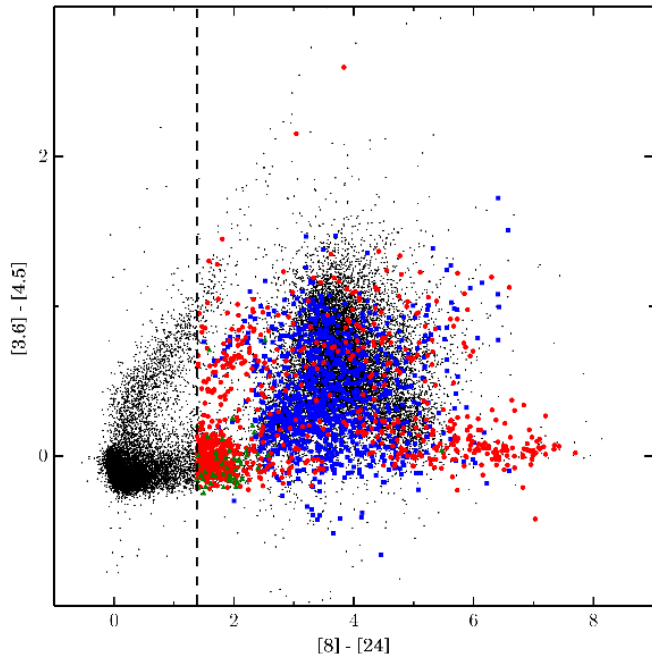


Figure 3. The same as Figure 1 but for only those 2102 objects from the initial selection sample for which we obtained an optical spectrum. The small black dots in the background represent the entire field LMC population with a valid $24\mu\text{m}$ magnitude from the SAGE catalogue. The red filled circles represent the priority 1 candidates with an optical spectrum. The blue filled squares represent the priority 2 objects with an optical spectrum and the green filled triangles represent the priority 3 objects with an optical spectrum. We note that some of the priority 1, priority 2 and priority 3 objects do not show detections at $[3.6]$ or $[4.5]$ microns, and therefore do not appear in this plot.

I bands were added from either Massey U, B, V, R CCD survey of the Magellanic Clouds (Massey 2002), the LMC stellar catalogue (Zaritsky et al. 2004), or the Guide Star Catalogue Version 2.3.2 (Lasker et al. 2008). The SAGE-LMC survey covers the IRAC ($3.6, 4.5, 5.8,$ and $8\mu\text{m}$) and the MIPS ($24.0, 70.0,$ and $160.0\mu\text{m}$) bands. The Spitzer sources have been merged with the Two Micron All Sky Survey (2MASS) $J, H,$ and K bands ($1.24, 1.66$ and $2.16\mu\text{m}$, Skrutskie et al. 2006). We also added WISE photometry in the $3.4, 4.6, 12,$ and $22\mu\text{m}$ bands $W1, W2, W3,$ and $W4,$ respectively (Wright et al. 2010). Column (22) of Table 2 also gives the observed luminosity (L_{ob}) of the candidates. L_{ob} for these sources was obtained by integrating under the SED defined by all the photometric bands after correcting for the effects of Galactic and LMC reddening (similar to the method that was used for the SMC sources, see Paper I). We used a mean reddening $E(B-V) = 0.08$ mag for the combined LMC and Galactic components (Keller & Wood 2006).

We found that for 556 of the 2102 objects, their spectra had too low signal (mostly less than 200 counts) such that no relevant spectral features could be detected. These objects were discarded. Hence, at this stage, we were left with good spectra of 1546 individual objects.

Table 2. Photometric data. See text for full details. The full table is available online.

Object Name	RA(°)	DEC(°)	U	B	V	R	I	J	H	K	$W1$	[3.6]	[4.5]	$W2$	[5.8]	[8.0]	$W3$	$W4$	[24]	[70]	[160]
L_{obs}/L_{\odot}	$T_{\text{eff,SED}}(\text{K})$																				
J043617.75-693022.0	69.073958	-69.506111	99.999	99.999	99.999	18.34	99.999	16.789	16.112	15.377	15.016	14.876	14.289	14.641	14.563	12.667	11.282	9.687	9.38	99.999	99.999
121	3500																				
J043652.36-693356.2	69.218167	-69.565611	99.999	99.999	99.999	17.75	99.999	16.98	16.445	15.927	99.999	15.326	15.133	99.999	14.794	12.433	99.999	99.999	9.24	99.999	99.999
118	4250																				
J043655.62-694748.1	69.23175	-69.796694	99.999	99.999	99.999	18.01	99.999	16.865	16.071	15.662	15.421	15.14	15.106	15.328	14.219	11.802	11.253	9.348	9.448	99.999	99.999
128	3750																				
J043702.61-694130.6	69.260875	-69.691833	19.738	19.025	17.327	15.54	14.313	12.573	11.668	11.376	11.353	11.237	11.324	11.335	11.107	10.786	10.185	9.253	9.307	99.999	99.999
4011	3500																				
J043706.79-694922.6	69.278292	-69.822944	18.814	18.727	17.696	15.48	99.999	15.254	14.537	14.191	13.611	14.076	14.237	13.584	13.511	12.099	11.156	8.998	9.342	99.999	99.999
743	4750																				

Note: The object name is the SAGE name. The RA and DEC coordinates are given for the J2000 epoch. Null magnitudes are listed as 99.999. L_{obs}/L_{\odot} is the observed luminosity. $T_{\text{eff,SED}}(\text{K})$ is the photometric temperature obtained by fitting ATLAS9 atmosphere models (Castelli & Kurucz 2003) to the B , V , I , and J bands corrected for foreground extinction.

4 PRELIMINARY SPECTRAL CLASSIFICATION

Though a mid-IR excess is characteristic of post-AGB and post-RGB stars, there are other interesting objects with mid-IR excesses such as M stars, C stars, PNe, background galaxies, and QSOs etc. These intermingled contaminants have characteristic spectra which can be used to identify them. Therefore, we performed a preliminary spectral analysis, by eye, to categorise the group of 1546 objects with good optical spectra into bins based on the nature of their spectra.

We found a group of 290 background galaxies and 39 QSOs that were identified by their large redshifts and the width of the emission lines of hydrogen and metallic lines (e.g. Field 1973; Vanden Berk et al. 2001). Some of the background galaxies and QSOs identified in this study have been published in Cioni et al. (2013). The full sample of background galaxies and QSOs will be discussed in a following publication. A group of 382 cool M-stars were identified based on the presence of strong molecular absorption features of titanium oxide (TiO) and vanadium oxide (VO) (e.g. Kirkpatrick et al. 1999). We also identified 55 cool C-stars characterised by the presence of key molecules such as C₂, CN, and CH (see Wallerstein & Knapp 1998, for a review on C stars). Based on the presence of an emission-line spectrum characterised by recombination lines of hydrogen and helium as well as various collisionally-excited forbidden lines of heavier elements such as O, N, C, Ne, and Ar, we were able to identify 123 PNe (see Frew & Parker 2010, for further details on identifying PNe). From the 123 PNe, 32 objects are likely newly identified PNe, as they have not been previously classified in the literature. The sample of M-stars, C-stars and PNe is presented in Appendix A. Five stars in our sample were identified to be stars with TiO bands in emission. These objects are discussed in Wood et al. (2013) and are not considered further here. We also found a group of 69 objects with prominent emission lines throughout their spectrum. The majority of these objects also show a broad H α emission line profile mostly along with a UV continuum. Hot post-AGB/post-RGB stars are likely to have an emission-line spectrum characterised by a broad H α profile along with weak recombination lines of hydrogen and helium and various collisionally-excited forbidden lines of heavier elements (e.g., Van Winckel 2003). The spectra of YSO candidates are also likely to show a broad H α emission line profile owing to the disc accretion (Natta et al. 2002; Jayawardhana et al. 2002). For 15 of these 69 objects (J044739.07-692036.5, J044745.05-694048.3, J045647.06-695024.7, J050224.17-660637.4, J050504.33-674744.9, J050951.27-684845.2, J051247.94-690307.1, J051338.88-692108.1, J051451.00-692544.1, J052605.27-683609.4, J052613.39-684715.0, J052630.65-674036.6, J052707.10-702001.9, J052747.62-714852.8, J053218.75-681731.5) we were able to clearly detect FeII emission line features. Their spectra not only show a UV continuum and strong Balmer emission lines, but also the low-excitation permitted emission lines of singly ionised metals (e.g., the multiplet 42 of FeII at $\approx 4924\text{\AA}$, 5018\AA , and 5169\AA), forbidden emission lines of [FeII] and [OI] and higher ionisation emission lines (e.g., [OIII] and [HeII]). These spectral features in

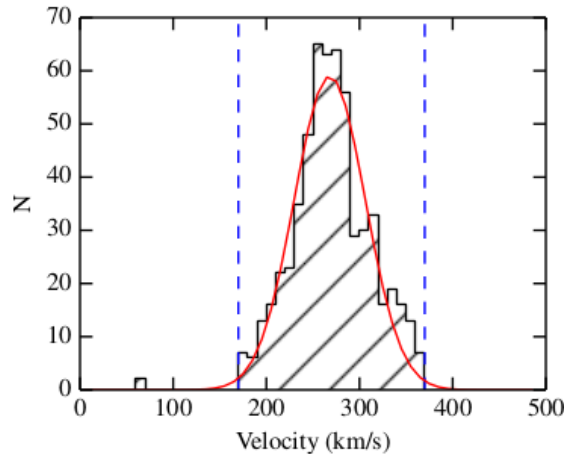


Figure 5. Radial velocity histogram for the group of 583 probable post-AGB/post-RGB and YSO candidates. The red curve denotes a Gaussian with a mean of 270 km s^{-1} and a standard deviation of 40 km s^{-1} . The blue dashed lines denote the radial velocity interval (defined as a 2.5 sigma deviation from the mean of the Gaussian fit) used in our study to select stars with a radial velocity belonging to the LMC.

combination with a strong infrared excess in the spectra of early-type stars is characteristic of the B[e] phenomenon (Zickgraf 2000; Miroshnichenko 2007). Out of the 15 objects, three (J045647.06-695024.7, J051338.88-692108.1 and J052747.62-714852.8) have been previously classified as B[e] stars by Zickgraf (2006). Therefore, it is likely that the remaining objects are newly identified B[e] stars in the LMC. Thus, based on their spectral features, we expect the group of 69 objects with an emission line spectrum to contain hot post-AGB/post-RGB stars, hot YSOs and B[e] candidates. We do not carry out any further spectral analysis on the 69 objects, owing to their spectra being dominated by emission lines. A detailed analysis of these objects will be presented in following a publication.

After the removal of the above mentioned contaminants, the remaining 583 objects were carried forward for a detailed spectral analysis, similar to the one carried out in Paper I. The spectra and IR colours of YSOs are very similar to those of post-AGB/post-RGB stars. Therefore, amongst the remaining sample of 583 objects, we expect to find not just post-AGB/post-RGB candidates but also YSOs, similar to what we found in our SMC study (see Paper I).

Figure 4 shows all the 1546 sources with good spectra plotted on the colour–colour plot of $[8] - [24]$ vs $[3.6] - [4.5]$ used for our sample selection (see Section 2). The different symbols in Figure 4 represent the nature of the sources as classified by the preliminary spectral analysis described above.

5 ESTABLISHING LMC MEMBERSHIP OF THE PROBABLE POST-AGB/POST-RGB AND YSO CANDIDATES

To establish LMC membership of the group of 583 post-AGB/post-RGB/YSO candidates, we derived heliocentric radial velocities using the Fourier cross-correlation tech-

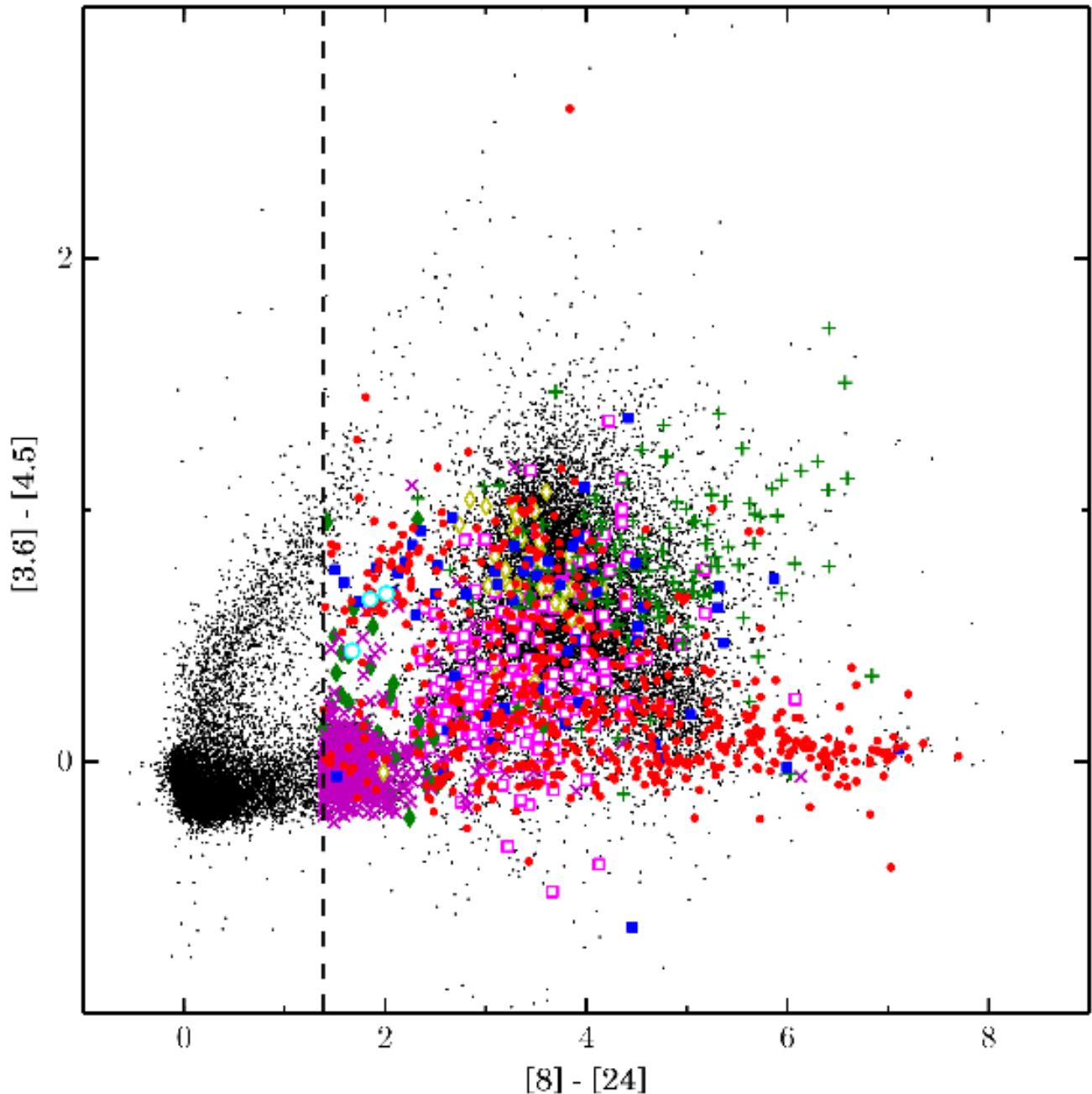


Figure 4. The 1546 sources with good spectra plotted on the colour-colour plot of $[8] - [24]$ vs $[3.6] - [4.5]$ with the general spectral classification indicated by symbol type. The small black dots in the background represent the entire field LMC population with a valid $24\mu\text{m}$ magnitude from the SAGE catalogue. The red filled-circles represent the sample of probable post-AGB/RGB and YSO candidates. The blue filled-squares represent the sample of objects that have strong emission lines. The cyan open-circles represent the objects with TiO bands in emission. The green plus symbols represent the PNe population. The green filled diamonds represent C-stars, and the magenta crosses represent M-stars. The magenta open squares represent the sample that has been classified as background galaxies. The yellow open diamonds represent the sources identified as QSOs. In each of the groups, objects that do not have detections at $[3.6]$ or $[4.5]$ microns do not appear in this plot.

nique. For cross-correlation we used only the calcium IR triplet (CaT) region from 8400\AA to 8700\AA , the Balmer line region from 3700\AA to 4000\AA , and the $H\alpha$ region from 6250\AA to 6450\AA . The procedure is similar to that used for the SMC objects (see Paper I for full details). For each ob-

ject we estimated three radial velocities resulting from the cross-correlation of the three regions of the spectra with the three templates. The adopted heliocentric velocity was chosen to be the one with the minimum radial velocity error. Radial velocity errors for each cross-correlation were com-

puted by *FXCOR* based on the fitted peak height and the antisymmetric noise as described by Tonry & Davis (1979). A typical error in the adopted radial velocity is 11 km s^{-1} . We note that, for some of the objects, instead of the CaT absorption lines, there are CaT lines in emission or the Paschen lines. For such objects only two regions (Balmer line region and H α region) were used for cross-correlation. This also applies to stars of an earlier spectral type that have Paschen lines that lie in the CaT region.

Figure 5 shows the histogram of the heliocentric velocities for the 583 targets. A Gaussian fit to the histogram results in an average velocity of 270 km s^{-1} and standard deviation of 40 km s^{-1} . The estimated average velocity agrees well with the velocity expected for stars in the LMC ($\approx 270 \text{ km s}^{-1}$, van der Marel et al. 2002; Clementini et al. 2003). Based on the expected radial velocity for stars in the LMC and also the shape of the velocity distribution of our sample of stars, we found that 581 out of the 583 candidates lie within the range of 170 to 370 km s^{-1} (these limits correspond to a 2.5 sigma deviation from the mean radial velocity of the fitted Gaussian). The 2 stars, J052020.60-693115.4, J052348.94-711201.8, that lie outside this interval have heliocentric velocities $\approx 60 \text{ km s}^{-1}$ and are likely Galactic objects in the field of view of the LMC. After removing these 2 stars, we are left with a sample of 581 candidates with confirmed LMC membership.

6 DETERMINATION OF STELLAR PARAMETERS

Deriving stellar parameters such as T_{eff} , $\log g$, [Fe/H], and $E(B - V)$ is crucial to fully characterise the remaining candidates. In the following sub-sections we present our systematic procedure to establish a spectroscopically verified catalogue of post-AGB and post-RGB stars in the LMC.

6.1 Spectroscopic analysis

We performed a detailed spectroscopic analysis of the 581 candidates using a fully automated spectral typing pipeline (STP) to simultaneously determine the stellar parameters (T_{eff} , $\log g$, and [Fe/H]) of the candidates. A detailed description of our STP is mentioned in Paper I. In brief, our STP matches each individual observed spectrum to a library of synthetic templates, and finds the minimum root mean square (RMS) deviation over a carefully restricted T_{eff} , $\log g$, and [Fe/H] grid. The synthetic templates were obtained from the Munari synthetic library (Munari et al. 2005) which consists of a grid of nearly 60000 spectra, based on the local thermodynamical equilibrium (LTE) Kurucz-Castelli atmosphere models (Castelli & Kurucz 2003). In the STP, our RMS calculations follow a weighting scheme which is based on certain spectral regions that are sensitive to specific stellar parameters. For instance, the calcium IR triplet [CaT] region from 8400 \AA to 8700 \AA , serves as a good metallicity indicator. This helps to break the degeneracy that often plagues automated spectral classification algorithms. Since our spectral resolution is low, the only good metallicity indicator is the CaT region. Therefore, for those stars whose spectra do not contain CaT absorption lines, [Fe/H] is fixed to -0.5 which is the mean metallicity of the LMC (see Van

der Swaelmen et al. 2013, and references therein). Note that for some stars with a low signal, the resulting fit from the STP was poor. In these cases, during their spectral analysis we fixed the [Fe/H] to provide some constraints to the STP.

We note that the STP does not consider the H α region, from $6500\text{-}6650 \text{ \AA}$, while estimating the minimum RMS deviation owing to the diversity of the observed H α line profiles that range from emission to complex line profiles (with both emission and absorption components).

Figure 6 shows an example of the fitting result of the STP for a candidate in our sample. The plot presents the inverse RMS distribution (goodness of fit) in the $T_{\text{eff}} - \log g$ space and the $T_{\text{eff}} - [\text{Fe}/\text{H}]$ space, with the interpolated final values marked. The preferentially weighted spectral regions used during the spectral typing process are plotted and important spectral features are also indicated. Depending on the strength of the spectral features, lines such as the BaII line at 4554.03 \AA , the BaII line at 6496.89 \AA , and the BaI line at 6498.76 \AA can be detected. These are indicators of possible *s*-process enrichment and are marked on each plot for the identification of the sources in which we can identify *s*-process enrichment. Similarly, LiI lines at 6707.77 \AA and 6707.92 \AA are also marked for identification of Li in the candidates (although the two lines are unresolved at the resolution of our spectra and their position is indicated by a single blue dashed vertical line in Figure 6.)

For each of the 581 candidates that were fed into the STP, we were able to derive T_{eff} , $\log g$, and [Fe/H] values. Plots similar to Figure 6 for all these candidates are available as online supporting information.

In Paper I, we present a detailed error estimation of our STP by using three objects that were then in our study and which were also previously examined using high-resolution spectra. Currently, we have a sample of seven objects (including the three objects used in Paper I). Out of these seven objects four (J050632.10-714229.8, J051848.84-700247.0, J053250.69-713925.8 and J053253.51-695915.1) are LMC objects whose chemical abundances have been studied in detail using UVES spectra (van Aarle et al. 2013), and three (J004441.04-732136.4, J010056.95-715551.4 and J010333.89-724405.7) are SMC objects (De Smedt et al. 2012, De Smedt et al. in prep). Table 3 gives the estimated T_{eff} , $\log g$, and [Fe/H] values using our STP and the corresponding values estimated using high-resolution spectra obtained from the literature mentioned above. By comparing the two sets of values, we get a mean RMS difference for each of the stellar parameters as follows: $\Delta T_{\text{eff}} = 250 \text{ K}$, $\Delta \log g = 0.7$, and $\Delta [\text{Fe}/\text{H}] = 0.2 \text{ dex}$.

Additionally, the low-resolution optical AAOmega spectra have a range of signal from 100 to 3000 counts. In Paper I, we tested the reliability of our STP as a function of signal by taking a set of synthetic spectra varying in temperatures from 3500K to 9500K (the T_{eff} region over which we expect most of the post-AGB/RGB and YSO candidates to lie), in $\log g$ from 0.5 to 1.5, with fixed [Fe/H] = -1.0 . To these synthetic spectra we added AAOmega detector read noise and varying levels of photon noise, resulting in artificial spectra with quality equivalent to measured spectra of 100, 500, 1500, and 3000 counts. The artificial spectra were then passed through the spectral typing pipeline. These tests resulted in mean errors of 250K in T_{eff} , 0.5 in $\log g$, and 0.5 in [Fe/H], for stars with T_{eff} values $\leq 10000 \text{ K}$. From this er-

Table 3. Determination of error estimates in the derived T_{eff} , $\log g$, and $[\text{Fe}/\text{H}]$ from the STP based on a sample of objects previously studied with high-resolution spectra (see text for full details).

Object	$T_{\text{eff,STP}}$ (K)	$\log g_{\text{STP}}$	$[\text{Fe}/\text{H}]_{\text{STP}}$ (dex)	$T_{\text{eff,high-res}}$ (K)	$\log g_{\text{high-res}}$	$[\text{Fe}/\text{H}]_{\text{high-res}}$ (dex)	ΔT_{eff} (K)	$\Delta \log g$	$\Delta [\text{Fe}/\text{H}]$ (dex)
J004441.04-732136.4	6168	1.0	-1.0	6250	0.5	-1.0	82	0.5	0.0
J010056.95-715551.4	4295	0.0	-0.9	4250	1.0	-1.0	45	1.0	0.1
J010333.89-724405.7	4621	0.0	-0.9	4500	1.0	-0.6	121	1.0	0.3
J050632.10-714229.8	7614	0.5	-0.4	6750	0.5	-1.0	864	0.0	0.6
J051848.84-700247.0	6015	0.0	-1.0	6000	0.5	-1.0	15	0.5	0.0
J053250.69-713925.8	6073	1.0	-1.1	5500	0.0	-1.0	573	1.0	0.1
J053253.51-695915.1	4698	1.5	-0.7	4750	2.5	-0.7	52	1.0	0.0

ror estimation exercise and comparison with high-resolution studies, we conclude that the expected errors in our derived parameters are in the range: 250K to 500K in T_{eff} , 0.5 to 1.0 in $\log g$, and 0.5 to 1.0 in $[\text{Fe}/\text{H}]$. We note that for higher temperatures ($T_{\text{eff}} > 10000\text{K}$) the grid spacings of the synthetic templates in T_{eff} increase from the 250K step (which applies to $T_{\text{eff}} < 10000\text{K}$) to steps of 500K, 1000K, 1500K and 2500K as T_{eff} increases (see Munari et al. 2005), and therefore accurate error estimations are not feasible.

6.2 Reddening estimates

Owing to the large mid-IR excesses displayed by our candidates, the expected reddening in these objects is significant. The total reddening, which includes both the interstellar and circumstellar reddening, can be determined by estimating the difference between the intrinsic colour of the candidate (derived from the T_{eff} estimated from the spectrum) and the measured colour (derived from the raw photometry based on the B , V , I and J magnitudes). Of the sample of 581 candidates, we found that 85 objects did not have both B and I magnitudes and thus there were not enough data points to estimate the value of $E(B - V)$. We therefore removed this sample of 85 objects from further analysis. These objects are presented in Appendix B.

The remaining sample consisted of 496 candidates for which we calculated the $E(B - V)$ by estimating the value of $E(B - V)$ that minimised the sum of the squared differences between the de-reddened observed and the intrinsic B , V , I and J magnitudes. At longer wavelengths, emission from dust can contribute to the observed magnitudes. We used the Cardelli et al. (1989) extinction law, assuming $R_V = 3.1$. It is possible that the circumstellar extinction law is different from the interstellar extinction law but we have not explored this possibility. The derived $E(B - V)$ values were used to correct the observed magnitudes for extinction. Then the $BVIJ$ fluxes of the best-fit model atmosphere (derived from the STP) were normalised to the corrected $BVIJ$ fluxes. For a few stars the estimated $E(B - V)$ was negative which indicates that the T_{eff} estimated from the spectra is likely to be cooler than the actual T_{eff} of the star. For such stars, we re-estimated the $E(B - V)$ by adopting T_{eff} values that were increased by 250K or by 500K than the estimated T_{eff} values of the stars. Therefore, the derived total reddening serves as a good check for the T_{eff} value estimated using the STP (see Subsection 6.1).

The uncertainty in the $E(B - V)$ estimate owing to other errors, such as errors in the photometry and errors in the derived T_{eff} values, are small. We estimated the maximum

error in $E(B - V)$ to be the difference between $E(B - V)$ at the estimated T_{eff} , and at T_{eff} values of ± 250 . We find that the error $\Delta E(B - V) \approx 0.2$ mag at $T_{\text{eff}} \sim 4000\text{K}$ and declines with increasing T_{eff} to $\Delta E(B - V) \approx 0.1$ mag at $T_{\text{eff}} \sim 5000\text{K}$ and $\Delta E(B - V) \approx 0.05$ mag at $T_{\text{eff}} \sim 6500\text{K}$.

6.3 The luminosity of the central star

For post-AGB/post-RGB and YSO candidates, the central star is surrounded by circumstellar dust that is not necessarily spherically symmetric. For such cases, the observed luminosity L_{ob} (obtained by integrating the flux under the observed SED) could either be over-estimated or under-estimated. For this reason it is essential to estimate the photospheric luminosity of the central star L_{ph} .

This photospheric luminosity (L_{ph}) can be derived from the bolometric correction for the model atmosphere corresponding to each individual candidate normalised to the de-extincted V magnitude, coupled with the distance modulus to the LMC. We note that for some objects, we find that the available luminosity L_{ph} from the central star is too small to account for the luminosity L_{ob} derived by integrating the total SED thus resulting in L_{ob} being $\sim 1.5 - 5$ times L_{ph} . This trend was also found for some of the objects in our previous studies (see Wood et al. 2013; Kamath et al. 2014). This is likely due to the non-spherically symmetric dust envelope. Alternatively, it could be due to a substantial flux contribution from another object coincident on the sky with the optically observed star or uncertainties in the reddening estimates.

7 SEPARATION OF THE POST-AGB, POST-RGB AND YSO CANDIDATES

Based on the estimated stellar parameters (T_{eff} , $\log g$, and $[\text{Fe}/\text{H}]$, see Subsection 6.1), the $E(B - V)$ values (see Subsection 6.2) and the derived photospheric luminosity L_{ph} (see Subsection 6.3) of the 496 remaining candidates, we were able to systematically characterise the sample as follows.

On analysing their stellar parameters, we found that the sample is more diverse than expected. Post-AGB/post-RGB stars are expected to have luminosities $\lesssim 35000 L_{\odot}$. Therefore, based on the estimated L_{ph} value, we were able to identify a sample of 112 luminous objects with $L_{\text{ph}} \geq 35000 L_{\odot}$. These objects are likely to be supergiants or massive main-sequence stars. Furthermore, Post-AGB/post-RGB stars are expected to have spectral types A, F, G and K (Van Winckel 2003), the hotter objects having already rapidly evolved to

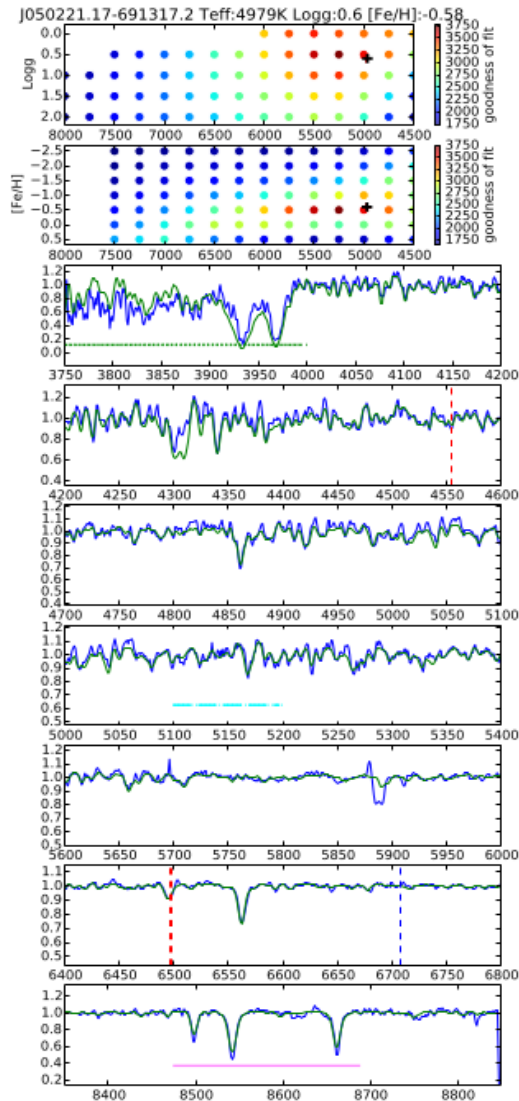


Figure 6. An example of the spectral fitting result from the STP for a candidate in our sample. The first two subplots show the inverse RMS distribution (goodness of fit) in the $T_{\text{eff}} - \log g$ space and $T_{\text{eff}} - [\text{Fe}/\text{H}]$ space with a black plus representing the final interpolated value. In the remaining subplots, the observed spectrum is shown in blue, whilst the green line represents the best-fitting synthetic spectrum. The green-dotted, cyan-dashed and pink-solid horizontal lines represent the preferentially weighted T_{eff} , $\log g$ and $[\text{Fe}/\text{H}]$ regions (see Paper I for full details). The blue dashed vertical line marks the position of the LiI lines at 6707.77\AA and 6707.92\AA . The single red dashed vertical line marks the position of the BaII line at 4554.03\AA and the double red dashed vertical lines mark the positions of the BaII line at 6496.89\AA , and the BaI line at 6498.76\AA . In this object, the Balmer lines of hydrogen are filled in with emission.

the PNe stage. Based on the derived T_{eff} values, we were able to identify a sample of 68 objects with $T_{\text{eff}} > 10000\text{K}$. Some of these objects could very well be hot post-AGB/post-RGB stars or YSO candidates. However, the spectra of majority of these 68 objects do not show an emission-line spectrum characterised by weak recombination lines of hydrogen and

helium and various collisionally-excited forbidden lines of heavier elements (e.g., Van Winckel 2003), that are characteristic of hot post-AGB/post-RGB stars. Moreover, hot YSO candidates show rather broad $\text{H}\alpha$ profiles due to accretion (Natta et al. 2002; Jayawardhana et al. 2002) while most of our 68 objects do not show such $\text{H}\alpha$ emission line profiles. Therefore, these objects are likely to be main-sequence stars.

A detailed analysis of the 112 luminous objects with $L_{\text{ph}} \geq 35000 L_{\odot}$ and the 68 likely main-sequence stars with early-A, O and B spectral types will be discussed in a following publication. After the removal of these objects, the remaining sample consists of 316 objects that are likely to be either post-AGB/post-RGB or YSO candidates.

Disentangling the post-AGB/post-RGB candidates from the YSO candidates is a concern since these unrelated objects lie in the same region of the HR diagram with similar T_{eff} and L_{ph} values and they have very similar IR colours and dust excesses. In our SMC survey (see Paper I), to distinguish between the post-AGB/post-RGB and YSO objects, we devised a criterion based on the $\log g$ of the central star. At a given luminosity, the mass of a YSO is about 15 – 20 times that of the corresponding post-AGB/post-RGB star (see Figure 14), leading to a difference of ~ 1.3 in $\log g$ between post-AGB/post-RGB stars and YSOs.

To derive the theoretical $\log g$ value a star (with a specific photospheric luminosity, L_{ph} and intrinsic temperature, T_{eff}) would have during the post-AGB phase, we first derived the mass of the post-AGB star using the photospheric luminosity (L_{ph}) and the luminosity-core mass relation (Wood & Zarro 1981) for AGB stars. During the post-RGB phase (if $L_{\text{ph}}/L_{\odot} \leq 2500$), a similar procedure can be used but using a luminosity-core mass relation derived from a fit to the evolutionary tracks of Bertelli et al. (2008) with $Z = 0.004$. For a given post-AGB/post-RGB star, the stellar mass (M/M_{\odot}) is essentially the core mass of the progenitor AGB/RGB star.

Using this estimated mass value along with the L_{ph} and T_{eff} of the object, we calculated the theoretical $\log g$, value the object would have during the post-AGB/post-RGB phase. Similarly, using the PISA pre-main sequence evolutionary tracks (Tognelli et al. 2011) for $Z = 0.004$ (and an extrapolation to higher masses since the maximum mass of the PISA tracks is $7 M_{\odot}$), we estimated the theoretical value of $\log g$ the same object would have if it were on the pre-main sequence evolutionary track. The difference of the two theoretical values resulted in a difference factor of ~ 1.3 between the post-AGB/RGB stars and the pre-main sequence stars of a given luminosity and T_{eff} (see Paper I for full details). The errors in our $\log g$ estimates for individual stars are typically in the range 0.5 – 1.0 (see Subsection 6.1). Therefore, we applied this $\log g$ criterion to the remaining sample of 316 objects and we were able to identify a sample of 162 YSO candidates and 154 post-AGB/post-RGB candidates.

We note that in determining the stellar parameters such as T_{eff} , $\log g$, and $[\text{Fe}/\text{H}]$, the $\log g$ estimates have the highest uncertainty since the $\log g$ value least affects the spectra when compared to the T_{eff} and $[\text{Fe}/\text{H}]$. Therefore, despite the criteria used to separate the post-AGB/post-RGB candidates from the YSOs, there remains a degree of uncertainty in our classification method. Detailed studies based on high-

resolution spectra are needed to confirm the nature of the individual objects.

We then made the distinction between post-AGB and post-RGB candidates using a luminosity criterion. Post-AGB stars were assumed to have $L_{\text{ph}}/L_{\odot} > 2500$ and post-RGB stars were assumed to have $L_{\text{ph}}/L_{\odot} \leq 2500$. This is based on the expected luminosity of the RGB-tip for stars in the LMC and SMC (see Section 1 and Paper I). We found a sample of 35 post-AGB candidates and 119 post-RGB candidates.

Since post-AGB/post-RGB stars are an old to intermediate age population, we expect them to be more metal poor than the YSOs. The young LMC population has a mean metallicity of $[\text{Fe}/\text{H}] \simeq -0.5$ (Van der Swaelmen et al. 2013, and references therein). Figure 7 shows the $[\text{Fe}/\text{H}]$ distribution for the post-AGB candidates, post-RGB candidates, and YSO candidates⁴. From Gaussian fits to the histograms (Figure 7) we find that the post-AGB sample peaks at a $[\text{Fe}/\text{H}] = -0.6$ with a standard deviation of 0.4, the post-RGB sample peaks at $[\text{Fe}/\text{H}] = -1.0$ with a standard deviation of 0.7 whilst the YSO sample, peaks at a higher metallicity of $[\text{Fe}/\text{H}] = -0.3$ with a standard deviation of 0.3. This indicates that, as expected, the post-AGB and post-RGB evolved objects are indeed more metal poor than the YSO population. Using the 2-sided Kolmogorov-Smirnov (KS) test, we find that the post-AGB/post-RGB candidates are more metal poor than the YSOs with high confidence. The probability of the post-AGB and YSO samples being drawn from the same distribution is $P \sim 10^{-2}$. The probability of the post-RGB and YSO samples to be drawn from the same distribution is $P \sim 10^{-7}$. Finally the probability of the post-AGB and post-RGB samples to be drawn from the same distribution is $P \sim 0.3$, i.e., there is no significant evidence for a different metallicity distribution for these two groups. However, there definitely exist distinct metallicity distributions for the evolved and young objects which strongly supports our separation of post-AGB/post-RGB from the YSO candidates.

Figure 8 shows the positions of the spectroscopically verified post-AGB, post-RGB, and YSO candidates on the colour-colour plot of $[8] - [24]$ vs $[3.6] - [4.5]$ used for our sample selection (see Section 2). Figure 8 also shows the positions of the 112 luminous objects with $L_{\text{ph}} \geq 35000 L_{\odot}$, the 68 likely main-sequence stars with early-A, O and B spectral types, and the 85 likely post-AGB, post-RGB and YSO candidates without a detection in the B and V bands (see subsection 6.2).

In Tables 4 and 5 we list the final sample of post-AGB and post-RGB candidates, along with their derived stellar parameters such as T_{eff} , $\log g$, $[\text{Fe}/\text{H}]$, $E[B - V]$, stellar mass (M/M_{\odot}), the observed luminosity (L_{ob}), the photospheric luminosity (L_{ph}) and the estimated radial velocity. Similarly, in Table 6 we present the final sample of YSO candidates.

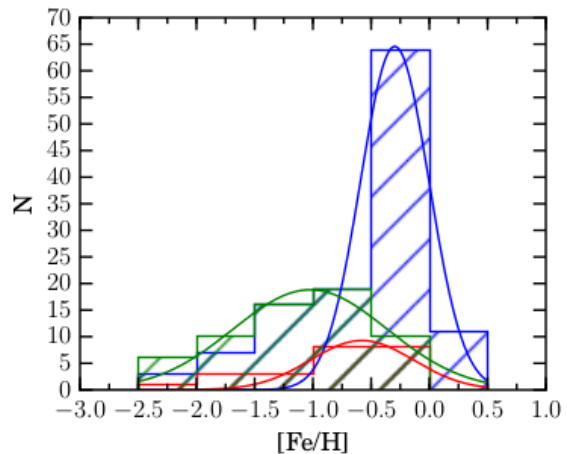


Figure 7. Histograms showing the $[\text{Fe}/\text{H}]$ distribution for the post-AGB, post-RGB and YSO candidates. The red histogram corresponds to the post-AGB objects, green to the post-RGB objects, and blue to the YSOs. The red, green and blue curves denote individual Gaussian fits to the histograms for the post-AGB, post-RGB and YSO candidates, respectively.

⁴ Note: The post-AGB/RGB and YSO candidates for which we imposed a $[\text{Fe}/\text{H}]$ value of -0.5 (see Tables 4 – 6) have not been considered while plotting the $[\text{Fe}/\text{H}]$ distribution.

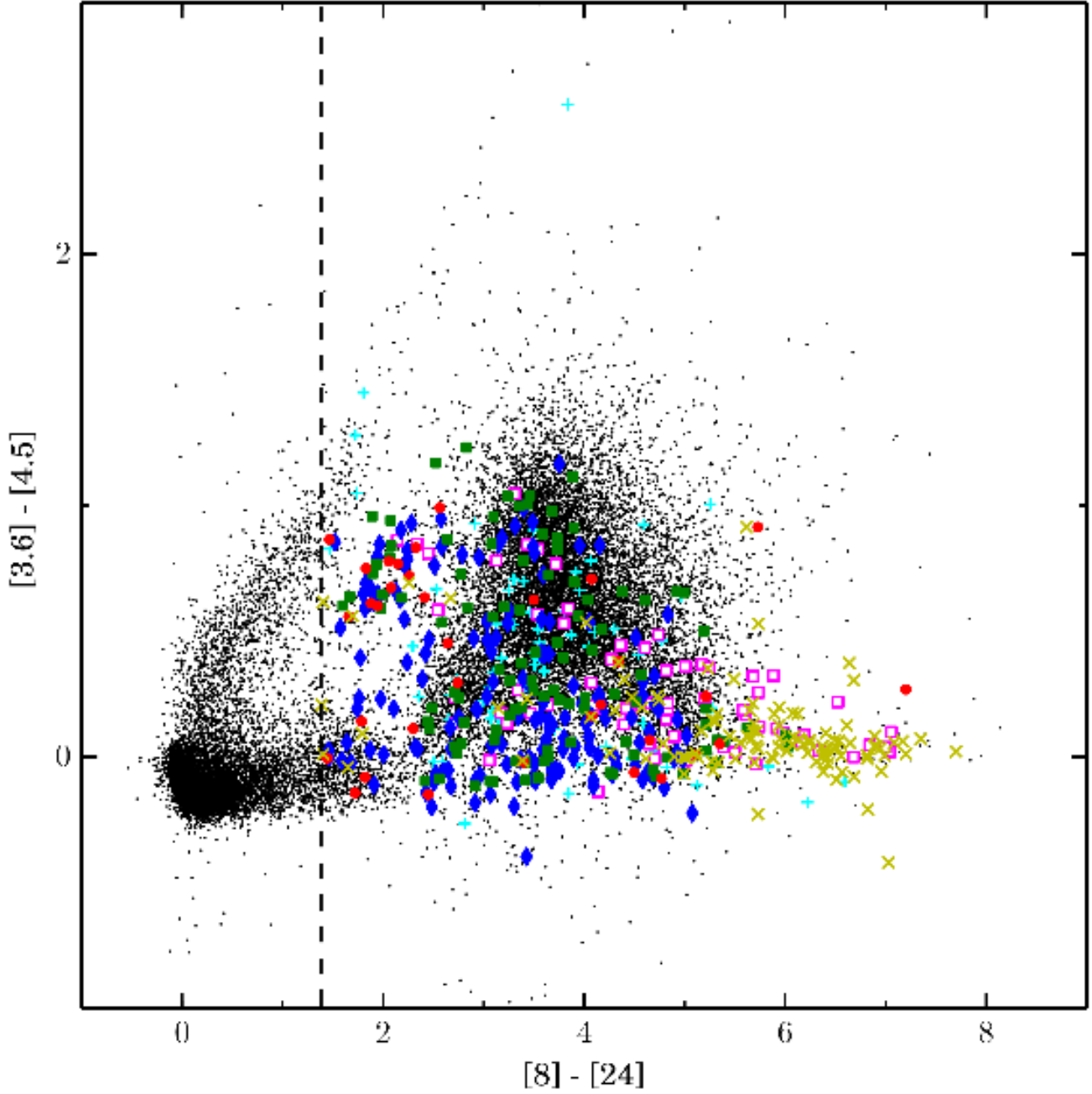


Figure 8. The spectroscopically verified post-AGB, post-RGB and YSO candidates on the colour-colour plot of $[8] - [24]$ vs $[3.6] - [4.5]$, represented by red filled-circles, green filled-squares and blue filled-diamonds, respectively. The yellow cross symbols and the magenta open-squares represent the 112 luminous objects with $L_{\text{ph}} \geq 35000 L_{\odot}$ and the 68 likely main-sequence stars with early-A, O and B candidates, respectively. The cyan plus symbols represent the 85 likely post-AGB, post-RGB and YSO candidates without a detection in the B and I bands. In each of the groups, objects that do not have detections at $[3.6]$ or $[4.5]$ microns do not appear in this plot.

Table 4: The observational and stellar parameters for the post-AGB candidates.

Name	T_{eff} (K)	$\log g$	$[\text{Fe}/\text{H}]$	$E(B-V)$	$(L_{\text{ob}}/L_{\odot})$	$(L_{\text{ph}}/L_{\odot})$	V (mags)	RV (km/s)	M/M_{\odot}	SED	$H\alpha$ FWHM	[OIII]	Previous identifications
Candidates with $[\text{Fe}/\text{H}]$ estimates from spectra													
J045119.94-670604.8	8280	1.0	-0.4	1.11	790	7921	17.0	270 ± 5	0.63	Shell	e	5.0	-
J045526.98-665032.0 ^a	4267	0.5	-0.6	0.02	4240	2601	15.5	296 ± 3	0.54	Disc	a	-	OSARG-AGB ²³
J045623.21-692749.0	4500	0.0	-1.0	0.14	6864	7131	14.6	246 ± 2	0.62	Disc	a	-	LPV ⁴ , O-AGB ²⁹ , YSO-hp ²⁸ , pagb-disc ²⁵
J045635.23-682732.9 ^a	3730	0.5	-0.5	0.01	4116	5161	15.6	238 ± 2	0.58	Disc	e	5.5	Evolved ²⁸ , YSO ⁵ , pagb-uncer ²⁵
J050221.17-691317.2 ^a	5229	0.5	-0.6	0.02	5328	4795	14.3	272 ± 3	0.58	Shell	a	-	-
J050632.10-714229.8	7614	0.5	-0.4	0.26	4910	7606	14.3	287 ± 8	0.62	Shell	a	-	CEP ²⁵ , star ⁵ , pagb-shell ²⁵ , pagb-s ²⁶
J051351.32-704656.4	4500	0.5	-0.9	0.85	1631	4130	17.4	293 ± 2	0.56	Disc	a	-	LPV ⁴ , OSARG-RGB ²³ , YSO ²⁸
J051418.09-691234.9	6112	0.5	-1.6	0.14	6667	4703	14.6	354 ± 6	0.57	Disc	e	5.5	CEP ²⁵ , EB ¹ , Evolved ²⁸ , O-PAGB(RVT) ²⁹ , RVT ^{21,25} , pagb-disc ²⁵
J051848.84-700247.0	6015	0.0	-1.0	0.81	4477	14112	15.4	250 ± 3	0.73	Shell	a	-	Evolved ²⁸ , LPV ⁴ , YSO ⁵ , SRV-AGB ²³ , pagb-shell ²⁵
J051906.86-694153.9	5613	0.0	-1.3	0.37	2052	4246	15.5	270 ± 1	0.57	Shell	e	5.5	PN ⁷
J052147.95-700957.0	4500	0.0	-0.8	0.84	6350	21517	15.2	262 ± 3	0.86	Disc	a	-	OTHER(RCB) ²⁹ , RCB ²² , RCB ²⁴
J052204.24-691520.7	6179	0.5	-1.9	0.04	4071	3753	14.5	308 ± 7	0.56	Disc	e, a	2.9	SRV-AGB ²³ , YSO ²⁸
J052218.52-695013.3	4500	0.5	-0.8	0.84	5916	6303	16.9	262 ± 2	0.6	Disc	a	-	YSO ²⁸
J052220.98-692001.5	5845	0.5	-0.5	0.35	3321	2698	15.8	275 ± 2	0.54	Shell	a	-	LPV ⁴ , SRV-AGB ²³ , YSO-hp ²⁸
J052243.99-693828.0	4500	0.5	-1.6	0.14	13480	4870	15.0	231 ± 3	0.58	Disc	e	5.8	LPV ⁴ , PN ¹⁶
J052315.15-695801.7	6061	0.5	-0.8	1.17	3810	7284	17.3	257 ± 5	0.62	Disc	e	4.3	AGB/post-AGB ⁵ , Evolved ²⁸ , LPV ⁴ , SRV-AGB ²³
J052351.13-680712.2	4500	0.5	-0.5	0.82	11065	7834	16.7	287 ± 2	0.63	Disc	a	-	YSO ²⁹ , YSO-hp ²⁸
J052557.32-680450.5	4500	1.0	-0.7	0.27	2508	2686	16.0	274 ± 1	0.54	Disc	a	-	OSARG-RGB ²³
J052604.53-685737.6	4500	1.0	-0.7	0.57	2035	2929	16.9	288 ± 1	0.54	Disc	a	-	LPV ⁴ , YSO ²⁸
J053116.74-690104.1†	5843	0.0	-1.9	1.50	5369	14696	17.6	275 ± 12	0.74	Disc	e, a	4.2	LPV ⁴ , OSARG-AGB ²³
J053250.69-713925.8	6073	1.0	-1.1	0.60	4223	11056	15.1	315 ± 5	0.68	Shell	a	-	LPV ⁴ , PAGB-s ²⁶ , YSO ⁵ , SRV-AGB ²³ , pagb-shell ²⁵
J053530.00-712941.6	6012	0.5	-1.7	0.81	1095	4207	16.8	252 ± 4	0.57	Uncer	a	-	-
J054218.24-695249.4†	5060	0.5	-0.5	0.51	4625	6200	15.6	258 ± 2	0.6	Disc	e	5.5	Evolved ²⁸
J055122.52-695351.4	6237	1.5	-2.5	0.24	3780	3657	15.2	331 ± 8	0.56	Disc	e	4.9	CEP ²⁵ , O-PAGB(RVT) ²⁹ , RVT ^{21,25} , star ⁵ , YSO ⁹ , pagb-uncer ²⁵
Candidates with $[\text{Fe}/\text{H}] = -0.50$													
J051044.47-691233.0	10544	2.0	-0.5	0.39	2038	5340	15.6	207 ± 7	0.59	Disc	e	7.9	EB ¹ , YSO ⁹ , YSO-hp ²⁸
J052116.15-674511.7	8327	1.5	-0.5	0.44	4084	8527	14.8	248 ± 4	0.64	Disc	e, a	12.0	YSO ²⁸
J052222.95-684101.2	10437	2.0	-0.5	0.89	1755	3168	17.7	288 ± 12	0.55	Disc	e	11.3	YSO ^{5,9,10,29} , YSO ²⁹ , YSO-hp ²⁸
J052241.52-675750.2	8284	1.0	-0.5	0.07	4232	4566	14.4	293 ± 15	0.57	Shell	a	-	-
J052519.48-705410.0	8117	1.0	-0.5	0.31	3219	4943	15.0	237 ± 3	0.58	Disc	e, a	4.8	CEP ²⁵ , O-PAGB(RVT) ²⁹ , RVT ^{21,25} , pagb-disc ²⁵
J052740.75-702842.0	8283	1.0	-0.5	0.04	4961	5123	14.1	263 ± 51	0.58	Shell	e	9.1	YSO-hp ²⁸
J052947.62-682819.0	8274	1.0	-0.5	0.10	16797	3073	14.9	191 ± 7	0.55	Disc	e	7.6	-
J053937.58-701544.9	8284	1.0	-0.5	0.55	3577	5400	15.7	301 ± 6	0.59	Disc	e	9.6	Evolved ²⁸
J054013.09-691716.0	8281	1.0	-0.5	0.12	2546	2754	15.1	197 ± 28	0.54	Shell	e	6.0	Evolved ²⁸
J054042.24-695743.0	8284	1.0	-0.5	0.16	4590	7634	14.1	225 ± 26	0.62	Disc	e	6.5	OSARG-RGB ²³ , YSO-hp ²⁸
J054246.93-683319.7	8313	1.0	-0.5	0.35	1780	3607	15.5	322 ± 4	0.56	Uncer	e, a	5.7	-

Notes: $(L_{\text{ob}}/L_{\odot})$ is the observed luminosity corrected for foreground extinction, $(L_{\text{ph}}/L_{\odot})$ is the photospheric luminosity of the central star, V is the optical V-band magnitude, M/M_{\odot} is the derived mass of the post-AGB candidate (see Section 7). The SED column lists the SED type of the object (see Section 8). $H\alpha$ and OIII represents the nature of the $H\alpha$ and OIII lines at 6562.8 Å and 5001 Å, respectively. 'e', 'a', 'e,a' and 'a,e' represent emission, absorption and dominant emission with an absorption component and dominant absorption with an emission component, respectively. '-', indicates no detection. FWHM (in Å) represents the full width at half maximum of the $H\alpha$ line. The column 'Previous identifications' gives the result of a positional cross-matching that was done with the following catalogues: ¹Alcock et al. (2002), ²Bonanos et al. (2009), ³Cioni et al. (2013), ⁴Fraser et al. (2008), ⁵Gruendl & Chu (2009), ⁶Groenewegen et al. (2009), ⁷Hora et al. (2008), ⁸Kontizas et al. (2001), ⁹Kozłowski & Kochanek (2009), ¹⁰Kozłowski et al. (2012), ¹¹Levato et al. (2014), ¹²Miszalski et al. (2011), ¹³Matsuura et al. (2014), ¹⁴Morgan et al. (2003), ¹⁵Neugent et al. (2012), ¹⁶Reid & Parker (2006), ¹⁷Reid & Parker (2010), ¹⁸Reid & Parker (2013), ¹⁹Reid et al. (2009), ²⁰Seale et al. (2009), ²¹Soszyński et al. (2008), ²²Soszyński et al. (2009b), ²³Soszyński et al. (2009a), ²⁴Tisserand et al. (2009), ²⁵van Aarle et al. (2011), ²⁶van Aarle et al. (2013), ²⁷Volk et al. (2011), ²⁸Whitney et al. (2008), ²⁹Woods et al. (2011), ³⁰Yang & Jiang (2011), ³¹Zickgraf (2006). Catalogue identifications: OSARG-AGB =

OGLE small amplitude red giant - AGB star, OSARG-RGB = OGLE small amplitude red giant - RGB star, LPV = long period variable, O-AGB = oxygen-rich AGB, YSO-hp = high probability YSO candidate, pagb-disc = post-AGB with disc-type SED, pagb-shell = post-AGB with shell-type SED, pagb-uncer = post-AGB with uncertain-type SED, YSO = young stellar object, Evolved = evolved object, CEP = Cepheid variable, RVT = RV-Tauri, O-PAGB = oxygen-rich post-AGB, PAGB-s = *s*-process enriched post-AGB star, PN = planetary nebula, SRV-AGB = semi-regular variable AGB star, SRV-RGB = semi-regular variable RGB star, EB = eclipsing binary, RCB = **R Coronae Borealis star**. See catalogued references for full details of the individual object identification.

The superscript 'a' in the first column indicates that the T_{eff} value used to estimate $E(B - V)$ is increased by 250K (see Subsection 6.2 for further details). The superscript † in the first column indicates that based on their spectra, J053116.74-690104.1 and J054218.24-695249.4 are likely symbiotic objects.

Table 5: The observational and stellar parameters for the post-RGB candidates.

Name	T_{eff} (K)	$\log g$	$[\text{Fe}/\text{H}]$	$E(B-V)$	$(L_{\text{ob}}/L_{\odot})$	$(L_{\text{ph}}/L_{\odot})$	V (mags)	RV (km/s)	M/M_{\odot}	SED	H α FWHM	[OIII]	Previous identifications
Candidates with [Fe/H] estimates from spectra													
J043919.30-685733.4	6313	1.5	-2.0	0.32	106	159	18.8	352 ± 13	0.3	Shell	a	-	-
J043948.92-693828.9	4928	0.5	-1.6	0.23	368	350	17.9	212 ± 5	0.34	Uncer	a	-	-
J045243.16-704737.3	5685	0.5	-1.2	0.25	2045	2284	15.7	266 ± 3	0.45	Disc	e,a	4.8	YSO ^{9,28} , pagb-disc ²⁵
J045625.46-695130.7	4761	1.5	-0.5	0.28	490	639	17.5	259 ± 6	0.37	Uncer	-	-	-
J045739.78-694854.2	5819	1.5	-1.2	0.04	969	142	18.1	232 ± 6	0.3	Uncer	e,a	3.0	-
J045755.05-681649.2	4927	1.5	-0.3	0.2	190	215	18.3	231 ± 25	0.32	Disc	e	4.8	-
J045806.79-694855.8	4575	1.5	-0.8	0.25	434	507	17.8	263 ± 6	0.36	Uncer	-	-	-
J045815.58-662507.0	5303	1.0	-1.1	0.06	293	236	17.7	287 ± 20	0.32	Shell	e	5.2	e
J045840.99-693433.5	4500	1.0	-0.5	0.2	875	757	17.2	243 ± 8	0.38	Uncer	e	4.3	G ⁵
J050252.50-681705.9	5318	1.0	-1.6	0.5	241	374	18.6	200 ± 16	0.34	Uncer	a	-	QSO ⁹
J050304.95-684024.7	5586	0.5	-2.3	0.01	3251	2091	15.1	332 ± 5	0.44	Disc	e	5.2	CEP ²⁵ , EB ¹ , O-PAGB(RVT) ²⁹ , RVT ^{21,25} , S ⁵ , YSO ⁹ , pagb-disc ²⁵
J050353.52-684703.8	5087	0.5	-1.5	0.16	287	286	17.9	315 ± 16	0.33	Uncer	a	-	-
J050554.76-664708.1	4500	0.5	-1.3	0.68	1394	2390	17.5	275 ± 7	0.45	Disc	a	-	OSARG-RGB ²³ , star ⁵
J050617.59-690537.7	5911	1.5	-1.5	0.1	367	368	17.2	295 ± 8	0.34	Disc	-	-	QSO ⁹
J050738.94-682005.9	5420	1.5	-1.0	0.13	859	664	16.8	321 ± 3	0.37	Disc	e,a	6.4	EB ¹ , Evolved ²⁸ , WVir ²¹ , YSO ⁹
J050817.90-684315.6	5653	0.5	-1.4	0.57	487	1269	17.4	261 ± 4	0.41	Uncer	e	5.3	e
J051046.68-690850.0	4750	1.0	-0.9	0.21	1018	1094	16.7	256 ± 2	0.4	Shell	e,a	5.7	-
J051113.66-700357.2	8296	1.0	-2.5	0.13	1453	1658	15.7	280 ± 4	0.43	Shell	e	4.9	-
J051230.14-682708.9	4720	1.5	-1.0	0.0	123	102	18.6	273 ± 18	0.28	Shell	e,a	3.0	-
J051240.23-722249.5	7220	1.5	-1.9	0.04	1197	677	16.3	255 ± 10	0.37	Disc	a	-	-
J051259.43-691223.1	4401	1.0	-0.7	0.48	1077	1430	17.4	335 ± 2	0.42	Disc	e	5.5	e
J051347.57-704450.5	4500	1.0	-0.5	0.2	712	840	17.1	234 ± 3	0.39	Shell	a	-	-
J051453.10-691723.5	4123	0.5	-0.5	0.05	2616	2171	16.0	276 ± 1	0.44	Uncer	e,a	4.9	e
J051652.53-702143.2	6795	1.0	-0.8	0.63	283	955	17.7	306 ± 10	0.39	Uncer	-	-	Evolved ²⁸ , O-PAGB ²⁹ , YSO ⁵ , pagb-uncer ²⁵
J051728.71-694246.7	5161	0.5	-1.0	0.2	546	487	17.4	206 ± 1	0.36	Shell	e	5.0	e
J051752.75-695819.1	5280	1.0	-1.1	0.09	235	104	18.7	226 ± 10	0.29	Disc	e	5.0	-
J051821.10-684922.4	6752	1.0	-2.1	0.04	1912	1315	15.6	296 ± 9	0.41	Disc	e,a	3.5	YSO ^{9,28}
J051916.88-693757.3	4500	0.0	-2.5	0.06	10022	210	18.3	191 ± 9	0.32	Shell	e	5.1	e
J051920.18-722522.1	4500	1.5	-1.5	0.13	496	507	17.4	177 ± 4	0.36	Shell	a	-	-
J051924.80-701152.8	4500	1.0	-1.5	0.06	335	335	17.7	198 ± 4	0.34	Uncer	-	-	-
J051942.32-690535.4	4500	0.5	-1.0	0.12	2123	1718	16.1	257 ± 2	0.43	Disc	e	4.2	-
J052034.21-693822.1	5992	0.5	-1.2	0.02	1622	588	16.4	263 ± 2	0.37	Uncer	e	5.2	e
J052047.95-692948.7	5721	1.5	-1.9	0.29	238	430	17.7	237 ± 7	0.35	Shell	e	5.1	e
J052115.71-702106.2	6185	1.0	-2.5	0.46	277	700	17.6	218 ± 9	0.38	Shell	a	-	-
J052118.97-690103.6	4500	1.5	-0.2	0.13	584	554	17.3	284 ± 5	0.36	Disc	e	6.0	-
J052135.62-695157.1	4500	0.5	-0.8	0.32	1753	2114	16.5	271 ± 2	0.44	Uncer	a	-	OSARG-AGB ²³
J052203.30-681921.4	5430	1.5	-1.0	0.44	1786	1027	17.3	291 ± 3	0.4	Disc	e	3.2	-
J052411.12-692126.7	5387	1.0	-1.7	0.0	346	164	17.9	224 ± 10	0.3	Disc	e	5.1	e
J052500.40-721845.3	4652	1.5	-2.5	0.16	163	197	18.4	256 ± 11	0.31	Disc	-	-	-
J052546.81-722256.8 ^b	5000	1.0	-1.9	0.04	257	202	17.9	250 ± 6	0.31	Shell	a	-	-
J052548.17-693700.1	4500	0.5	-0.9	0.12	854	818	16.9	246 ± 2	0.38	Uncer	e,a	5.7	e
J052819.91-681834.2 ^b	5000	1.5	-1.9	0.04	145	132	18.4	276 ± 5	0.3	Shell	e	3.9	-
J052849.25-674125.3	4500	1.5	-1.9	0.02	193	155	18.4	282 ± 5	0.3	Uncer	e,a	4.9	e
J053030.78-701805.5	4500	2.0	-1.4	0.03	167	130	18.6	205 ± 7	0.29	Disc	e	3.9	-
J053045.83-705016.5	4500	1.0	-0.8	0.18	952	1170	16.7	227 ± 2	0.41	Shell	e	5.5	e
J053206.81-702101.9	4656	1.0	-1.3	0.07	286	289	17.7	222 ± 3	0.33	Uncer	-	-	PN7.16

Table 5: continued.

Name	T_{eff} (K)	$\log g$	[Fe/H]	$E(B-V)$	$(L_{\text{ob}}/L_{\odot})$	$(L_{\text{ph}}/L_{\odot})$	V (mags)	RV (km/s)	M/M_{\odot}	SED	H α FWHM [OIII]	Previous identifications		
J053253.54-714703.7 ^b	6310	1.0	-1.0	0.02	789	621	16.3	267 ± 10	0.37	Disc	a	-	AGN ¹⁰ , YSO ⁹	
J053514.93-680010.8	4500	0.5	-1.1	0.27	1169	1440	16.7	256 ± 2	0.42	Uncer	a	-	-	
J053528.64-683746.2	4500	1.5	-1.9	0.07	120	130	18.7	254 ± 1	0.29	Uncer	e	2.0	-	
J053547.36-700625.4	4054	0.5	-0.5	0.16	1343	1639	16.7	282 ± 1	0.43	Disc	a	-	OSARG-AGB ²³	
J053628.41-701256.1	5244	2.0	-0.6	0.09	288	347	17.4	257 ± 3	0.34	Uncer	a	-	-	
J053851.10-713301.2	5250	1.5	-1.2	0.07	106	92	18.8	264 ± 10	0.28	Shell	a	-	-	
J053930.60-702248.5	4315	0.5	-0.9	0.14	248	294	18.2	262 ± 2	0.33	Shell	-	e	-	
J054024.49-692950.4	5343	1.0	-1.4	0.67	453	1080	18.0	262 ± 11	0.4	Shell	e	5.2	e	
J054054.35-701318.6	4822	1.5	-0.5	0.05	488	387	17.3	280 ± 4	0.35	Disc	e	6.1	-	YSO ⁵ , QSO ⁹
J054115.40-711248.9	5037	1.0	-1.5	0.28	332	372	18.0	259 ± 4	0.34	Uncer	e	5.0	-	-
J054144.88-712351.7	5262	2.0	-0.7	0.03	125	91	18.6	252 ± 5	0.28	Disc	e	5.6	-	AGN ¹⁰ , QSO ⁹
J054228.75-693021.2	5547	0.5	-2.5	0.07	1123	1107	16.0	365 ± 17	0.4	Disc	e	5.5	e	-
J054249.59-705015.2	4500	1.0	-0.5	0.26	609	850	17.3	227 ± 2	0.39	Uncer	a	-	-	-
J054306.57-713038.3	5843	1.5	-0.9	0.06	193	84	18.7	296 ± 27	0.28	Shell	a	-	-	-
J054555.68-705730.3	3902	0.0	-1.0	0.14	1973	2147	16.4	239 ± 1	0.44	Disc	a	-	-	LPV ⁴ , OSARG-RGB ²³
Candidates with [Fe/H] = -0.50														
J044049.73-684419.0	8607	2.5	-0.5	0.72	129	511	18.8	210 ± 21	0.36	Uncer	a	-	-	-
J044931.84-691551.6	7655	1.5	-0.5	0.1	297	111	18.4	265 ± 20	0.29	Disc	e	5.5	e	-
J045058.16-671634.4	7625	2.5	-0.5	0.21	250	200	18.1	212 ± 16	0.31	Disc	a	-	-	QSO ⁹
J045339.50-672833.5	7734	1.0	-0.5	0.16	588	715	16.6	282 ± 9	0.38	Disc	e, a	5.0	-	QSO ⁹
J045539.61-681202.9	7625	1.5	-0.5	1.19	212	1609	18.9	293 ± 20	0.42	Uncer	-	-	-	-
J045555.15-712112.3	10000	2.0	-0.5	0.09	454	191	18.2	240 ± 15	0.31	Disc	e	5.3	-	YSO ⁵
J045636.68-710226.2	9054	2.0	-0.5	0.7	134	524	18.8	255 ± 23	0.36	Disc	a	-	-	QSO ^{9,10}
J045736.84-705127.2	10000	2.0	-0.5	0.07	80	88	18.9	292 ± 34	0.28	Disc	a	-	-	QSO ^{9,10}
J045745.46-683724.1	7626	3.0	-0.5	0.1	121	118	18.4	276 ± 24	0.29	Disc	a	-	-	QSO ⁹
J045836.92-701120.1	8000	1.0	-0.5	0.12	277	95	18.7	261 ± 32	0.28	Disc	a	-	-	G ⁵ , QSO ^{9,10}
J045923.34-703157.3	9111	1.5	-0.5	0.17	2601	470	17.3	266 ± 17	0.36	Disc	e	5.9	-	YSO ^{8,5}
J050009.35-673506.7	8000	1.0	-0.5	0.08	307	137	18.1	223 ± 18	0.3	Disc	a	-	-	QSO ⁹
J050117.17-675033.6	8000	1.0	-0.5	0.9	214	1177	18.4	290 ± 23	0.41	Uncer	a	-	-	-
J050149.27-664935.4	7000	1.0	-0.5	0.89	274	2030	17.7	250 ± 16	0.44	Uncer	a	-	-	G ⁵
J050204.10-655017.7	9948	2.0	-0.5	0.06	145	83	19.0	301 ± 20	0.28	Disc	e	4.6	-	-
J050257.89-665306.3	4586	0.5	-0.5	0.12	267	177	18.5	254 ± 22	0.31	Disc	-	-	-	-
J050338.50-671754.4	7625	2.5	-0.5	0.53	367	379	18.4	272 ± 7	0.34	Disc	e	5.5	e	QSO ⁹ , YSO-hp ²⁸
J050452.48-701201.0	8250	1.0	-0.5	0.01	820	443	16.7	276 ± 8	0.35	Uncer	e	5.4	e	-
J050458.28-703102.4	10000	2.0	-0.5	0.45	310	1187	17.3	249 ± 9	0.41	Uncer	e	5.2	e	-
J050503.65-660841.9	7500	1.0	-0.5	0.77	174	809	18.3	258 ± 12	0.38	Uncer	a	-	-	-
J050504.15-684440.8 [†]	8332	1.0	-0.5	0.2	1232	1346	16.1	280 ± 13	0.41	Disc	e	10.2	-	YSO ⁹
J050515.28-713403.8	4864	1.0	-0.5	0.35	202	290	18.6	196 ± 11	0.33	Uncer	a	-	-	G ⁵
J050627.11-713800.0	6260	2.0	-0.5	0.58	208	353	18.7	251 ± 11	0.34	Uncer	a	-	-	-
J050723.82-661510.3	5576	1.0	-0.5	0.42	211	299	18.5	264 ± 12	0.33	Uncer	a	-	-	-
J050954.58-684947.3	7658	1.0	-0.5	0.05	2178	113	18.2	170 ± 14	0.29	Uncer	e	5.3	e	YSO ⁵ , YSO-P ²⁰
J051012.81-685535.9	7250	0.5	-0.5	0.33	2501	354	17.8	233 ± 10	0.34	Uncer	e	5.3	e	YSO ⁵
J051101.61-705221.4	4500	1.0	-0.5	0.11	729	547	17.3	251 ± 2	0.36	Disc	a	-	-	Evolved ²⁸ , S ⁵ , YSO ⁹
J051228.19-690755.8	8289	1.0	-0.5	0.17	2923	1164	16.2	203 ± 22	0.41	Disc	e	5.4	-	C-PAGB ²⁹ , C-PPNe ²⁷ , YSO ⁵ , YSO ²⁸
J051412.13-702026.0	7626	3.0	-0.5	0.11	173	117	18.4	244 ± 14	0.29	Disc	a	-	-	QSO ^{9,10}
J051503.27-703351.0	5794	2.0	-0.5	0.13	3204	145	18.3	314 ± 31	0.3	Disc	e	6.5	-	YSO ⁵ , YSO-P ²⁰ , YSO ²⁸
J051627.12-692623.0	7699	1.0	-0.5	0.08	753	263	17.4	306 ± 13	0.33	Disc	e	8.0	e	YSO ⁹ , YSO-hp ²⁸

Table 5: continued.

Name	T_{eff} (K)	$\log g$	[Fe/H]	$E(B-V)$	$(L_{\text{ob}}/L_{\odot})$	$(L_{\text{ph}}/L_{\odot})$	V (mags)	RV (km/s)	M/M_{\odot}	SED	H α FWHM [OIII]	Previous identifications
J051751.41-7113507.3	8124	2.0	-0.5	0.15	129	85	18.9	238 ± 16	0.28	Disc	a	-
J052009.57-683800.5	7681	1.5	-0.5	0.46	2123	2058	16.4	301 ± 7	0.44	Disc	e,a	12.6
J052034.42-700033.1	7734	1.0	-0.5	0.37	708	781	17.1	243 ± 14	0.38	Disc	e	7.7
J052107.90-714104.4	10000	2.5	-0.5	0.08	126	114	18.7	355 ± 42	0.29	Disc	e,a	6.2
J052115.92-693226.0	9875	2.0	-0.5	0.03	684	607	16.7	243 ± 12	0.37	Disc	e	4.6
J052128.28-681324.9	7675	1.5	-0.5	0.05	373	113	18.2	255 ± 32	0.29	Uncer	-	-
J052245.11-713610.2†	8289	1.0	-0.5	0.66	5539	1413	17.5	186 ± 10	0.42	Disc	e	6.8
J052300.15-681120.8	8291	1.0	-0.5	0.28	997	1541	16.2	266 ± 15	0.42	Shell	e	9.2
J052603.31-684220.0	8290	1.0	-0.5	0.02	1236	1366	15.5	319 ± 11	0.41	Shell	e,a	5.1
J052834.16-715558.1†	9964	2.0	-0.5	0.31	2788	1148	16.9	335 ± 13	0.4	Disc	e	7.2
J052902.80-682321.4	7641	2.0	-0.5	0.06	95	79	18.7	196 ± 16	0.27	Uncer	-	-
J053102.33-682952.6	8297	1.0	-0.5	0.06	528	528	16.7	284 ± 17	0.36	Shell	e,a	4.9
J053130.65-714448.2†	8294	1.0	-0.5	0.24	2155	968	16.6	246 ± 7	0.39	Disc	e	8.1
J053305.75-673844.0	10000	2.0	-0.5	0.06	187	116	18.6	322 ± 19	0.29	Uncer	e,a	5.3
J053431.48-683513.7	8322	1.0	-0.5	0.01	4973	532	16.5	250 ± 11	0.36	Disc	e	6.2
J053452.18-695649.6	7665	2.0	-0.5	0.04	123	123	18.1	259 ± 47	0.29	Shell	e	4.7
J053804.72-695918.5	7655	1.0	-0.5	0.06	941	128	18.1	175 ± 8	0.29	Disc	e	7.7
J053811.63-680824.9	4935	2.0	-0.5	0.02	99	81	18.8	311 ± 15	0.28	Disc	-	-
J053907.26-693514.5	8292	1.0	-0.5	-0.0	2065	1182	15.6	192 ± 9	0.41	Uncer	e	5.2
J053925.37-674653.8	10000	2.0	-0.5	0.02	1055	970	16.2	330 ± 23	0.39	Disc	-	-
J054034.77-683228.2	8250	1.0	-0.5	0.15	845	906	16.4	240 ± 32	0.39	Uncer	e	5.0
J054038.64-702800.5	8129	1.0	-0.5	0.35	1922	249	18.4	293 ± 45	0.32	Disc	e	6.8
J054038.99-694850.2	8286	1.0	-0.5	0.06	1716	2095	15.2	319 ± 16	0.44	Shell	e	5.2
J054051.04-700712.9	5278	2.5	-0.5	0.1	78	83	19.0	272 ± 10	0.28	Uncer	e	4.2
J054551.75-702005.0	6533	2.0	-0.5	0.58	157	342	18.7	289 ± 8	0.34	Disc	-	-
J054849.92-682918.6	10500	2.0	-0.5	1.09	237	2139	18.8	270 ± 31	0.44	Uncer	e,a	3.8
J055102.44-685639.1	7625	1.0	-0.5	0.94	452	815	18.9	352 ± 39	0.38	Disc	e,a	-

Notes: As for Table 4.

The column "Previous identifications" gives the result of a positional cross-matching that was done with the catalogues mentioned in Table 4. Catalogue identifications: YSO = young stellar object, YSO-P = YSO with PAH emission features, YSO-hp = high probability YSO candidate, pagb-disc = post-AGB with disc-type SED, pagb-uncer = post-AGB with uncertain-type SED, G = background galaxy, QSO = quasi-stellar object, Evolved = evolved object, PN = planetary nebula, OSARG-RGB = OGLE small amplitude red giant - RGB star, OSARG-AGB = OGLE small amplitude red giant - AGB star, C-PPNe = carbon-rich proto-planetary nebula, EB = eclipsing binary, RRLab - RR Lyrae, C-PAGB = carbon-rich post-AGB, RVt = RV-Tauri, O-PAGB = oxygen-rich post-AGB, LPV = long period variable, AGN = active galactic nuclei, WVir = W Virginis star, HII = HII region. See catalogued references for full details of the individual object identification.

The superscript 'b' in the first column indicates that the T_{eff} value used to estimate $E(B-V)$ is increased by 500K (see Subsection 6.2 for further details).

†J050504.15-684440.8, J052245.11-713610.2, J052834.16-715558.1 and J053130.65-714448.2 show FeII emission line features similar to that of B[e] stars (see Section 4).

Table 6: The observational and stellar parameters for the YSO candidates.

Name	T_{eff} (K)	$\log g$	$[\text{Fe}/\text{H}]$	$E(B-V)$	$(L_{\text{ob}}/L_{\odot})$	$(L_{\text{ph}}/L_{\odot})$	V (mags)	RV (km/s)	$H\alpha$ FWHM [OIII]	Previous identifications
Candidates with $[\text{Fe}/\text{H}]$ estimates from spectra										
J044535.72-685840.4	5313	3.0	-1.0	0.31	224	329	18.2	210 ± 16	-	-
J044920.32-690900.0	4500	1.0	-0.3	0.5	4169	6564	15.8	263 ± 2	-	-
J044937.42-682924.9	5484	3.0	-0.1	0.15	233	138	18.5	290 ± 12	-	-
J045009.84-701320.9	4500	1.5	-0.1	0.38	798	1116	17.3	227 ± 3	a	-
J045145.31-692837.1	4500	2.0	-0.7	0.61	1888	3173	16.9	277 ± 3	e	4.0 LPV ⁴ , OSARG-RGB ²³
J045216.81-713421.5	7486	4.0	-0.7	0.7	118	457	18.8	278 ± 9	a	-
J045253.76-664029.2	4416	1.5	-0.4	0.45	1805	2579	16.6	262 ± 4	a	-
J045330.56-695150.7	4500	1.5	-0.1	0.43	2074	2774	16.5	253 ± 1	-	YSO ²⁸ OSARG-RGB ²³
J045424.37-685240.6	5756	3.0	-0.0	0.11	267	274	17.6	245 ± 12	e	5.6 QSO ⁹ G ⁵
J045445.18-680656.4	7007	3.5	-1.4	0.83	335	1342	18.1	312 ± 13	a	-
J045500.50-675115.7	4500	2.0	-0.6	0.23	577	634	17.5	243 ± 11	a	-
J045552.51-664517.2	3944	1.0	-0.5	0.22	2250	2504	16.4	211 ± 3	a	-
J045601.49-683958.2	7627	3.5	-0.6	0.12	332	251	17.6	226 ± 18	e	5.4 SRV-AGB ²³
J045607.04-712422.3	4500	1.5	-0.4	0.3	1141	1567	16.7	249 ± 1	a	-
J045638.17-670352.3	4500	1.5	-1.7	0.06	949	978	16.5	359 ± 13	a	-
J045639.01-694846.2	4500	2.0	-0.9	0.16	363	414	17.7	238 ± 7	a	-
J045749.15-715407.5	6271	3.0	-1.6	0.28	421	812	17.0	254 ± 16	a	-
J045815.38-684658.5	7187	3.5	-1.6	0.6	167	421	18.6	257 ± 13	e	5.3 QSO ⁹
J045908.22-703254.1	4500	2.5	-1.0	0.59	2843	5455	16.3	236 ± 3	e	5.9 QSO ⁹ , LPV ⁴ , LPV-C ¹ , SRV-AGB ²³
J045913.17-705029.9	4500	1.5	-0.5	0.89	2601	5316	17.2	235 ± 2	e	5.8 LPV ⁴ , LPV-C ¹ , SRV-AGB ²³
J050017.38-680143.4	7168	3.0	-2.2	0.53	465	405	18.4	211 ± 17	e _a	3.5 e
J050022.04-713802.2	5113	3.0	-0.2	0.1	347	428	17.3	278 ± 2	a	-
J050022.37-691413.6	5855	2.5	-0.6	0.96	942	4707	17.2	241 ± 6	e	3.9
J050055.66-720013.5	5019	3.0	-0.5	0.35	430	554	17.8	259 ± 3	a	-
J050150.72-700450.0	5120	3.0	-0.2	0.37	540	882	17.3	233 ± 8	e	5.4
J050201.73-673419.2	6423	3.0	-0.9	0.17	422	584	16.9	345 ± 8	e	5.8
J050217.28-685428.5	6195	3.5	-0.3	0.14	85	89	18.9	211 ± 9	a	-
J050232.06-690501.5	8211	2.0	-0.0	0.22	2654	4879	14.7	341 ± 9	a	-
J050252.54-674848.6	4922	2.0	-0.6	0.3	427	560	17.6	244 ± 4	a	-
J050305.55-712846.3	4747	2.5	-1.1	0.1	166	114	18.8	261 ± 19	a	-
J050335.39-700347.2	4500	1.0	-0.4	0.19	2848	3332	15.5	256 ± 1	a	-
J050431.87-701037.0	5771	3.0	-2.5	0.13	646	146	18.5	327 ± 15	e	5.3 YSO ⁵
J050503.87-683210.7	7631	3.5	-1.6	0.79	166	550	18.9	263 ± 10	e	3.8
J050524.47-670125.4	5145	2.5	-0.1	0.39	519	799	17.4	246 ± 5	a	-
J050527.24-684844.5	5096	2.5	-0.5	0.3	481	949	17.0	226 ± 4	a	-
J050600.08-683714.0	4750	1.0	-0.8	0.55	3491	5701	16.0	260 ± 1	-	-
J050651.48-713030.2	5093	3.5	-1.2	0.06	96	78	19.0	252 ± 16	a	-
J050718.33-690742.9	7206	1.5	-1.1	0.05	10075	8348	13.6	329 ± 9	e _a	3.0 YSO-hp ²⁸ , pagb-uncer ²⁵
J050732.94-682925.4 ^b	7910	3.0	-1.3	0.01	512	415	16.8	270 ± 12	e _a	3.7 e
J050735.59-701546.4	5169	3.5	-0.2	0.15	95	100	18.9	282 ± 20	e _a	5.0
J050830.51-692237.4 [†]	8062	2.5	-1.7	0.09	8725	5090	14.3	287 ± 6	-	-
J050953.41-701833.8	4500	1.5	-0.4	0.34	628	866	17.5	261 ± 1	a	-
J051200.28-683819.4	4698	2.0	-0.0	0.55	1947	3763	16.4	264 ± 2	a	-
J051255.84-721644.5	4500	2.5	-1.8	0.1	182	188	18.4	203 ± 6	-	-
J051315.46-711415.0	4500	1.5	-0.5	0.32	976	1377	16.9	238 ± 2	a	-
J051443.20-685034.5	4500	2.0	-0.6	0.85	2394	6036	17.0	300 ± 4	e	5.7 LPV ⁴ , LPV-C ¹ , SRV-AGB ²³ , YSO ²⁸

Table 6: continued.

Name	T_{eff} (K)	$\log g$	[Fe/H]	$E(B-V)$	$(L_{\text{ob}}/L_{\odot})$	$(L_{\text{ph}}/L_{\odot})$	V (mags)	RV (km/s)	$H\alpha$ FWHM	O III	Previous identifications	
J051450.04-692735.3	5850	2.5	-0.5	0.29	1809	2488	15.8	260 ± 3	e, a	4.6	-	CEP ²⁵ , Evolved ²⁸ , LPV ⁴ , pagb-uncertain ²⁵
J051550.59-684105.2	6036	2.0	-0.4	0.71	764	2434	17.1	299 ± 3	-	-	-	-
J051624.89-690000.8	6837	2.0	-0.7	0.02	3761	3590	14.4	335 ± 7	a	-	-	YSO-hp ²⁸ , pagb-shell ²⁵
J051810.34-695714.1	4500	2.0	-0.1	0.4	1624	3127	16.3	212 ± 2	a	-	-	OSARG-RGB ²³
J051844.30-695357.0	6474	3.0	-1.6	0.02	517	519	16.6	289 ± 5	e	4.6	-	-
J051845.23-700534.5	6152	2.0	-1.2	1.01	4651	3930	17.5	306 ± 10	e	5.9	-	C-PAGB ²⁹ , C-PPNe ²⁷ , LPV ⁴ , S ⁵ , SRV-AGB ²³ , YSO-hp ²⁸
J051845.47-690321.8	5860	1.5	-0.8	0.11	4001	3664	14.8	261 ± 3	e	5.6	-	CEP ²⁵ , O-PAGB(RVT) ²⁹ , RVT ^{21,25} , YSO ²⁸ , pagb-disc ²⁵
J051917.29-693147.3	4500	1.5	-0.3	0.23	3800	3787	15.5	283 ± 2	-	-	-	YSO ⁵ , YSO-hp ²⁸ , pagb-uncert ²⁵
J051917.83-714359.4	4500	3.0	-0.3	0.31	953	1376	16.9	273 ± 2	a	-	-	-
J051922.13-683901.9	4500	2.5	-0.2	0.34	1416	1921	16.6	273 ± 2	e	3.6	-	-
J052106.33-711755.7	5866	3.5	-1.6	0.3	122	167	18.8	237 ± 16	e	5.1	e	-
J052141.52-710909.2	4678	2.5	-0.6	0.22	1300	1452	16.4	228 ± 2	a	-	-	YSO ⁹
J052151.46-673455.8	4500	2.0	-0.6	0.26	387	383	18.1	257 ± 3	a	-	-	-
J052159.63-710859.1	4943	3.0	-2.5	0.1	218	211	17.8	256 ± 10	e, a	3.1	-	-
J052202.91-694127.8	4895	1.5	-0.5	0.13	2362	1814	15.8	291 ± 2	e	5.4	-	YSO ⁹
J052211.94-690420.5	4500	1.5	-0.5	0.29	972	1046	17.1	217 ± 3	e, a	4.3	-	LPV ⁴ , YSO ²⁸
J052300.83-700431.1	7645	3.5	-0.3	0.04	394	477	16.7	328 ± 19	e	7.9	-	Be ¹⁰ , QSO ⁹
J052317.90-692330.0	7626	3.5	-0.0	0.71	314	1583	17.4	286 ± 4	e, a	4.3	e	-
J052338.74-700054.2	5956	2.5	-0.6	0.33	441	804	17.1	273 ± 3	e	4.7	e	-
J052410.77-705414.5	4500	1.5	-0.3	0.28	870	1101	17.0	283 ± 5	a	-	-	-
J052417.75-710708.7	5093	2.0	-0.5	0.34	444	681	17.5	296 ± 3	a	-	-	-
J052449.29-693320.4	5000	3.0	-0.5	0.29	372	542	17.6	262 ± 8	e	4.6	-	QSO ⁹ , red ¹⁰
J052507.64-702219.7	4436	2.0	-0.3	0.35	873	1170	17.2	243 ± 3	a	-	-	OSARG-RGB ²³
J052526.01-703523.9	4500	2.0	-0.4	0.31	857	1111	17.1	250 ± 2	a	-	-	-
J052533.79-674240.7	4982	3.0	-0.7	0.2	117	139	18.8	288 ± 21	-	-	-	-
J052559.42-671932.9	4500	2.0	-0.1	0.36	1173	1650	16.9	279 ± 2	e	2.5	e	-
J052602.26-690306.2	4500	2.0	-1.6	0.15	204	212	18.4	257 ± 5	e	2.4	e	-
J052608.03-704232.9	4500	2.0	-0.5	0.38	1815	2826	16.3	232 ± 2	e, a	4.7	e	G ⁵ , OSARG-RGB ²³
J052622.28-704131.2	6357	2.5	-0.7	0.04	4993	712	16.3	281 ± 5	e, a	3.8	e	OSARG-RGB ²³
J052709.99-683335.2	4500	2.5	-1.6	0.08	215	235	18.1	285 ± 3	-	-	e	-
J052715.55-701425.0	5116	3.0	-0.2	0.08	379	321	17.5	259 ± 2	a	-	e	-
J052725.04-671245.3	4888	3.0	-0.3	0.29	491	711	17.3	269 ± 2	-	-	e	-
J052728.46-702359.9	4500	1.5	-0.4	0.08	707	899	16.6	248 ± 2	a	-	-	G ⁵
J052838.12-683101.8	4500	2.0	-0.4	0.37	810	1231	17.2	257 ± 2	-	-	e	OSARG-RGB ²³
J052909.56-684258.3	4728	2.0	-1.0	0.3	739	993	17.1	277 ± 2	-	-	e	-
J052917.10-703422.1	5447	3.0	-1.8	0.43	221	374	18.4	326 ± 21	e	5.3	e	-
J052959.77-705545.9	4500	1.5	-0.5	0.23	589	725	17.3	287 ± 2	e	5.5	e	-
J053030.10-675018.0	4500	2.5	-0.4	0.25	649	802	17.3	316 ± 2	-	-	e	-
J053153.96-673845.7	4777	2.5	-0.6	0.3	2894	3438	15.7	286 ± 2	e	5.4	e	-
J053249.63-704640.8	4500	1.5	-0.3	0.15	1654	1446	16.3	245 ± 1	a	-	-	YSO ⁹ , red ¹⁰
J053253.51-695915.1	4698	1.5	-0.7	0.1	1391	1422	16.1	234 ± 2	a	-	-	CEP ²⁵ , PAGB-s ²⁶ , YSO-hp ²⁸ , pagb-disc ²⁵
J053445.96-704737.0	5489	3.0	-0.6	0.33	177	310	18.2	226 ± 5	a	-	-	-
J053505.62-691923.2	5142	2.5	-0.5	0.4	3298	5011	15.5	222 ± 4	e	5.3	e	Evolved ²⁸ , SC ⁵ , pagb-uncert ²⁵
J053546.56-702810.4	6216	2.5	-0.5	0.03	537	449	16.8	276 ± 5	e	5.4	-	G ⁵ , QSO ⁹
J053551.32-702400.4	5378	3.0	-0.4	0.37	273	480	17.9	223 ± 6	-	-	-	-
J053553.70-704844.7	4500	2.0	-0.3	0.24	660	810	17.2	219 ± 3	a	-	-	-
J053605.89-695802.6	6030	1.5	-1.5	0.03	5569	4499	14.3	316 ± 7	a	-	-	YSO ²⁸ , pagb-disc ²⁵

Table 6: continued.

Name	T_{eff} (K)	$\log g$	[Fe/H]	$E(B-V)$	$(L_{\text{ob}}/L_{\odot})$	$(L_{\text{ph}}/L_{\odot})$	V (mags)	RV (km/s)	$H\alpha$ FWHM	OIII	Previous identifications
J053614.00-695543.8	4712	1.5	-0.5	0.52	1694	2259	16.9	263 ± 2	-	-	Evolved ²⁸ , YSO ⁵
J053618.84-672909.4	4500	2.5	-1.4	0.08	443	418	17.5	324 ± 3	e,a	2.6	-
J053625.85-702834.7	7623	3.5	-0.7	0.05	295	363	17.0	316 ± 6	a	-	-
J053637.40-704709.2	4500	2.5	-1.6	0.04	301	223	18.0	240 ± 7	a	-	-
J053648.05-700722.4 ^b	7578	3.5	-1.6	0.01	144	63	18.8	251 ± 13	e	2.9	QSO ⁹
J053712.04-702131.2	7273	3.5	-0.6	0.02	393	434	16.7	319 ± 8	e,a	4.4	G ⁵ , QSO ⁹
J053720.22-702628.1	4500	1.5	-0.4	0.33	1641	2445	16.3	262 ± 1	a	-	OSARG-AGB ²³
J053802.32-675552.9	4500	1.5	-1.0	0.04	783	827	16.6	308 ± 2	-	-	-
J053808.67-680522.6	5154	3.0	-0.6	0.12	631	591	16.9	272 ± 3	-	-	Evolved ²⁸ , QSO ⁹
J053918.05-704841.8	5519	3.0	-1.0	0.12	181	100	18.8	244 ± 4	e	5.9	QSO ⁹ , red ¹⁰
J053951.46-695703.9	4576	1.5	-0.5	0.64	1031	1321	18.0	265 ± 1	e	4.8	LPV ⁴ , YSO ^{9,28}
J054008.64-704650.7	4500	2.0	-1.4	-0.0	364	295	17.6	298 ± 6	-	-	-
J054044.70-700916.3	7250	4.0	-1.6	0.04	257	101	18.4	200 ± 10	e	5.2	YSO ²⁸
J054128.10-701501.7	4500	1.5	-0.4	0.97	670	2185	18.5	277 ± 2	e	3.4	YSO-hp ²⁸
J054131.78-705614.5	4760	2.0	-0.1	0.35	472	735	17.6	285 ± 2	a	-	LPV ⁴
J054153.85-710903.7	4500	2.0	-0.1	0.34	529	402	18.3	275 ± 3	e	6.1	YSO ^{9,28} , red ¹⁰
J054247.71-695304.2	6076	2.5	-0.6	0.83	689	2383	17.5	273 ± 4	e	5.1	-
J054312.86-683357.1	5221	2.5	-0.3	0.11	167	174	18.2	283 ± 2	a	-	-
J054432.64-704330.7	5103	1.5	-1.9	0.02	3085	1381	15.8	312 ± 6	a	-	CEP ²⁵ , Evolved ²⁸ , RVTau ^{21,25} , pagb-disc ²⁵
J054440.60-713520.5	4965	2.5	-0.0	0.41	777	1293	17.0	228 ± 2	a	-	-
J054442.05-712024.1	5055	2.0	-0.6	0.06	363	412	17.2	257 ± 2	a	-	LPV ^{4,4} , OSARG-RGB ²³
J054535.99-692859.9	4669	3.0	-0.4	0.48	277	397	18.6	309 ± 12	e	5.3	-
J054623.31-704325.8	5287	2.5	-0.3	0.3	401	529	17.6	256 ± 5	a	-	-
J054718.55-705859.7	4500	1.0	-0.8	0.67	1857	3515	17.0	264 ± 1	a	-	Evolved ²⁸ , LPV ⁴ , OSARG-RGB ²³
J054901.96-690322.9	4500	2.0	-0.2	0.53	1955	3159	16.7	286 ± 2	a,e	-	OSARG-RGB ²³
J055219.64-693454.1	4973	2.5	-0.9	0.47	490	922	17.6	329 ± 6	a	-	-
Candidates with [Fe/H] = -0.50											
J045329.79-693211.9	6965	3.5	-0.5	0.04	303	78	18.7	193 ± 23	e	6.6	YSO ²⁸
J045330.21-690316.6	7628	3.0	-0.5	0.13	518	472	17.0	235 ± 21	e	7.6	G/YSO ⁵ , YSO ^{9,28}
J045442.81-654637.9	7626	3.0	-0.5	0.31	284	188	18.5	310 ± 10	a	-	YSO ⁹ , YSO-hp ²⁸
J045625.05-673708.6	9176	3.5	-0.5	0.01	218	214	17.6	256 ± 19	a	-	-
J045746.14-670206.2	7626	3.5	-0.5	0.77	152	599	18.7	273 ± 16	a	-	-
J045750.97-654135.0	8916	3.0	-0.5	0.42	183	282	18.6	267 ± 17	a	-	QSO ⁹
J045804.32-715634.7	4998	2.5	-0.5	0.55	338	639	18.2	214 ± 18	a	-	-
J045835.46-675614.1	7420	3.0	-0.5	0.33	720	1272	16.5	290 ± 7	e,a	2.9	YSO ^{9,28}
J050350.12-655953.9	7625	3.0	-0.5	1.19	1745	15066	16.5	255 ± 10	a	-	-
J050403.92-680048.6	7064	3.0	-0.5	0.37	783	765	17.2	265 ± 20	e	8.6	YSO ^{5,9} , YSO-hp ²⁸
J050422.62-684553.3	7625	3.0	-0.5	1.25	2150	18467	16.5	249 ± 2	a	-	OSARG-RGB ²³ , SG ⁵
J050538.12-693002.2	6784	2.5	-0.5	0.5	315	463	18.1	270 ± 13	a	-	-
J050835.91-711730.7	7625	2.5	-0.5	1.33	4330	4010	18.4	231 ± 24	e	6.0	AGB/post-AGB ⁵ , C-PPNe ²⁷ , LPV ⁴ , YSO ²⁸
J050919.91-682842.1	7643	3.0	-0.5	0.2	1856	776	16.6	288 ± 29	e	5.7	YSO ⁵
J051031.10-713013.0	6059	3.0	-0.5	0.88	203	784	18.9	209 ± 23	a	-	-
J051113.48-681644.6	7628	2.5	-0.5	0.39	2997	13134	15.7	234 ± 6	e	6.9	LPV ⁴
J051543.32-683340.5	7627	3.0	-0.5	0.39	79	162	18.9	228 ± 14	a	-	AGN ¹⁰
J051726.80-692132.0	9948	2.0	-0.5	0.06	8314	13365	13.5	310 ± 21	a,e	-	YSO ⁵
J051812.13-715655.2	7630	3.5	-0.5	0.08	213	156	18.0	230 ± 14	e	5.2	QSO ⁹

Table 6: continued.

Name	T_{eff} (K)	$\log g$	[Fe/H]	$E(B-V)$	$(L_{\text{ob}}/L_{\odot})$	$(L_{\text{ph}}/L_{\odot})$	V (mags)	RV (km/s)	$H\alpha$	FWHM OIII	Previous identifications
J051829.85-711023.3	5752	3.0	-0.5	0.09	131	82	18.9	294 ± 31	a	-	-
J051831.46-685926.3	11000	2.5	-0.5	0.02	5179	6286	14.3	315 ± 8	e	7.6	YSO ^{9,28}
J052000.01-693617.7	7623	2.5	-0.5	0.81	5048	10289	15.7	286 ± 4	e,a	4.1	Evolved ²⁸ , YSO ⁵
J052429.44-693723.7	8876	2.0	-0.5	0.06	7132	9647	13.6	333 ± 9	a	-	pagb-shell ²⁵
J052520.76-705007.5	6742	2.5	-0.5	0.52	3349	6558	15.3	277 ± 23	a	-	C-PPNe ²⁷ , LPV ⁴ , OSARG-RGB ²³ , PN/YSO ⁵ , pagb-shell ²⁵
J052549.58-715627.7	7640	3.5	-0.5	0.26	389	247	18.1	211 ± 11	e	8.8	-
J052700.36-711854.7	7626	3.0	-0.5	0.55	419	615	18.0	270 ± 27	e	8.1	G/YSO ⁵ , QSO ⁹ , YSO-hp ²⁸
J052705.32-713800.2	7372	3.5	-0.5	0.14	448	203	17.9	282 ± 30	e,a	5.1	YSO/G ⁵ , YSO ²⁸
J052731.18-684352.0	7158	3.5	-0.5	0.06	210	196	17.7	299 ± 22	e,a	13.1	-
J052924.07-702724.7	5111	3.0	-0.5	0.04	92	95	18.7	244 ± 28	e	6.7	-
J053020.07-714933.9	7625	2.5	-0.5	0.97	269	1824	18.1	302 ± 38	a	-	YSO ⁵
J053050.58-681210.3	7642	3.0	-0.5	0.05	621	318	17.1	306 ± 13	e	2.7	-
J053244.62-715347.7	9576	3.0	-0.5	0.72	148	816	18.4	234 ± 22	-	-	YSO/G ⁵ , YSO ⁹ , red ¹⁰
J053337.09-711046.1	4578	1.5	-0.5	0.24	764	738	17.3	274 ± 2	a	-	-
J053501.15-695717.6	5113	2.5	-0.5	0.16	271	339	17.7	249 ± 4	e	5.5	YSO ^{9,28}
J053944.35-710350.6	7650	3.5	-0.5	0.04	496	370	17.0	266 ± 12	e	9.5	-
J054000.07-713941.2	7624	3.0	-0.5	1.15	1294	9754	16.9	243 ± 1	e,a	3.7	LPV ⁴ , OSARG-RGB ²³
J054033.54-703240.8	7634	3.0	-0.5	0.33	2064	169	18.7	220 ± 21	e	7.4	YSO ⁵ , PN ^{16,28} , YSO ²⁹
J054037.01-695951.2	7045	3.0	-0.5	0.06	514	351	17.1	340 ± 22	e	5.5	YSO ²⁸
J054503.85-682915.2	7626	3.5	-0.5	1.04	531	1231	18.8	183 ± 30	-	-	G ⁵ , YSO ²⁸
J054540.61-693453.3	7626	3.0	-0.5	1.34	1013	7855	17.7	271 ± 3	e	5.1	YSO ^{9,28}
J054530.64-685610.2	7626	3.0	-0.5	0.46	442	233	18.8	197 ± 33	e	4.6	-
J055133.18-691633.7	7628	3.0	-0.5	0.43	192	286	18.4	347 ± 32	a,e	3.5	G ⁵ , QSO ⁹

Notes: As for Table 4.

The column "Previous identifications" gives the result of a positional cross-matching that was done with the catalogues mentioned in Table 4. Catalogue identifications: OSARG-AGB = OGLE small amplitude red giant - AGB star, OSARG-RGB = OGLE small amplitude red giant - RGB star, LPV = long period variable, YSO = young stellar object, YSO-hp = high probability YSO candidate, pagb-disc = post-AGB with disc-type SED, pagb-shell = post-AGB with shell-type SED, pagb-uncer = post-AGB with uncertain-type SED, G = background galaxy, Evolved = evolved object, CEP = Cepheid variable, RVT = RV-Tauri, C-PPNe = carbon-rich proto-planetary nebula, Be = Be star, O-PAGB = oxygen-rich post-AGB, C-PAGB = carbon-rich post-AGB, PN = planetary nebula, SRV-AGB = semi-regular variable AGB star, SRV-RGB = semi-regular variable RGB star, QSO = quasi-stellar object, red = stars with red spectra, AGN = active galactic nuclei, C = C-star. See catalogued references for full details of the individual object identification. The superscript 'b' in the first column indicates that the T_{eff} value used to estimate $E(B-V)$ is increased by 250K (see Subsection 6.2 for further details).
[†]Based on the spectra of J050830.51-692237.4, it is likely a YSO candidate with a C-star in the line-of-sight (see Section 9).

For each of the spectroscopically verified post-AGB, post-RGB and YSO candidates, we performed a positional cross-matching with the most relevant previous studies. The results of the positional cross-matching are listed in the last column of Tables 4, 5 and 6 for the post-AGB, post-RGB and YSO candidates, respectively. In Table 4 (see footnote) we list all the previous studies used for the positional cross-matching. We find that, in many cases, the positional cross-matching gives a similar evolutionary nature for the objects. However, in some cases, mostly when the positional cross-matching is performed with studies that use a purely photometric classification (e.g., Whitney et al. 2008), we find that the evolutionary nature of the object was misclassified. This goes to show that spectroscopic characterisation of objects is crucial to confirm their evolutionary nature. The positional cross-matching also helps to test our $\log g$ criterion for the separation of post-AGB/post-RGB and YSO objects. We find that for majority of the cases, the nature of the objects the nature of the object from our spectroscopic analysis matched well with other studies that are based either on high-resolution optical spectroscopic studies (e.g., van Aarle et al. 2013) or studies using SST spectra (e.g., Woods et al. 2011).

However, in some cases there exists an inconsistency in the nature of the object when compared to studies using SST spectra. For instance, Woods et al. (2011) have classified J051228.19-690755.8 as a C-rich PAGB star. Volk et al. (2011) classify this object as a C-rich proto-planetary nebula. Furthermore, they estimate the luminosity of the object to be $4200 \pm 550 L_{\odot}$. In our study, J051228.19-690755.8 has been classified as a post-RGB star based on its $\log g$ value and its photospheric luminosity ($L_{\text{ph}} = 1164 L_{\odot}$) (see Table 5). The observed luminosity of this object is $L_{\text{ob}} = 2932 L_{\odot}$. This object could be a post-AGB star if its estimated reddening value is too low. A good high-resolution spectrum is required to obtain a more accurate estimate of the reddening.

The relevance of our $\log g$ criterion can be illustrated by considering one of the objects in our sample: J053253.51-695915.1. This object is one of the four objects considered in a detailed chemical abundance study of candidate *s*-process enriched post-AGB objects, using high-resolution UVES spectra (van Aarle et al. 2013). van Aarle et al. (2013) find that though J053253.51-695915.1 shows a mild *s*-process enrichment, there is an anti-correlation between the strength of the neutron irradiation and the efficiency of the third dredge-up. However, observationally, post-AGB stars have always shown a strong correlation between the two parameters (Van Winckel & Reyniers 2000; Reyniers et al. 2004). van Aarle et al. (2013) attribute this anti-correlation to the possible extrinsic nature of J053253.51-695915.1 i.e. it obtained its *s*-process enhancement by mass transfer from an AGB star in a binary system. However, in our study, based on our $\log g$ criterion, we classify this object as a YSO candidate (see Table 6), indicating that the mild *s*-process enhancement comes from the initial composition of the LMC (Van der Swaelmen et al. 2013).

The detailed spectroscopic analysis in our study is performed using low-resolution spectra ($R \approx 1300$). Since the classification of post-AGBs/post-RGBs from the YSOs is based on the estimated $\log g$ value, it is possible that some of the objects have been misclassified, espe-

cially when the signal-to-noise ratio of the spectra are low (either due to faint optical fluxes or poor observing conditions). For instance, Volk et al. (2011) classify J051845.23-700534.5 ($V = 17.5$ mags), J050835.91-711730.7 ($V = 18.4$ mags) and J052520.76-705007.5 ($V = 15.3$ mags) as C-rich proto-planetary nebulae. J051845.23-700534.5 and J050835.91-711730.7 show the $21\mu\text{m}$ feature, that is especially prominent in the spectra of some carbon-rich proto-planetary nebulae and also the $30\mu\text{m}$ feature which which is commonly observed in the spectra of carbon stars and generally attributed to MgS (see Volk et al. 2011, and references therein). J052520.76-705007.5 shows the $21\mu\text{m}$ feature and only a weak trace of the $30\mu\text{m}$ feature. In our study, we classify all the three objects as YSOs (see Table 6) based on their spectroscopically derived $\log g$ values. On visually inspecting the low-resolution spectra of these 3 objects, we find that the spectra of J051845.23-700534.5 and J050835.91-711730.7 are rather noisy and of low signal (which is likely due to their faint optical magnitudes). For J052520.76-705007.57, the spectroscopically determined T_{eff} for this object is $\approx 7000\text{K}$. The spectrum of this star does not contain CaT absorption lines but instead contains the Paschen lines. For such objects without the CaT absorption lines and with T_{eff} values in the range of $6000\text{K} - 8000\text{K}$, the Balmer lines in the wavelength region of $3750\text{\AA} - 3950\text{\AA}$ are used to determine the $\log g$ (see Paper I for full details). For J052520.76-705007.5, this region of the spectrum is rather noisy. Therefore it is likely that the spectroscopically estimated $\log g$ values for these three objects are uncertain beyond the estimated error of $0.5 - 1.0$ resulting in a possible misclassification of their nature. Note that the spectral fitting for these three objects (as well as all the other objects in our study) can be found in the online supporting information

The importance of a detailed spectroscopic analysis such as that presented in this study can be further illustrated by comparing the results of our spectral analysis to the sample of 70 post-AGB candidates from van Aarle et al. (2011) that were identified on the basis of a visual spectral-type classification only. Of the 2102 objects in our study for which we obtained optical spectra, 37 were in common with the 70 objects classified as post-AGB candidates by van Aarle et al. (2011). Table 7 lists these 37 objects along with the nature of the object as classified in our study. We find that, though some of the object classifications from the two studies match, majority of the 37 objects are not necessarily post-AGB candidates, as classified by van Aarle et al. (2011). They cover a wide range of object classes such as post-RGBs, YSOs, luminous supergiants and likely main-sequence stars. Therefore, our systematic spectral analysis provides a more detailed classification of the nature of the objects.

7.1 The newly discovered post-RGB objects

The spectroscopic analysis along with the determination of the photospheric luminosities (L_{ph}) have revealed a new population of evolved, dusty "post-RGB" objects with $L_{\text{ph}} \lesssim 2500 L_{\odot}$. This class of objects was discovered in our SMC survey (see Paper I) where 41 new dusty post-RGB objects were presented. The present study has confirmed the existence of dusty post-RGB stars, by revealing 119 such

Table 7. The nature of the 37 objects that were common to our study and that of van Aarle et al. (2011). In van Aarle et al. (2011), these 37 objects were classified as post-AGB stars based on a visual spectral-type classification.

Object	Nature of the object based on our study
J045243.16-704737.3	post-RGB
J045444.13-701916.1	Reject
J045543.20-675110.1	C star
J045615.77-682042.3	M star
J045623.21-692749.0	post-AGB
J045655.23-682732.9	post-AGB
J050304.95-684024.7	post-RGB
J050431.84-691741.4	Main-sequence star
J050632.10-714229.8	post-AGB
J050718.33-690742.9	YSO
J050733.83-692119.9	C star
J050830.51-692237.4	YSO
J051418.09-691234.9	post-AGB
J051450.04-692735.3	YSO
J051453.10-691723.5	post-RGB
J051624.89-690000.8	YSO
J051845.47-690321.8	YSO
J051848.84-700247.0	post-AGB
J051917.29-693147.3	YSO
J052340.49-680528.2	Luminous object
J052429.44-693723.7	YSO
J052519.48-705410.0	post-AGB
J052520.76-705007.5	YSO
J052722.11-694710.1	Luminous object
J052836.59-685829.9	M star
J053011.67-710559.7	Luminous object
J053250.69-713925.8	post-AGB
J053253.51-695915.1	YSO
J053416.45-695740.4	M star
J053444.17-673750.1	QSO
J053505.62-691923.2	YSO
J053605.89-695802.6	YSO
J054312.86-683357.1	YSO
J055122.52-695351.4	post-AGB

candidates in the LMC. So far, in the Galaxy, these objects have not been identified, owing to the unknown distances and hence unknown luminosities. However, it is likely that some of the supposed Galactic post-AGB objects are indeed post-RGB objects.

The post-RGB objects have stellar parameters (T_{eff} , $\log g$, [Fe/H]), IR colours and SED types similar to those of post-AGB stars. However, their luminosities (and hence masses and radii) are much lower than that expected for post-AGB stars. Furthermore, we expect that they should be in binary systems, since single-star mass loss that occurs during the RGB phase is insufficient to remove the H-rich envelope and produce a dusty post-RGB star (e.g. Vassiliadis & Wood 1993). Therefore, the only way large amounts of mass loss followed by evolution off the RGB can occur is via binary interaction (e.g., Han et al. 1995; Heber 2009).

To confirm the evolutionary nature of these objects and establish evolutionary links to their possible precursors and progeny, in the near-future we intend to carry out a radial velocity monitoring program to verify their likely binary nature. Furthermore, we also intend to pursue a chemical abundance study to investigate their chemical patterns.

8 CLASSIFICATION OF SPECTRAL ENERGY DISTRIBUTIONS

Post-AGB/post-RGB and YSO candidates consist of two components: the central star and the circumstellar environment. SED analysis of the Galactic post-AGB stars revealed two highly distinct populations: the shell-sources with double peaked SEDs (probably arising from single stars, Van Winckel 2003), and disc-sources with a near-IR excess indicative of hot dust and circumstellar discs probably arising from binary stars (de Ruyter et al. 2006; Van Winckel 2007; Gielen et al. 2009; Van Winckel et al. 2009; Dermine et al. 2013). The post-AGB/post-RGB stars in the SMC also showed these two populations. We performed a preliminary SED analyses to classify the LMC post-AGB and post-RGB candidates into shell- and disc-sources, based on the visual inspection of the position of the peak of their dust excess. In shell-sources, the dust emission peaks at wavelengths greater than $10\mu\text{m}$ (as shown by radiative transfer models of the well known expanding shell source HD161796, where the peak of the dust SED is at around $30\mu\text{m}$, see Min et al. 2013, for details). On the other hand, for disc-sources the peak of the dust SED lies around $10\mu\text{m}$ and in some cases even bluer (de Ruyter et al. 2006; Gielen et al. 2011a). Figure 9 and Figure 10 show a few examples of post-AGB/post-RGB candidates that we classified as shell-sources and disc-sources, respectively. We note that for a group of objects, we were unable to classify them based on their SEDs and we call these objects ‘uncertain-sources’. Figure 11 shows a few examples of SEDs of post-AGB/post-RGB candidates that we classify as uncertain. Of the 35 post-AGB objects, we find a group of 10 shell-sources, 23 disc-sources and 2 are of uncertain SED type. Similarly, of the 119 post-RGB objects, we find a group of 23 shell-sources, 56 disc-sources and 40 uncertain.

To find a more quantitative method for classifying disc- and shell-sources, we explore the position of the sources in the $[8] - [24]$ vs $[3.6] - [4.5]$ colour–colour plot used previously. We note that a large $[3.6] - [4.5]$ indicates the presence of a near-IR excess due to hot dust surrounding the central star. This is indicative of a stable dust structure close to the central star, as these objects have photospheres too hot to be in a dust producing phase. A large $[8] - [24]$ colour indicates the presence of colder dust in the system. In Figure 12, we show the post-AGB and post-RGB candidates on a $[8] - [24]$ vs $[3.6] - [4.5]$ colour–colour plot indicating their visual SED-based classification as discs, shells or uncertain sources. We find that the majority of shell-sources show a $[8] - [24] > 4.0$. These shell-sources show only a mild $[3.6] - [4.5]$ excess with $[3.6] - [4.5] < 0.5$. Most disc-sources have a clear near-IR excess with $[3.5] - [4.5] > 0.5$. Some disc-sources, however, have $[3.6] - [4.5] < 0.5$ but in combination with a $[8.0] - [24] < 3.0$, indicating that hot dust dominates their SEDs. Finally the uncertain-sources are found to occupy the region between the disc- and shell-sources. This region is characterised by $3.0 < [8] - [24] < 4.0$ and $[3.6] - [4.5] < 0.5$.

We find that approximately half the post-RGB sample are classified as disc-sources while the remainder do not show disc-type SEDs. This is inconsistent with the suggested formation channel in which the RGB evolution of *all* post-RGB stars is terminated prematurely by a binary interac-

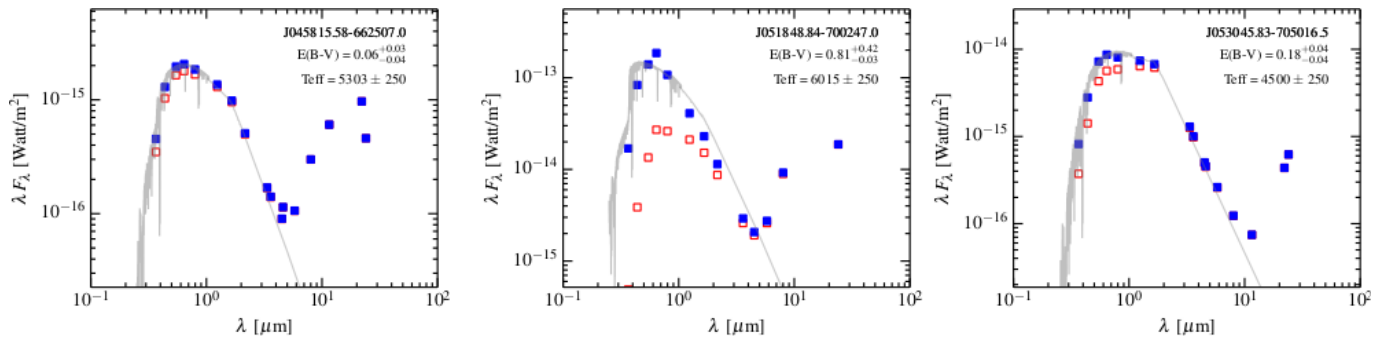


Figure 9. Example SEDs of the post-AGB/post-RGB candidates classified as shell sources. The red open squares represent the original broadband photometry. The blue filled squares represent the dereddened broadband photometry. Up to a wavelength of 10500Å, we over-plot (grey solid-line) the flux-calibrated Munari synthetic spectrum which is estimated to have the best-fit to the observed spectra (see Section 6.1). From 10500Å onwards we over-plot the low-resolution flux distribution from the corresponding appropriate ATLAS9 atmospheric model (Castelli & Kurucz 2004). The SED plots also show the name of the individual object, the estimated $E(B-V)$ value with error bars (see Section 6.2) and the estimated T_{eff} value.

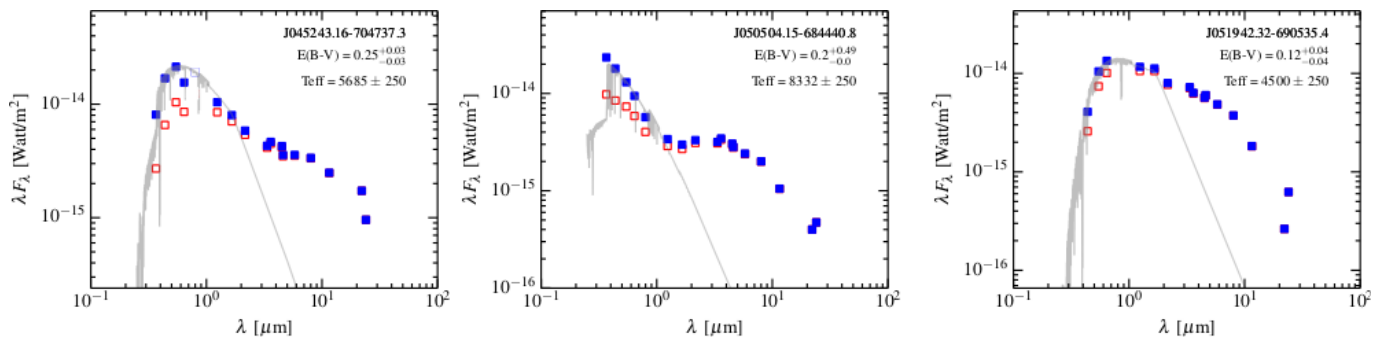


Figure 10. Example SEDs of the post-AGB/post-RGB candidates classified as disc sources. The symbols used in the plots are same as that mentioned in Figure 9.

tion which also results in the creation of a dusty disc. In fact, we find that 23 objects are classified as shell-sources within our classification scheme. Since binary interaction is, to our knowledge, the only mechanism that can prematurely terminate the RGB evolution, we think that the objects with shell-type SEDs in our study are not exclusively single stars but may also be stars in binary systems with likely evolved dusty disc components that peak at longer wavelengths. Furthermore, we find that the majority of the sources classified as ‘uncertain’, are post-RGB stars and therefore we expect these objects to also have dusty discs. This also shows that our SED based classification is a rather approximate classification and does not translate directly to the single or binary nature of these objects, especially since their SEDs are limited to $24\mu\text{m}$ in most cases. To be able to clearly differentiate between shell-type and disc-type SEDs, we would need SEDs which extend to longer wavelengths. For each of the post-AGB and post-RGB objects, their SED classifications (“disc”, “shell” or “uncertain”) are given in the SED column of Tables 4 and 5.

In the right panel of Figure 12 we also plot the YSO candidates (as blue filled circles) though the classification scheme for YSOs are different compared to that of post-AGB/post-RGB candidates. A SED based YSO classification is beyond the scope of this study. We note that the SEDs of the post-AGB, post-RGB and YSO candidates can

be found in Appendix C and are also available as online supporting information.

9 FEATURES IN THE STELLAR SPECTRA

Spectra can provide a plethora of information about the nature of an object. To further investigate the post-AGB, post-RGB and YSO candidates, we inspected their spectra individually.

We find in some cases prominent emission lines in the Balmer sequence (especially the $H\alpha$ line at 6562.8\AA), forbidden lines of oxygen ([OIII]), sulphur ([SII]), nitrogen ([NII]), the HeI lines, the CaT line or the Paschen lines. This indicates either that the star is of an early spectral type capable of exciting circumstellar gas or in those cases when the line profiles are narrow then there is un-associated ISM nebulosity in line-of-sight to the candidate.

The most prominent diagnostic is certainly the $H\alpha$ line. We find that in many of our post-AGB and post-RGB stars, the line profile is dominated by a strong emission component along with a weaker absorption component, similar to that seen in the post-AGB stars studied by van de Steene et al. (2000). Even with the low spectral resolution and low signal-to-noise ratio of our spectra, we can resolve the $H\alpha$ emission line profile which indicates the presence of strong

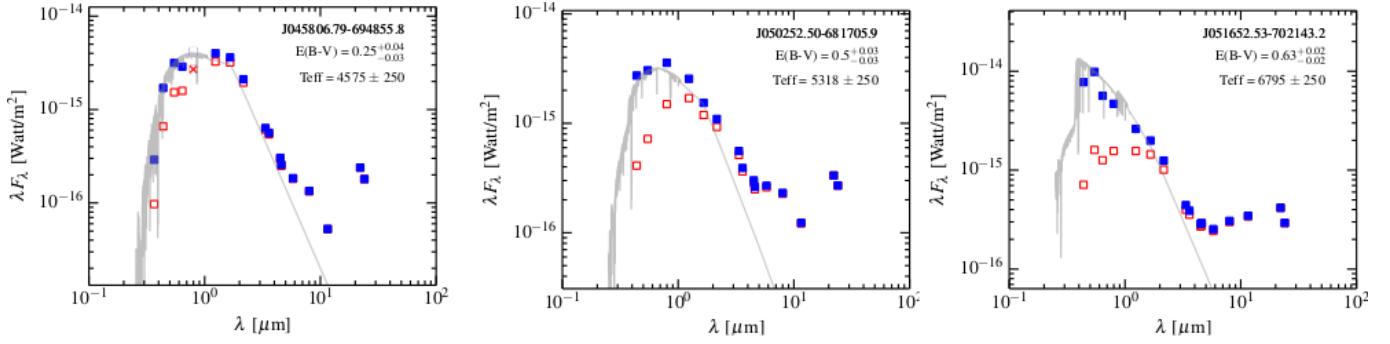


Figure 11. Example SEDs of the post-AGB/post-RGB candidates that are classified as ‘uncertain’. The symbols used in the plots are same as that mentioned in Figure 9.

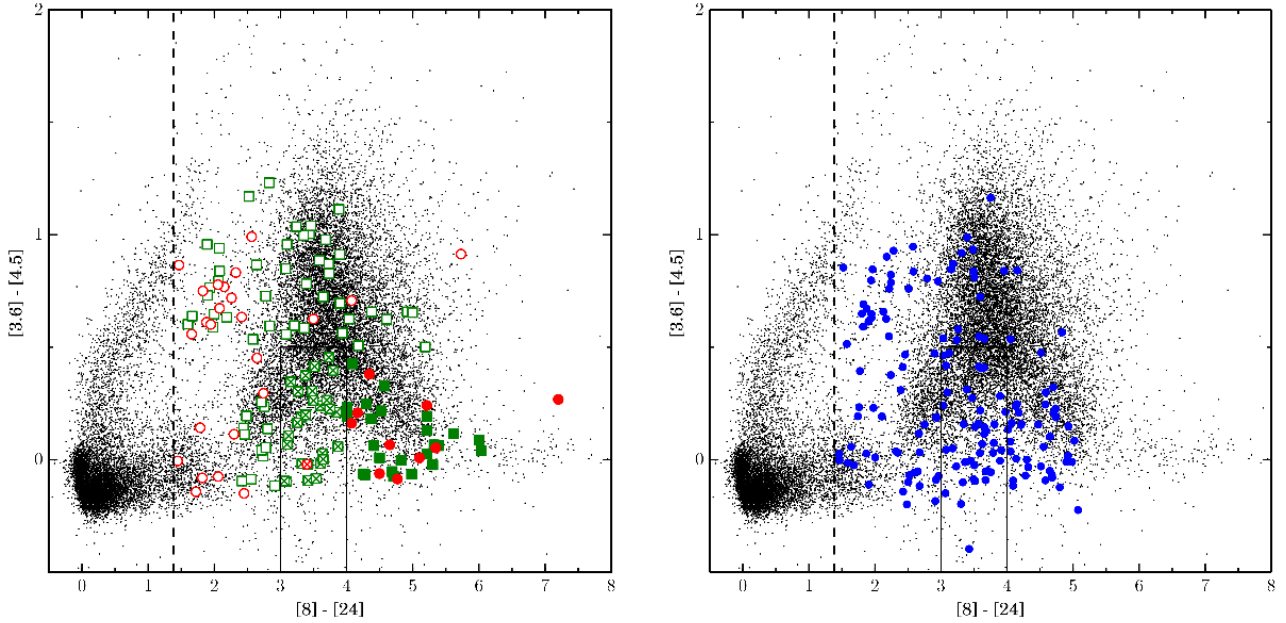


Figure 12. Left panel: Same as Figure 1, but indicating the visual SED-based classification as disc-, shell- or uncertain-sources for the post-AGB (red circles) and post-RGB candidates (green squares). Disc sources are represented as open symbols, shells as filled symbols and uncertain sources with enclosed-crosses. The region $3.0 < [8] - [24] < 4.0$ and $[3.6] - [4.5] < 0.5$ is marked with black solid lines and is where the uncertain-sources lie. Right panel: Same as Figure 1 but for the YSO candidates, represented as blue filled circles. The uncertain-sources region is transferred from the left panel to the right panel for comparison purposes only.

winds. Van de Steene et al. (2000) explain that the emission component originates close to the central star and the absorption component originates from the fast wind itself or in the region where the fast wind sweeps up the slow wind. In some rare cases we find that the $H\alpha$ line profile is dominated by an absorption component, along with a weaker emission component which is likely to be indicative of ongoing mass-loss in these objects. Furthermore, in some of the objects with a $H\alpha$ emission line profile, an absorption core is also detected and vice-versa. The $H\alpha$ line profile of the 162 YSO candidates also show similar trends to that of the post-AGB/post-RGB objects explained above. Natta et al. (2002) and Jayawardhana et al. (2002) show that the $H\alpha$ emission and forbidden line emission in YSOs indicate disc accretion.

In Tables 4, 5 and 6, we have summarised the line

profile of the $H\alpha$ line as well as the forbidden oxygen [OIII] line of the final sample of post-AGB, post-RGB and YSO candidates, respectively. The tables also list the full width at half maximum of the $H\alpha$ for an emission line profile, as an indication of whether the line is spectrally resolved or not. For broad lines, the FWHM is a good proxy of the H-alpha gas outflow velocity. Considering the resolution of the spectrograph ($R \approx 1300$), the outflow velocity must be larger than $\sim 115 \text{ km s}^{-1}$ (FWHM of 5 \AA) to be resolved. We find that for the majority of the objects, the $H\alpha$ line is resolved, indicating a large outflow velocity.

Four of the post-RGB candidates (J050504.15-684440.8, J052245.11-713610.2, J052834.16-715558.1 and J053130.65-714448.2), show FeII emission line features in their spectra. These features are characteristic of B[e] stars (see Section 4).

A significant element with respect to post-AGB stars is barium. The presence of enhanced Ba lines in the stellar spectrum indicates a *s*-process enriched post-AGB object. For low- to intermediate-mass stars, a significant amount of *s*-process nucleosynthesis takes place prior to the post-AGB phases of stellar evolution. Therefore we expect to detect the presence of *s*-process elements for post-third dredge-up objects.

On visually inspecting the spectra of the post-AGB candidates, we were unable to identify barium in the majority of cases. This could be due to the low-resolution of our spectra. However, for strongly *s*-process enriched stars, we were able to detect the presence of the strong BaII line at 4554.03Å. We found that 6 out of 35 stars (J050632.10-714229.8, J051906.86-694153.9, J052147.95-700957.0, J052220.98-692001.5, J052243.99-693828.0, J052604.53-685737.6) show the presence of the BaII line at 4554.03Å. J050632.10-714229.8 and J053250.69-713925.8 has been previously identified, from abundance studies with high resolution spectra, as *s*-process enriched post-AGB stars by van Aarle et al. (2013). Two of the post-RGB stars (J051453.10-691723.5 and J054034.77-683228.2) also the presence of the BaII line at 4554.03Å. J051453.10-691723.5 has $L_{\text{ob}} = 2616 L_{\odot}$ and $L_{\text{ph}} = 2171 L_{\odot}$, close to the post-AGB-post-RGB dividing line of $2500 L_{\odot}$ so this star is probably a genuine post-AGB star. On the other hand, J054034.77-683228.2 has $L_{\text{ob}} = 845 L_{\odot}$ and $L_{\text{ph}} = 906 L_{\odot}$ so it seems to be an unambiguous post-RGB star. In this case, since post-RGB stars have not yet gone through the AGB phase, it is likely that the object is extrinsically enriched by binary mass transfer putting in the category of Ba-stars.

Five of the YSO candidates (J050252.54-674848.6, J051845.47-690321.8, J053030.10-675018.0, J053153.96-673845.7, J053625.85-702834.7) show the presence of the BaII line at 4554.03Å, indicating *s*-process enrichment. This could imply that either these objects are post-AGB objects that have been misclassified YSOs or that the strong detection at 4554.03Ås is not real.

Another element of interest is lithium, which can be detected by the presence of the LiI line at 6708 Å. Lithium is abundant in the parent molecular cloud but it is destroyed in the stellar interior at relatively low temperatures ($\sim 2 \times 10^6$ K). If these interior temperatures are reached when the star is convective, Li will be depleted at the stellar surface during the pre-main sequence phase. During the evolution beyond the main sequence, lithium is further decreased owing to the first and second-dredge up processes that occur during the red-giant phase of evolution and the early-AGB phase of evolution (Karakas & Lattanzio 2003). However, in massive stars ($> 4 M_{\odot}$) during the thermally pulsing AGB phase, lithium can be created by hot bottom burning (Boothroyd et al. 1995; Lattanzio et al. 1996). We searched for the presence of lithium in the stellar photospheres of both the post-AGB/RGB and YSO candidates by visually inspecting the spectra. We could not detect the LiI (6708 Å) line in absorption in any of the post-AGB and post-RGB candidates. This is as expected since current evolutionary models for these initial mass ranges (calculated based on their luminosities) do not predict an enhanced Li abundance.

We detected the LiI (6708 Å) line in absorption in for 11 out of 162 YSO candidates (J044535.72-685840.4,

J044920.32-690900.0, J045009.84-701320.9, J045145.31-692837.1, J045424.37-685240.6, J050422.62-684555.3, J052141.52-710909.2, J053050.58-681210.3, J053337.09-711046.1, J053614.00-695543.8, J054153.85-710903.7) indicating that these latter objects are probably early stage YSOs or massive YSOs. We note again that the low-resolution of the spectra could possibly affect the number of identifications.

Figure 13 shows examples of the different H α line profile that the stars in our sample display. Also shown in Figure 13 are selected parts of the continuum-normalised spectrum for a few sample objects that show the forbidden [OIII] emission line (at 5001Å), the region with the multiplet 42 of FeII (at $\approx 4924\text{Å}$, 5018Å, and 5169Å), the barium line (at $\approx 4554\text{Å}$) as well as the Li absorption line (at $\approx 6708\text{Å}$).

A peculiar object in our sample is J050830.51-692237.4 (see Table 6), which has been classified as a YSO candidate based on our $\log g$ criterion. On analysing the spectrum of this object, we find that it shows a hot component that corresponds to an A-type star as well as a cooler component with molecular bands of carbon, corresponding to a C-star. Based on the radial velocity estimates of the two components of the spectra, we find that both the components have LMC velocities. The hot component has a heliocentric radial velocity of $\approx 220 \text{ km s}^{-1}$ while the cool component shows $\approx 290 \text{ km s}^{-1}$. The spectral features and the estimated radial velocities of the two components were also confirmed using UVES spectrum of this object that was obtained as a part of our high-resolution follow-up studies. Woods et al. (2011) have analysed the SST IRS spectra of this object and have found that the circumstellar environment of this object is clearly O-rich but with very large crystallinity, which indicates that the dust is in the form of a disc and therefore associated with an object in a binary system (with the C-star as it's companion) or a YSO. The former scenario is very unlikely as it would require a binary system with a post-AGB star and an AGB star or a luminous main-sequence star and a AGB star, which is rather uncommon. Furthermore, from the STP, the estimated $\log g$ value points to a YSO evolutionary nature for J050830.51-692237.4. Therefore, it is likely that this object is YSO with a O-rich disc and in the line-of-sight of the object is a non-related C-star.

10 EVOLUTIONARY STAGES OF THE POST-AGB, POST-RGB AND YSO CANDIDATES

To understand the evolutionary stage of the post-AGB, post-RGB and YSO candidates, we show their positions in the HR diagram in Figure 14. The left panel shows the post-AGB and post-RGB population. We note that the T_{eff} values are those derived from the spectral fitting and the luminosities plotted are the photospheric luminosities (L_{ph}).

Each plot shows the main sequence as a cyan cross-hatched region. Evolutionary tracks starting from the main sequence and continuing up to the AGB-tip according to the tracks of Bertelli et al. (2008, 2009) are shown as black solid lines. Note that these tracks use a synthetic AGB calculation adopting unusual mass loss rates, and almost certainly terminate at too low a luminosity. The plots also show the PISA pre-main sequence (PMS) evolutionary tracks (black

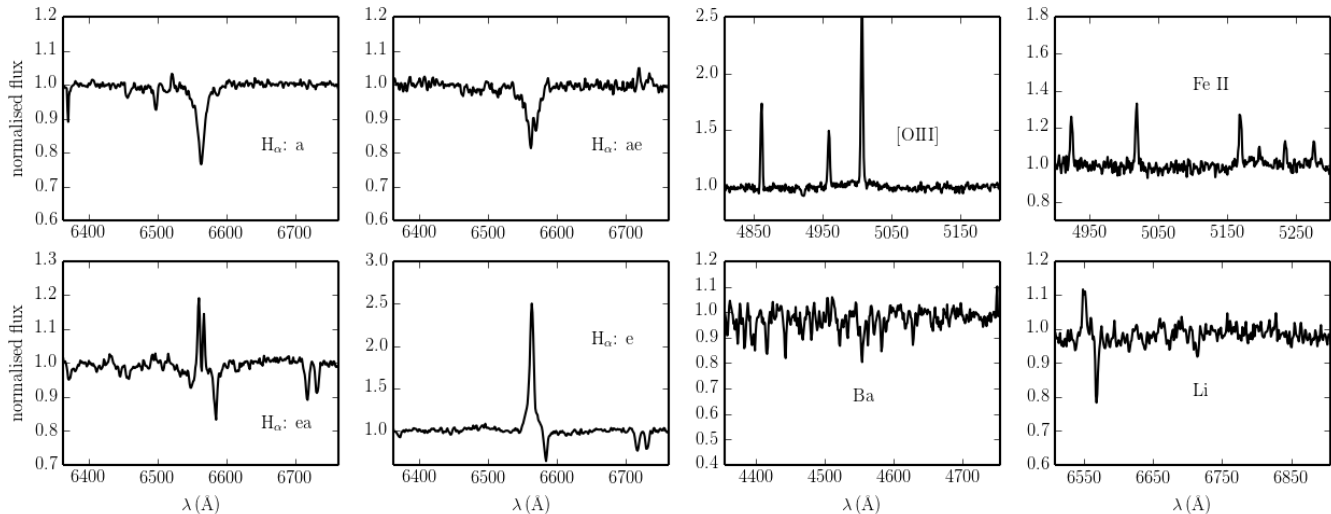


Figure 13. A small part of the continuum-normalised spectrum for a few sample stars that show the different H α line profiles, the forbidden [OIII] emission line, the region with FeII emission lines, the barium line (4554.03Å) and the Li absorption line (6708 Å). The spectral feature shown is labelled in each of the panels (see text for further details). In the case of the H α line, the nature of the line profile is also mentioned. See Tables 4, 5, and 6, for more details.

dotted lines: Tognelli et al. 2011) up to the maximum computed mass of $7 M_{\odot}$. A metallicity $Z = 0.004$ was selected for both sets of evolutionary tracks. The masses of the evolutionary tracks are marked on the plots with the PMS and main-sequence masses marked on the left side of the plots and RGB-tip masses marked on the right side of the plots. The positions of the RGB and AGB are also marked.

In the figure showing the post-AGB and post-RGB candidates, post-AGB and post-RGB evolutionary tracks are shown schematically (black dashed arrows). The masses for the post-AGB evolutionary tracks are from Vassiliadis & Wood (1994) for $Z = 0.004$. The post-RGB evolutionary track masses are estimated from the RGB luminosity-core mass relation of the Bertelli et al. (2008) models with $Z = 0.004$. In Section 7, we estimate the masses of the post-AGB and post-RGB candidates. The post-AGB candidates (with $L_{\text{phot}} \gtrsim 2500 L_{\odot}$) have masses of $\sim 0.45 - 0.8 M_{\odot}$ and the post-RGB candidates (with $(L_{\text{phot}} \approx 100 - 2500 L_{\odot})$) have masses of $\sim 0.28 - 0.45 M_{\odot}$.

In the HR diagram of the post-AGB/post-RGB candidates, the blue vertical lines shows the empirical OGLE instability strip for the Population II Cepheids presented in (Soszyński et al. 2008), since post-AGB/post-RGB evolutionary tracks cross the Population II Cepheids instability strip. In the HR diagram showing the YSO candidates, the green vertical lines on this plot denotes the Cepheid instability strip from Chiosi et al. (1993). Also shown in the HR diagram showing the YSO candidates, is the birthline (thick black dashed line in right panel of Figure 14), which may be considered as the dividing line between the obscured protostellar and the observable pre-main sequence stage of stellar evolution. The location of the birthline depends highly on the mass accretion rate, with higher accretion rates shifting the line to the right. A mass accretion rate of $10^{-5} M_{\odot}/\text{yr}$ (used for the birthline in right panel of Figure 14) represents the typical value for stars in the mass range from few

tenths of a solar mass to about $10 M_{\odot}$ (Stahler 1983; Palla & Stahler 1993).

The YSOs, with masses in the range of $\sim 3 - 10 M_{\odot}$ (see Section 7 and Figure 14), are rather luminous ($L_{\text{phot}} > 200 L_{\odot}$) and lie on the cool side of the usually adopted birthline in the HR-diagram. We also find that the majority of YSOs lie to the right of the birthline so they should not be visibly detectable. A similar trend was observed for the YSOs identified in the SMC (see Paper I), where we concluded that the discrepancy may be due to the assumption of symmetric and spherical dust shells in the birth line modelling (with asymmetries, it may be possible to see the central star through a region of low extinction), or too high an assumed accretion rate since the birthline depends on the mass-accretion rates (Palla & Stahler 1993). A low mass accretion rate could move the birthline to lower values of T_{eff} so that our stars could become visible. A group of massive pre-main sequence stars similar to the Galactic Herbig AeBe stars was found in the LMC by Lamers et al. (1999) and these are also located above the traditional birth line used for the Galactic sources. Lamers et al. (1999) suggested that this could be due to either a shorter accretion timescale for Galactic Herbig AeBe stars due to lower metallicity in the LMC, or a lower dust-to-gas ratio in the LMC, again owing to the lower metallicity. Therefore for the LMC, a higher birth line for YSOs could be expected in the HR diagram.

11 COMPLETENESS OF THE SURVEY

This study is aimed at identifying optically visible post-AGB and RGB candidates in the LMC. However, the survey obviously has its limitations and does not catalogue all the post-AGB and post-RGB stars. In this section we have listed the limitations that govern this survey and also provide the extent of the completeness of our survey.

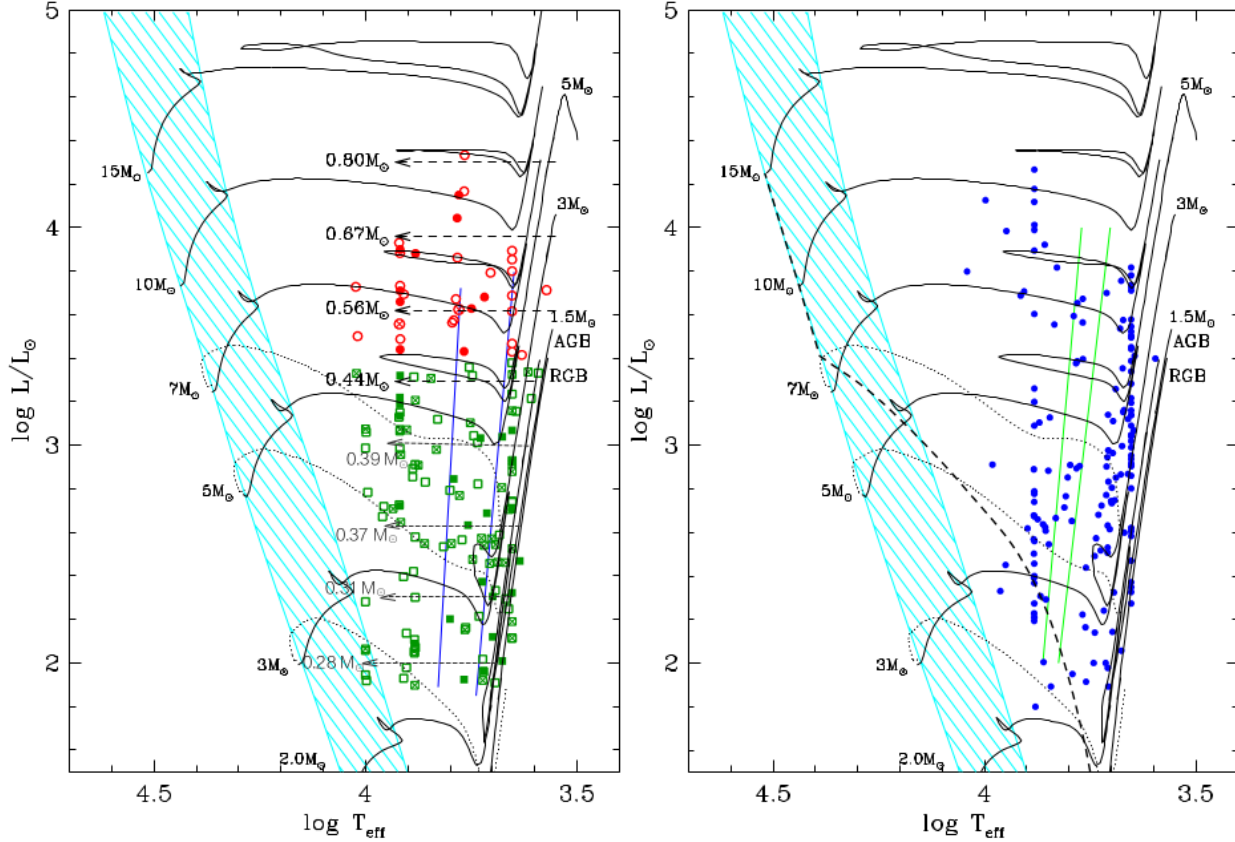


Figure 14. The HR diagram for the sample of the post-AGB and post-RGB candidates (left panel) and YSO candidates (right panel). In the left panel, the red circles represent the post-AGB candidates and the green squares represent the post-RGB candidates. The open symbols represent disc sources and the filled symbols represent the shell sources. The enclosed-crosses represent those post-AGB/post-RGB candidates for which the nature of the SED is uncertain. In the right panel, the blue filled circles represent the YSO candidates. Each plot shows the main sequence as a cyan cross-hatched region. In both the plots the black solid lines represent evolutionary tracks starting from the main-sequence and the black dotted lines represent pre-main sequence evolutionary tracks. The black dashed arrows on the HR diagram for the post-AGB/post-RGB candidates schematically represents the post-AGB/post-RGB evolutionary tracks, each labelled by the current stellar mass. Also shown on this plot is the empirical OGLE instability strip for the Population II Cepheids represented with blue vertical lines. In the right panel, the thick black dashed line in right panel is the birth-line and the green vertical lines represent the Cepheid instability strip. See text for further details.

To obtain a complete sample of post-AGB/post-RGB candidates in the LMC, we used the selection criteria of van Aarle et al. (2011) and these selection criteria restrict our search to post-AGB/post-RGB candidates with an excess at $24\mu\text{m}$. Older post-AGB/post-RGB stars with expanding shells for which the excess is undetectable at $24\mu\text{m}$ will not be selected. For instance, the LMC counterparts of the hot Galactic post-AGB stars studied by Gauba & Parthasarathy (2004) will not be selected since their $24\mu\text{m}$ fluxes would be below the detection threshold. Furthermore, we require that all the selected candidates have $V < 20$ mags, which only selects those post-AGB/post-RGB stars that are optically visible, therefore omitting those that are faint or heavily dust enshrouded.

Based on the mid-IR selection criteria, we started with a sample of 8628 objects, out of which 1517 objects were given

a priority 1, 6823 were given a priority 2 and 286 were given a priority 3. We note that the priorities were assigned based on the selection criteria used and the likelihood of finding post-AGB/post-RGB candidates with that selection criteria (see Section 2). In Table 8 we give a breakdown of the number of objects with respect to their assigned priorities as the analysis has proceeded. We performed a low-resolution optical survey that covered a large part of LMC, as shown in Figure 2. From the initial selected sample of 8628 objects, we obtained spectra of 2102 objects. Excluding the 556 objects that had a poor-quality spectrum with low signal (< 200 counts), we were left with a sample of 1546 unique spectra. Taking into consideration the candidates for which we did not obtain spectra and the objects that we rejected from the spectral analysis due to poor quality of their spectrum, we estimate the completeness of the survey (defined

Table 8. A breakdown of the number of objects with respect to their assigned priorities, as analysis has proceeded.

Stage	Total objects	Priority 1 objects	Priority 2 objects	Priority 3 objects
Initial photometric selection for the whole LMC	8628	1517	6823	286
Objects with optical spectra	2102	883	1170	49
Objects rejected due to poor spectra	556	102	449	5
Objects retained with good optical spectra	1546	781	721	44
Objects classified as M stars	382	333	10	39
Objects classified as C stars	55	51	3	1
Objects classified as PN	123	56	67	0
Objects classified as red-shifted galaxies	290	26	264	0
Objects classified as QSOs	39	2	37	0
Objects with TiO in emission	5	5	0	0
Objects with strong emission lines and an UV continuum	69	35	32	2
Sample of probable post-AGB/post-RGB and YSO candidates with confirmed LMC membership	581	271	308	2
for which we carry out detailed spectral analysis				
Objects without B, V magnitudes	85	12	73	0
Objects with $T_{\text{eff}} > 12000$ K (likely hot main-sequence objects)	68	34	34	0
Objects with $L_{\text{ph}} > 35000 L_{\odot}$ (likely luminous super-giants)	112	105	5	2
Final number of post-AGB candidates	35	34	1	0
Final number of post-RGB candidates	119	34	85	0
Final number of YSO candidates	162	52	110	0

as the fraction of all possible candidates that were observed) to be $1546/8626 \approx 20\%$. However, when only considering the priority 1 objects, we find that we were able to study and assign candidature for 781 out of the 1517 objects, resulting in $\approx 50\%$ completeness. Similarly we estimate the completeness of the study of the priority 2 and priority 3 objects to be $\approx 10\%$ and $\approx 15\%$, respectively.

We can provide a rough estimate of the number of optically visible post-AGB and post-RGB candidates we expect to find in the unstudied sample (see Table 8). Out of the 781 priority 1 objects, 34 turned out to be post-AGB candidates. So for the remaining unstudied sample of $1517 - 781 = 736$ priority 1 candidates we can expect ≈ 32 more post-AGB candidates in the whole LMC. One out of the 721 priority 2 objects turned out to be post-AGB candidates. So from the remaining unstudied sample of 6102 priority 2 candidates, we can expect ≈ 8 more post-AGB candidates. None of the priority 3 candidates are post-AGB stars and therefore we do not expect to find any post-AGB stars from the remaining unstudied sample of priority 3 objects. Similarly, based on the numbers of post-RGB objects, in the LMC we expect to find ≈ 32 additional post-RGB candidates from the priority 1 unstudied sample and ≈ 719 post-RGB candidates from the priority 2 unstudied sample. This implies that it might be possible to identify a further group of ≈ 40 optically visible post-AGB candidates and ≈ 751 optically visible post-RGB candidates from the total unstudied group of initially selected candidates in the LMC. We note that the number of observed and expected post-RGB candidates with priority 2 is much larger than the objects with priority 1, because while assigning priority for spectroscopic observations, priority 1 was assigned to objects with luminosities in-between $1000 L_{\odot}$ and $35000 L_{\odot}$, while priority 2 was assigned to objects with luminosities $< 1000 L_{\odot}$, where it is more likely to find post-RGB stars. Since priority 3 is assigned to those objects with luminosities $> 35000 L_{\odot}$, as

expected, we do not find any post-RGB objects with priority 3.

As part of the future work, we intend to complete the survey by observing the unstudied sample of objects. We note that out of the 556 objects that we rejected based on low signal spectrum, 456 objects were faint with V, I or R band magnitudes greater than 17 mags. For these objects a larger exposure time than that used obtain the current spectrum or a larger telescope would be required to obtain a more suitable spectrum. For the remaining 101 out of the 556 objects, it is likely that they were either observed in poor observing conditions or subject to a bad fibre alignment.

We note that the above estimated completeness applies only to optically visible post-AGB and post-RGB stars. We do not take into account the fainter or heavily enshrouded objects.

12 ESTIMATING POST-AGB AND POST-RGB EVOLUTIONARY RATES

To be able to estimate the evolutionary rate, a complete sample of post-AGB and post-RGB stars is required. During the post-AGB phase, for a particular luminosity, T_{eff} is determined by the mass of the hydrogen envelope (Schönberner 1981; Vassiliadis & Wood 1994). The rate of evolution in T_{eff} is therefore determined by the luminosity (which determines the rate of consumption of the hydrogen envelope by nuclear burning) and by the mass loss rate (in the case of single post-AGB stars) and the mass re-accretion rate (in the case binary of post-AGB and post-RGB stars). This mass loss rate/mass accretion rate is essentially completely unknown. Based on the available sample of post-AGB and post-RGB candidates from this study, we now try to estimate this mass loss/accretion rate by determining the numbers of stars in a given T_{eff} interval along the post-AGB and post-RGB tracks and comparing those numbers to the number of stars in the

top magnitude of the RGB, where the duration of evolution is known.

To estimate the lifetime on the top one magnitude of the RGB, we used the Bertelli et al. (2008) evolutionary tracks. They show that stars in the mass range 1.0 to 1.8 M_{\odot} and LMC-like metallicity take $\sim 3 \times 10^6$ years to traverse the top magnitude of the RGB. Subsequent AGB evolution through the same luminosity range takes $\sim 1 \times 10^6$ years. Hence, the total time spent by a low mass star in the luminosity range corresponding to the top one magnitude of the RGB is $\sim 4 \times 10^6$ years.

In order to estimate the observed number of stars on the top magnitude of the RGB in the nine fields LMC 1-9, we followed the prescriptions in Nie et al. (2012). Stars in the SAGE (Meixner et al. 2006; Blum et al. 2006) catalog were plotted in the J , $J-[3.6]$ diagram and those in a parallelogram coinciding with the top 1 magnitude of the RGB were selected. The parallelogram has sides $J=13.9$, $J=14.9$, $J-[3.6]=3.25 - 0.17J$ and $J-[3.6]=3.75 - 0.17J$. We find the numbers of stars $n_1, n_2, n_3, n_4, n_5, n_6, n_7, n_8$ and n_9 in each of LMC1, LMC2, LMC3, LMC4, LMC5, LMC6, LMC7, LMC8 and LMC9 are 34198, 19727, 16258, 6686, 4881, 11480, 10859, 7346 and 7491, respectively, with an error of approximately 5% (Nie et al. 2012). The total number of stars in the magnitude interval corresponding to the top mag of the RGB in all 9 LMC fields is thus 118927.

Next we estimated the lifetimes of the stars in the early part of the post-AGB and post-RGB phase. If we assume that post-AGB stars, whether they leave the AGB by single star mass loss or binary interaction, have all passed through the top magnitude of the RGB then we can easily derive their average post-AGB lifetime. If there are N_{AGB} post-AGB stars ($\log L \gtrsim 3.4$) in all 9 LMC fields in a certain evolutionary phase (say from the AGB to $T_{\text{eff}} = 10000$ K i.e. $\sim 3.6 < \log T_{\text{eff}} < \sim 4.0$), then the lifetime of these stars in that evolutionary phase is $4 \times 10^6 * N_{\text{AGB}} / 118927$ years. From our analysis, we find a total of $N_{\text{AGB}} = 35$ which results in a post-AGB lifetime of 1177 yrs. For post-RGB stars, the calculation is not so easy. Nie et al. (2012) find that $\sim 4\%$ of red giants evolving up the RGB produce post-RGB stars when they fill their Roche lobes before reaching the RGB tip. Most of the post-RGB stars are produced during the top two magnitudes of the RGB where most of our post-RGB stars are observed. The median luminosity of these stars is $\log L / L_{\odot} \sim 2.8$. In this case, if N_{RGB} post-RGB stars are observed, then their average lifetime is $4 \times 10^6 * (N_{\text{RGB}} / 0.04) / 118927$ years. From our analysis, we find a total of $N_{\text{RGB}} = 119$ post-RGB candidates, which results in a post-RGB lifetime of 100061 yrs.

The estimated lifetime assumes that the samples of post-AGB and post-RGB candidates in the fields LMC 1 – 9 is complete. However, as mentioned in Section 11, our survey is not entirely complete and we can expect to find an additional sample of 40 post-AGB candidates and 751 post-RGB candidates. To illustrate the impact of this addition, we recalculated the lifetimes and we estimate a post-AGB lifetime of 2522 yrs and a post-RGB lifetime of 731541 yrs.

We need to compare the above post-AGB lifetime to that of post-AGB stars without external mass loss during the post-AGB life. Following the procedures in Paper I, we estimated evolutionary times for a post-AGB to traverse the interval $3.7 < \log T_{\text{eff}} < 4.0$ where most of the observed

post-AGB stars lie and also for a post-RGB star to traverse from $\log T_{\text{eff}}(\text{RGB}) + 0.05$ to $\log T_{\text{eff}} = 4.0$ by consuming the hydrogen-rich envelope. The lifetime for post-AGB evolution without post-AGB mass loss from $\log T_{\text{eff}} = 3.7$ to 4.0 and for an intermediate luminosity star ($\log L / L_{\odot} = 3.8$) was estimated to be 9800 yrs. From the observations of the post-AGB stars in the LMC, we find an observational lifetime of 2522 yrs for the post-AGB stars. Formally, the numbers suggest that for the post-AGB stars, some mass loss is required to hasten the evolution. This mass loss rate is $M_{\odot} \approx 2.7 \times 10^{-7} M_{\odot} / \text{yr}$, but the uncertainties are very large and we do not consider the post-AGB binaries (with mass-accretion).

Using the procedures in Paper I, we find that the post-RGB evolution time without mass loss from $\log T_{\text{eff}}(\text{RGB}) + 0.05$ to $\log T_{\text{eff}} = 4.0$ and for an intermediate luminosity star ($\log L / L_{\odot} = 3.0$) is 109000 years (the envelope mass is assumed to be consumed by hydrogen burning only). From the observations of post-RGB stars in the LMC, we find an observational lifetime of 731541 years which is greater than the theoretically predicated lifetime therefore suggesting mass-accretion on the post-RGB, as expected for these likely binary objects. The mass accretion rate formally required to slow down the evolution to give the observed number of post-RGB stars is $M_{\odot} \approx 1.0 \times 10^{-8} M_{\odot} / \text{yr}$.

Finally, we note that our calculations of lifetimes do not include the possibility that some objects in the post-AGB and post-RGB phases could be heavily dust enshrouded and therefore not observed by us. If there are significant numbers of these objects then our estimate observational lifetimes will be underestimated, our post-AGB mass loss rates will be overestimated and our post-RGB accretion rates will be slightly underestimated.

13 SUMMARY AND CONCLUSIONS

In the LMC, we have identified a sample of 35 well characterised high probability optically visible post-AGB candidates with spectroscopically determined stellar parameters (T_{eff} , $\log g$, $[\text{Fe}/\text{H}]$ and $E[B - V]$) spanning a wide range in luminosities. These objects have spectral types between A and K and being an evolved class of objects, they have a lower metallicity ($[\text{Fe}/\text{H}] \approx -1.0$) than the mean present-day LMC metallicity. Their spectral energy distributions and their locations on the $[8] - [24]$ vs $[3.6] - [4.5]$ colour-colour plot allowed us to distinguish between shell-sources, (with a double-peaked SED) and disc-sources (with an SED that is indicative of hot circumstellar material). Out of the 35 post-AGB candidates, we found a group of 10 shell-sources and 23 disc-sources. For the remaining 2 sources, we were unable to classify them based on their SEDs. The low-resolution spectra of the post-AGB objects revealed a diversity in their $\text{H}\alpha$ line profiles. Some objects showed a line profile with a strong emission component along with a weaker absorption component, indicative of strong stellar winds, while other objects showed a strong absorption component with a weaker emission component, indicative of on-going weak mass loss. We were also able to identify the presence of barium for 6 candidates, which is an expected product of the nucleosynthesis during the AGB phase of evolution.

The determination of the photospheric luminosity (L_{ph})

confirmed the existence of optically visible dusty post-RGB stars by revealing 119 such candidates. This class of objects was discovered in our SMC survey (see Paper I). These objects have mid-IR excesses and stellar parameters similar to those of post-AGB stars (late-G to late-A spectral types, low $\log g$ values, and low metallicities with $[\text{Fe}/\text{H}] \approx -1.0$). However, their luminosities (≈ 100 – $2500 L_{\odot}$), and hence masses and radii, are much lower than those expected for post-AGB stars. We expect these objects to be a result of mass loss induced via binary interaction that terminates their RGB phase. Detailed radial velocity monitoring studies are required to confirm the true nature of all these sources. Based on their SEDs, we were able to classify the 119 post-RGB stars into groups of 23 shell-sources and 56 disc-sources. For the remaining 40 sources we were unable to classify them based on their SEDs. The low-resolution spectra of the post-RGB candidates also showed similar $\text{H}\alpha$ profiles as the post-AGB stars. Furthermore, we were able to identify the presence of barium in two of these objects. One of these objects, J051453.10-691723.5, is likely to be a post-AGB star since its central star luminosity is close to the post-AGB–post-RGB dividing line of $\approx 2500 L_{\odot}$. The second object, J054034.77-683228.2, is a low-luminosity star and since post-RGB stars have not yet gone through the AGB phase, it is likely that this object falls in the category of Ba-stars, which are objects that are extrinsically enriched by binary mass transfer.

This study has also resulted in a large sample of luminous YSOs, since YSOs are also surrounded by large amounts of circumstellar material (and display a large IR excess) and are present in the luminosity range occupied by post-AGB and post-RGB stars. We used a $\log g$ criterion to disentangle the YSOs since at a given luminosity, the mass of a YSO is about 15–20 times that of the corresponding post-AGB/post-RGB star, leading to a difference of 1.3 in $\log g$ between them. This resulted in a sample of 162 high probability YSO candidates, majority of which are newly identified in this study. These objects have temperatures ranging between 4000K and 9000K, high surface gravities, and a mean metallicity $[\text{Fe}/\text{H}] \approx -0.60$, which agrees well with the average present-day LMC metallicity. From the position of these YSO candidates on the HR diagram, we were able to infer that they have masses of ~ 3 – $10 M_{\odot}$. The YSO candidates showed $\text{H}\alpha$ emission and forbidden line emission indicative of disc accretion in YSOs. We were also able to identify the presence of Li in eleven candidates.

Our detailed spectroscopic analysis combined with our robust $\log g$ criterion has provided a systematic characterisation of the objects in our study and in some cases revealed the true nature of the objects. For instance, J050830.51-692237.4 was previously classified as an oxygen-rich post-AGB star by Woods et al. (2011) based on IRS spectra. The study by van Aarle et al. (2011) classified this object as a C-star. However, based on the $\log g$ value of this object and inspection of its spectrum and SED, we find that this object is more likely to be a YSO with a O-rich disc and in the line-of-sight of the object is a non-related C-star. Another object, J053253.51-695915.1, which is a low-luminosity object that shows a mild *s*-process enrichment, was classified as a *s*-process rich post-AGB star by van Aarle et al. (2013). However, this object has too low a luminosity to be a post-AGB star and based on the $\log g$ value of the object, our studies reveal that this object is likely a YSO, indicating

that the mild *s*-process enhancement comes from the initial composition of the LMC (Van der Swaelmen et al. 2013).

We note that the classification of post-AGB, post-RGB and YSO candidates depend significantly on their estimated stellar parameters (T_{eff} , $\log g$, $[\text{Fe}/\text{H}]$, $E(B-V)$ and luminosity). Since our study is performed using low-resolution spectra, this study results in spectroscopically verified, likely optically bright post-AGB, post-RGB and YSO candidates. To confirm their nature, follow-up studies with high-resolution spectra are essential.

Other interesting by-products of this survey include a group of 69 hot objects whose spectra show emission lines and in some cases, a significant UV continuum. These objects are likely to be either hot post-AGB, post-RGB or luminous YSO candidates. Fifteen of these objects are likely to be B[e] star candidates, out of which 12 are newly discovered.

This study has also resulted in the discovery of a significant number of contaminants. They are: M-stars, C-stars and PNe (presented in Appendix A), a group of QSOs and redshifted galaxies (to be presented in a following publication), a group of stars with TiO band emission (Wood et al. 2013), a group of luminous supergiants and a group of hot main-sequence stars (to be presented in a following publication).

We note that, due to limitations introduced by the selection criteria, our study is restricted to optically visible post-AGB and post-RGB stars of spectral type A – K, in the LMC. The completeness of this survey is $\approx 20\%$ since we were not able to obtain spectra all of the candidates from within the initially selected sample of candidates. Some of the candidates with optical spectra were rejected as their spectra were of poor quality due to the faintness of the targets (majority of which had $V \text{ mag} > 17$ mags) combined with the low resolution of our spectra (≈ 1300). Based on the current final sample of post-AGB/RGB candidates (of A – K) in the LMC, we expect to find approximately an additional 40 optically visible post-AGB and 751 optically visible post-RGB candidates from the remaining unstudied initial sample selection of objects. We note that the estimated completeness and the expected numbers of remaining post-AGB/post-RGB stars only apply to optically visible objects and do not include objects that are faint ($V > 20$) or heavily dust enshrouded.

We also used the numbers of the post-AGB and post-RGB objects, to study the evolutionary rates as well as the mass loss/mass accretion rates. Though the uncertainties are large, we found that the number of post-AGB stars require stellar evolution models with some mass-loss and the number of post-RGB stars suggests re-accretion of gas.

This study has provided a rich sample of post-AGB stars and a new population of dusty post-RGB stars that cover a wide range of luminosities and hence masses. Our on-going and future work includes investigating the chemical properties of these objects using high-resolution optical UVES spectra. The known luminosities and chemical abundances of these objects will provide excellent constraints for AGB nucleosynthesis models. We also intend to perform a long-term radial velocity monitoring of these objects, especially the newly discovered dusty post-RGB sample. This will help establish their likely binary nature and a possibility to probe this unexplored phase of stellar evolution.

Additional future work aims at characterising in detail the diverse samples of contaminants with IR excesses.

ACKNOWLEDGMENTS

DK acknowledges support of the FWO grant G.OB86.13. HVW and DK acknowledge support of the KU Leuven contract GOA/13/012. PRW acknowledges support from Australian Research Council Discovery Project DP120103337. We thank the Australian Astronomical Observatory for allowing us to use the observatory facilities and our AAT support astronomer, Dr. Paul Dobbie, who was very helpful during our observing run. We thank the AAO Service Program, especially Dr. Sarah Brough and Dr. Daniel Zucker, our service observers, for observing three of the LMC fields. We would also like to thank the referee for his/her useful comments and suggestions.

REFERENCES

Abate C., Pols O. R., Izzard R. G., Mohamed S. S., de Mink S. E., 2013, *A&A*, 552, A26
 Alcock C. et al., 2002, *ApJ*, 573, 338
 Balick B., Frank A., 2002, *ARA&A*, 40, 439
 Bertelli G., Girardi L., Marigo P., Nasi E., 2008, *A&A*, 484, 815
 Bertelli G., Nasi E., Girardi L., Marigo P., 2009, *A&A*, 508, 355
 Blöcker T., 1995, *A&A*, 297, 727
 Blum R. D. et al., 2006, *AJ*, 132, 2034
 Bolatto A. D. et al., 2007, *ApJ*, 655, 212
 Bonanos A. Z. et al., 2009, *AJ*, 138, 1003
 Boothroyd A. I., Sackmann I.-J., Wasserburg G. J., 1995, *ApJ*, 442, L21
 Bujarrabal V., Alcolea J., Van Winckel H., Santander-García M., Castro-Carrizo A., 2013a, *A&A*, 557, A104
 Bujarrabal V., Castro-Carrizo A., Alcolea J., Van Winckel H., Sánchez Contreras C., Santander-García M., Neri R., Lucas R., 2013b, *A&A*, 557, L11
 Cardelli J. A., Clayton G. C., Mathis J. S., 1989, *ApJ*, 345, 245
 Castelli F., Kurucz R. L., 2003, in *IAU Symposium*, Vol. 210, *Modelling of Stellar Atmospheres*, Piskunov N., Weiss W. W., Gray D. F., eds., p. 20P
 Castelli F., Kurucz R. L., 2004, *ArXiv:astro-ph/0405087*
 Chen X., Han Z., Tout C. A., 2011, *ApJ*, 735, L31
 Chiosi C., Wood P. R., Capitanio N., 1993, *ApJS*, 86, 541
 Cioni M. R., Habing H. J., Loup C., Groenewegen M. A. T., Epchtein N., DENIS Consortium, 1999, in *IAU Symposium*, Vol. 192, *The Stellar Content of Local Group Galaxies*, Whitelock P., Cannon R., eds., p. 65
 Cioni M.-R. L. et al., 2013, *A&A*, 549, A29
 Clementini G., Gratton R., Bragaglia A., Carretta E., Di Fabrizio L., Maio M., 2003, *AJ*, 125, 1309
 de Ruyter S., Van Winckel H., Maas T., Lloyd Evans T., Waters L. B. F. M., Dejonghe H., 2006, *A&A*, 448, 641
 De Smedt K., Van Winckel H., Karakas A. I., Siess L., Goriely S., Wood P. R., 2012, *A&A*, 541, A67
 Dermine T., Izzard R. G., Jorissen A., Van Winckel H., 2013, *A&A*, 551, A50

Deroo P., Van Winckel H., Verhoelst T., Min M., Reyniers M., Waters L. B. F. M., 2007, *A&A*, 467, 1093
 Egan M. P., Van Dyk S. D., Price S. D., 2001, *AJ*, 122, 1844
 Field G. B., 1973, *Science*, 179, 991
 Fraser O. J., Hawley S. L., Cook K. H., 2008, *AJ*, 136, 1242
 Frew D. J., Parker Q. A., 2010, *PASA*, 27, 129
 Frogel J. A., Cohen J. G., Persson S. E., 1983, *ApJ*, 275, 773
 Gauba G., Parthasarathy M., 2004, *A&A*, 417, 201
 Gielen C. et al., 2011a, *A&A*, 533, A99
 Gielen C. et al., 2011b, in *Astronomical Society of the Pacific Conference Series*, Vol. 445, *Why Galaxies Care about AGB Stars II: Shining Examples and Common Inhabitants*, Kerschbaum F., Lebzelter T., Wing R. F., eds., p. 281
 Gielen C. et al., 2009, *A&A*, 508, 1391
 Giridhar S., Lambert D. L., Reddy B. E., Gonzalez G., Yong D., 2005, *ApJ*, 627, 432
 Gordon K. D. et al., 2011, *AJ*, 142, 102
 Gorlova N., Van Winckel H., Vos J., Ostensen R. H., Jorissen A., Van Eck S., Ikonnikova N., 2014, *ArXiv e-prints*.
 Groenewegen M. A. T., Sloan G. C., Soszyński I., Petersen E. A., 2009, *A&A*, 506, 1277
 Gruendl R. A., Chu Y.-H., 2009, *ApJS*, 184, 172
 Han Z., Podsiadlowski P., Eggleton P. P., 1995, *MNRAS*, 272
 Heber U., 2009, *ARA&A*, 47, 211
 Hillen M. et al., 2013, *A&A*, 559, A111
 Hora J. L. et al., 2008, *AJ*, 135, 726
 Hrivnak B. J., Lu W., Bohlender D., Morris S. C., Woodsworth A. W., Scarfe C. D., 2011, *ApJ*, 734, 25
 Jayawardhana R., Mohanty S., Basri G., 2002, *ApJ*, 578, L141
 Kamath D., Wood P. R., Van Winckel H., 2014, *MNRAS*, 439, 2211
 Karakas A. I., Lattanzio J. C., 2003, *PASA*, 20, 279
 Karakas A. I., Lattanzio J. C., 2007, *PASA*, 24, 103
 Karakas A. I., Lattanzio J. C., 2014, *ArXiv e-prints*.
 Keller S. C., Wood P. R., 2006, *ApJ*, 642, 834
 Kirkpatrick J. D. et al., 1999, *ApJ*, 519, 802
 Kontizas E., Dapergolas A., Morgan D. H., Kontizas M., 2001, *A&A*, 369, 932
 Kozłowski S., Kochanek C. S., 2009, *ApJ*, 701, 508
 Kozłowski S. et al., 2012, *ApJ*, 746, 27
 Kraemer K. E., Sloan G. C., Bernard-Salas J., Price S. D., Egan M. P., Wood P. R., 2006, *ApJ*, 652, L25
 Kučinskas A., Vansevicius V., Sauvage M., Tanabé T., 2000, *A&A*, 353, L21
 Kwok S., 1993, *araa*, 31, 63
 Lamers H. J. G. L. M., Beaulieu J. P., de Wit W. J., 1999, *A&A*, 341, 827
 Lasker B. M. et al., 2008, *AJ*, 136, 735
 Lattanzio J., Frost C., Cannon R., Wood P. R., 1996, *Mem. Soc. Astron. Italiana*, 67, 729
 Levato H., Miroshnichenko A. S., Saffe C., 2014, *A&A*, 568, A28
 Lewis I. J. et al., 2002, *MNRAS*, 333, 279
 Maas T., Van Winckel H., Lloyd Evans T., 2005, *A&A*, 429, 297
 Massey P., 2002, *ApJS*, 141, 81
 Matsuura M. et al., 2014, *MNRAS*, 439, 1472

- Meixner M. et al., 2006, *AJ*, 132, 2268
- Min M., Jeffers S. V., Canovas H., Rodenhuis M., Keller C. U., Waters L. B. F. M., 2013, *A&A*, 554, A15
- Miroshnichenko A. S., 2007, *ApJ*, 667, 497
- Miszalski B., Napiwotzki R., Cioni M.-R. L., Groenewegen M. A. T., Oliveira J. M., Udalski A., 2011, *A&A*, 531, A157
- Miszalski B., Shortridge K., Saunders W., Parker Q. A., Croom S. M., 2006, *MNRAS*, 371, 1537
- Morgan D. H., Cannon R. D., Hatzidimitriou D., Croke B. F. W., 2003, *MNRAS*, 341, 534
- Munari U., Sordo R., Castelli F., Zwitter T., 2005, *A&A*, 442, 1127
- Natta A., Testi L., Comerón F., Oliva E., D'Antona F., Baffa C., Comoretto G., Gennari S., 2002, *A&A*, 393, 597
- Neugebauer G. et al., 1984, *ApJ*, 278, L1
- Neugent K. F., Massey P., Skiff B., Meynet G., 2012, *ApJ*, 749, 177
- Nie J. D., Wood P. R., Nicholls C. P., 2012, *MNRAS*, 423, 2764
- Palla F., Stahler S. W., 1993, *ApJ*, 418, 414
- Rao S. S., Giridhar S., Lambert D. L., 2012, *MNRAS*, 419, 1254
- Reid W. A., 2014, *MNRAS*, 438, 2642
- Reid W. A., Parker Q. A., 2006, *MNRAS*, 373, 521
- Reid W. A., Parker Q. A., 2010, *MNRAS*, 405, 1349
- Reid W. A., Parker Q. A., 2013, *MNRAS*, 436, 604
- Reyniers M., Van Winckel H., 2003, *A&A*, 408, L33
- Reyniers M., Van Winckel H., Gallino R., Straniero O., 2004, *A&A*, 417, 269
- Schönberner D., 1981, *A&A*, 103, 119
- Seale J. P., Looney L. W., Chu Y.-H., Gruendl R. A., Brandl B., Chen C.-H. R., Brandner W., Blake G. A., 2009, *ApJ*, 699, 150
- Sharp R. et al., 2006, in *Society of Photo-Optical Instrumentation Engineers (SPIE) Conference Series*, Vol. 6269, *Society of Photo-Optical Instrumentation Engineers (SPIE) Conference Series*
- Skrutskie M. F. et al., 2006, *AJ*, 131, 1163
- Soker N., 2014, *ArXiv e-prints*.
- Soszyński I. et al., 2009a, *Acta Astron.*, 59, 239
- Soszyński I. et al., 2008, *Acta Astron.*, 58, 293
- Soszyński I. et al., 2009b, *Acta Astron.*, 59, 335
- Stahler S. W., 1983, *ApJ*, 274, 822
- Szczerba R., Siódmiak N., Stasińska G., Borkowski J., 2007, *A&A*, 469, 799
- Tisserand P. et al., 2009, *A&A*, 501, 985
- Tognelli E., Prada Moroni P. G., Degl'Innocenti S., 2011, *A&A*, 533, A109
- Tonry J., Davis M., 1979, *AJ*, 84, 1511
- van Aarle E., Van Winckel H., De Smedt K., Kamath D., Wood P. R., 2013, *A&A*, 554, A106
- van Aarle E., Van Winckel H., Lloyd Evans T., Ueta T., Wood P. R., Ginsburg A. G., 2011, *A&A*, 530, A90+
- Van de Steene G. C., van Hoof P. A. M., Wood P. R., 2000, *A&A*, 362, 984
- van de Steene G. C., Wood P. R., van Hoof P. A. M., 2000, in *Astronomical Society of the Pacific Conference Series*, Vol. 199, *Asymmetrical Planetary Nebulae II: From Origins to Microstructures*, Kastner J. H., Soker N., Rappaport S., eds., p. 191
- van der Marel R. P., Alves D. R., Hardy E., Suntzeff N. B., 2002, *AJ*, 124, 2639
- Van der Swaelmen M., Hill V., Primas F., Cole A. A., 2013, *A&A*, 560, A44
- Van Winckel H., 2003, *ARA&A*, 41, 391
- Van Winckel H., 2007, *Baltic Astronomy*, 16, 112
- Van Winckel H. et al., 2009, *A&A*, 505, 1221
- Van Winckel H., Reyniers M., 2000, *A&A*, 354
- Vanden Berk D. E. et al., 2001, *AJ*, 122, 549
- Vassiliadis E., Wood P. R., 1993, *ApJ*, 413, 641
- Vassiliadis E., Wood P. R., 1994, *ApJS*, 92, 125
- Volk K. et al., 2011, *ApJ*, 735, 127
- Wallerstein G., Knapp G. R., 1998, *ARA&A*, 36, 369
- Waters L. B. F. M., Waelkens C., Van Winckel H., 1997, in *IAU Symposium*, Vol. 180, *Planetary Nebulae*, Habing H. J., Lamers H. J. G. L. M., eds., p. 313
- Whitlock P. A., Feast M. W., Menzies J. W., Catchpole R. M., 1989, *MNRAS*, 238
- Whitney B. A. et al., 2008, *AJ*, 136, 18
- Wood P. R. et al., 1999, in *IAU Symposium*, Vol. 191, *Asymptotic Giant Branch Stars*, Le Bertre T., Lebre A., Waelkens C., eds., p. 151
- Wood P. R., Cohen M., 2001, in *Astrophysics and Space Science Library*, Vol. 265, *Astrophysics and Space Science Library*, Szczerba R., Górny S. K., eds., p. 71
- Wood P. R., Kamath D., Van Winckel H., 2013, *MNRAS*, 435
- Wood P. R., Zarro D. M., 1981, *ApJ*, 247, 247
- Woods P. M. et al., 2011, *MNRAS*, 411, 1597
- Wright E. L. et al., 2010, *AJ*, 140, 1868
- Yang M., Jiang B. W., 2011, *ApJ*, 727, 53
- Zaritsky D., Harris J., Thompson I. B., Grebel E. K., 2004, *AJ*, 128, 1606
- Zickgraf F., 2000, in *Astronomical Society of the Pacific Conference Series*, Vol. 214, *IAU Colloq. 175: The Be Phenomenon in Early-Type Stars*, Smith M. A., Henrichs H. F., Fabregat J., eds., p. 26
- Zickgraf F.-J., 2006, in *Astronomical Society of the Pacific Conference Series*, Vol. 355, *Stars with the B[e] Phenomenon*, Kraus M., Miroshnichenko A. S., eds., p. 135

APPENDIX A: TABLES OF THE PN, C-STARS, AND M-STARS IN OUR SAMPLE

Here, we present the list of C-stars (Table A1), M-stars (Table A2) and the PNe (Table A3). For the PNe objects listed in Table A3, we separate the objects into the previously catalogued PNe and the newly identified likely PN candidates, identified based on the visual inspection of their spectra, as mentioned in Section 4. In Table A3, we also perform a positional cross-matching of all the objects to the most relevant previous studies (see Table 4 for a list of catalogues using which the positional cross-matching was performed). Based on the result of the positional cross-matching, out of the 123 PNe in our study, 91 objects have been previously catalogued as PNe, while the remaining 32 objects have not been catalogued as PNe. Some of these objects have been classified as YSOs or QSOs, based on either photometric classifications (e.g., Gruendl & Chu 2009; Whitney et al. 2008) or inspection of Spitzer Space Telescope (SST) spectra (e.g., Seale et al. 2009). Therefore, we refer to these objects as

uncatalogued planetary nebula candidates. A follow-up detailed spectral analysis is required to confirm the PN nature of these objects.

Table A1. The C-stars in our sample

Name	Name	Name	Name	Name
J044114.11-700109.5	J050040.18-682911.6	J051028.50-694704.4	J052046.78-690124.1	J052805.91-700753.4
J044542.06-700352.8	J050252.33-690252.6	J051121.80-693456.0	J052224.83-693837.4	J052943.72-700913.9
J044918.46-695314.5	J050403.80-675408.0	J051255.63-704551.1	J052248.93-714312.1	J053004.33-722253.4
J044941.97-683821.1	J050508.30-701242.0	J051307.99-683311.8	J052337.00-700905.4	J053030.25-683807.7
J045111.42-710001.0	J050527.05-690643.6	J051320.59-703928.3	J052346.76-684653.0	J053128.44-701027.1
J045144.79-661757.0	J050536.98-701734.4	J051405.00-682758.4	J052419.63-710424.9	J053556.87-690045.0
J045241.94-713137.5	J050538.97-684732.1	J051435.67-713837.0	J052500.49-694811.8	J053738.67-712124.0
J045543.20-675110.1	J050558.23-680923.6	J051734.05-692609.4	J052619.82-681602.1	J054124.63-694806.5
J045645.54-675048.6	J050606.51-690302.7	J051807.82-685355.9	J052714.36-712731.8	J054216.19-695636.6
J045731.30-663232.0	J050733.83-692119.9	J052010.84-684212.3	J052747.03-691913.4	J054406.22-701342.1
J045902.04-692102.1	J050839.80-681205.6	J052040.41-691909.2	J052755.27-695828.8	J054418.29-705320.3

Table A3. The new planetary nebula candidates and previously known planetary nebulae in our sample.

Name	Previous Identification	Name	Previous Identification
Uncatalogued planetary nebula candidates			
J045108.87-684905.3	-	J053142.45-683245.3	YSO/G ⁵
J045703.49-684513.5	YSO ⁵	J053208.55-674004.0	YSO/G ⁵
J045811.72-662211.3	YSO ⁵ , YSO-PE ²⁰	J053355.00-672705.5	G/YSO ⁵ , QSO ⁹
J050305.59-683337.0	-	J053609.54-691805.4	YSO ⁵
J050432.15-704412.0	YSO ⁵ , YSO-hp ²⁸	J053615.83-693151.1	YSO ⁵ , YSO-PE ²⁰ , YSO-hp ²⁸
J050558.68-693953.6	YSO ⁵	J053705.13-691406.0	-
J050849.56-684405.1	-	J053845.34-690251.3	YSO ⁵
J050937.01-675508.8	YSO/G ⁵	J053853.87-690931.2	YSO ⁵ , YSO-PE ²⁰
J051829.16-691458.2	YSO ⁵	J053932.39-690005.8	-
J052147.07-675656.6	YSO ⁵ , YSO-PE ²⁰ , YSO-hp ²⁸	J053938.25-685740.2	G ⁵ , YSO ²⁸
J052559.86-671019.4	YSO ⁵ , YSO ⁹ , YSO-hp ²⁸	J054000.73-694713.4	YSO ⁵ , YSO-PE ²⁰
J052609.17-690059.2	-	J054046.97-700308.7	-
J052633.00-672705.1	YSO ⁵ , QSO ⁹	J054142.68-711928.3	YSO ⁵ , YSO ⁹
J052708.12-685230.5	YSO ⁵	J054309.31-694454.4	YSO ²⁸
J052852.95-710920.3	YSO ⁵	J054519.52-711606.9	Evolved ²⁸ , LPV ⁴
J053132.96-701827.7	YSO ⁵	J054855.15-700510.7	YSO ⁵ , YSO ⁹ , YSO-hp ²⁸
Previously identified planetary nebulae			
J044829.55-690813.0	PN ²⁸ , QSO ⁹	J052456.62-691530.9	PN ^{7,28}
J045013.12-693356.9	PN ^{5,7,28} , YSO ⁹	J052525.97-685553.8	PN ^{5,28}
J045201.45-683917.1	PN ^{7,28}	J052743.78-712556.5	PN ^{5,7,16,28}
J045959.97-702741.2	PN ^{5,7,16}	J052801.54-701331.6	PN ^{7,16}
J050052.64-701341.0	PN ^{5,7,16}	J052804.80-685947.2	YSO ⁵ , YSO-PE ²⁰ , PN ²⁸
J050058.17-680748.9	PN ¹⁶	J052834.40-703302.7	PN ^{7,16}
J050341.21-701353.5	PN ^{5,7,16}	J052841.01-673339.2	PN ^{7,16,28}
J050342.60-700647.4	PN ^{7,16,28}	J052902.79-701924.2	PN ^{7,16,28} , QSO ⁹
J050427.64-685811.5	PN ^{7,16}	J052915.66-673247.4	C ⁸ , PN ^{5,7,16,28}
J050434.20-675221.8	PN ^{16,28} , UNK ²⁹ , YSO ⁹	J052918.33-702349.9	PN ^{7,16}
J050451.97-683909.7	PN ⁵	J052926.57-723843.1	PN ⁷
J050609.37-674527.5	PN ⁵	J052932.73-701738.7	PN ^{7,16}
J050623.88-690319.3	PN ^{5,7,16}	J053033.17-704437.9	PN ⁵ , PN ^{7,16}
J050643.81-691538.1	PN ^{7,16}	J053055.57-672006.2	YSO ⁵ , YSO-P ²⁰ , PN ^{16,28} , yso-L ¹⁹
J050730.70-690808.6	PN ^{5,16,28}	J053059.48-683541.2	PN ^{5,16,28}
J050757.61-685147.5	PN ²⁸ , YSO ⁹	J053108.97-713640.6	PN ⁷
J050803.34-684016.7	PN ^{5,28}	J053115.90-710508.1	YSO/G ⁵ , PN ¹⁰ , YSO ⁹ , YSO-hp ²⁸
J050911.13-673402.6	PN ^{7,16}	J053121.88-704045.3	PN ^{5,7,16} , RRLab ¹
J050920.18-674725.0	PN ^{5,7,16,28}	J053308.84-711803.3	PN ¹⁶
J050937.20-704908.6	PN ^{5,7,16,28} , QSO ⁹	J053313.06-723647.2	PN ⁷
J051009.41-682954.6	PN ^{5,7,16,28}	J053329.77-715228.7	PN ^{5,7}
J051017.11-684822.6	PN ^{5,7,16,28}	J053346.97-683644.2	C-PN ²⁹ , PN ^{5,7,16,28}
J051039.65-683604.8	PN ^{5,7,16}	J053356.10-675308.9	PN ^{5,7,16,28}
J051102.94-674759.2	PN ^{5,7,16,28}	J053406.23-692618.4	PN ^{5,7,12,16,28}
J051141.99-683459.8	PN ^{5,7,28}	J053421.19-685825.2	PN ^{5,7,12,16,28}
J051327.23-703335.0	PN ^{7,16}		
J051342.30-681516.4	PN ^{7,16}	J053430.21-702834.8	PN ^{7,16}
J051546.75-684223.5	PN ^{7,16,28}	J053438.84-701956.7	PN ^{7,16}
J051702.45-690716.5	PN ^{10,16,28} , QSO ⁹	J053448.02-684835.7	PN ^{12,16,28}
J051743.59-711533.9	PN ¹⁰ , YSO ⁹ , YSO-hp ²⁸	J053510.23-693939.1	PN ^{7,12,16,28}
J051929.62-685109.1	PN ^{7,16,28}	J053557.56-695816.9	PN ^{5,7,12,16,28} , QSO ⁹
J051954.62-693104.9	PN ^{5,7,16,28}	J053630.83-691817.3	YSO ⁵ , PN ²⁰ , YSO-hp ²⁸
J052009.35-702538.1	PN ^{7,16}	J053652.96-715338.6	PN ^{5,7}
J052009.50-695339.0	PN ^{16,28}	J053710.26-712314.3	O-PN ²⁹ , PN ^{10,16} , QSO ⁹
J052034.66-683518.2	YSO ⁵ , PN ^{16,28}	J053737.93-714137.7	PN ⁷
J052052.42-700935.5	C-PN ²⁹ , PN ^{5,7,16,28}	J054008.62-685826.9	LPV/HII ¹² , PN ^{16,28} , EclBin ¹⁹
J052056.03-700513.1	PN ^{5,16,28}	J054045.04-702806.9	YSO ⁵ , HII ¹⁷ , YSO-PE ²⁰ , PN ^{16,28} , YSO ⁹
J052123.85-683533.8	PN ^{5,7,16,28}	J054224.02-695305.1	PN ^{12,28}
J052142.85-683924.9	PN ^{7,16}	J054233.17-702924.1	O-PN ²⁹ , PN ^{7,16,28} , QSO ⁹
J052212.80-694329.1	PN ^{5,7,16,28} , YSO ⁹	J054236.65-700932.0	C-PN ²⁹ , PN ^{5,28}
J052235.20-682425.9	PN ^{7,16,28}		
J052240.97-711906.6	PN ^{5,7,16,28}	J054434.71-702140.7	PN ^{5,7,16,28} , YSO ⁹
J052331.11-690404.6	PN ^{5,7,10,16,28} , YSO ⁹	J054500.14-691819.1	PN ^{16,28} , Symb ¹⁹
J052348.66-691222.0	PN ^{7,16}	J054558.49-711903.9	Evolved ²⁸ , PN ¹⁰ , QSO ⁹
J052420.75-700501.3	PN ^{5,7,10,16,28} , YSO ⁹	J054704.54-692733.9	O-PN ²⁹ , PN ^{5,28}
J052427.26-702223.9	PN ^{7,16} , QSO ⁹	J054938.74-691000.1	PN ^{7,16}
J052455.07-713256.3	PN ^{5,7,16,28}		

Notes: The column "Previous identifications" gives the result of a positional cross-matching that was done with the catalogues mentioned in Table 4. Catalogue identifications: YSO = young stellar object, YSO-PE = YSO with PAH emission features and fine-structure lines, YSO-P = YSO with PAH emission features YSO-hp = high probability YSO candidate, G = background galaxy, QSO = quasi-stellar object, Evolved = evolved object, LPV = long period variable, PN = planetary nebula, C-PN = carbon-rich PN, O-PN = oxygen-rich PN, LPV/HII = long period variable/ HII region, EclBin = eclipsing binary, C = carbon star, Symb = Symbiotic, RRLab = RR Lyrae, UNK = object of unknown type. See catalogue references for full details of the individual object identification.

APPENDIX B: OBJECTS WITHOUT B AND I MAGNITUDES

In this section, we present the group of 85 objects, from the sample of 581 possible post-AGB/post-RGB and YSO candidates with confirmed LMC membership, which did not have both B and I magnitudes. These objects were fed into the STP (see Subsection 6.1) and their stellar parameters (T_{eff} , $\log g$, and $[\text{Fe}/\text{H}]$) were determined, but there were not enough data points to estimate the value of $E(B - V)$ that minimised the sum of the squared differences between the de-reddened observed and the intrinsic B , V , I and J magnitudes and therefore derived the reddening. We have removed this sample of 85 objects from further analysis and we carried forth the analysis with a sample of 496 possible post-AGB/post-RGB and YSO candidates. In Table B1 we present a list of these 85 objects along with their derived T_{eff} , $\log g$, $[\text{Fe}/\text{H}]$, the V band magnitude, the observed luminosity (L_{ob}), and the estimated radial velocity.

Table B1: The observational and stellar parameters for the 85 objects without B and V magnitudes.

Name	T_{eff} (K)	$\log g$	[Fe/H]	V (mags)	$(L_{\text{ob}}/L_{\odot})$	RV (km/s)
Candidates with [Fe/H] estimates from spectra						
J045034.50-701550.1	4500	0.50	-0.83	15.81	1216	244 ± 5
J045129.24-694648.7	4929	2.07	-1.02	18.10	198	200 ± 5
J045304.87-694106.0	5617	2.93	-0.91	18.16	188	181 ± 20
J045835.30-700350.0	5250	3.50	0.50	99.99	109	211 ± 4
J045906.08-675154.7	7632	2.00	-2.50	99.99	84	319 ± 15
J045931.59-701223.7	6179	3.21	-2.50	17.23	208	250 ± 20
J050131.83-704046.2	5546	2.23	-2.50	18.16	244	286 ± 18
J050247.50-703452.4	5386	2.17	-2.50	17.82	266	288 ± 16
J050504.78-675128.6	4500	1.42	-0.70	17.50	404	253 ± 5
J050906.53-710305.3	9520	2.00	0.09	17.96	226	213 ± 11
J050931.87-682935.4	7626	3.50	0.50	17.27	175	231 ± 20
J050939.63-710549.1	4759	2.46	-0.71	18.02	194	251 ± 9
J051109.63-723719.8	5611	3.38	-2.50	99.99	141	285 ± 14
J051200.73-692150.9	5747	3.00	-1.24	17.47	348	240 ± 6
J051255.05-713628.7	4633	2.17	-2.07	18.08	144	177 ± 12
J051305.83-682625.5	5119	3.50	-0.59	17.54	235	241 ± 12
J051427.55-720447.5	5053	1.50	-2.50	99.99	85	249 ± 6
J051529.30-684129.4	4500	1.87	-0.94	16.86	619	301 ± 5
J051551.41-723107.7	4500	1.00	-1.29	17.78	350	258 ± 3
J051616.97-693248.8	5733	2.98	-0.45	18.11	130	262 ± 5
J051712.18-690309.4	5938	1.00	-2.50	17.52	357	255 ± 7
J051825.71-700532.6	4500	1.71	-0.14	16.97	4614	255 ± 2
J051848.35-693334.7	5756	2.00	-1.13	17.92	4652	286 ± 8
J051853.31-730118.0	4500	1.40	-0.74	16.48	2134	209 ± 2
J051926.64-721604.2	5393	3.00	-2.50	99.99	246	241 ± 19
J052002.01-703017.0	5546	2.12	-2.50	16.25	761	210 ± 15
J052108.47-691158.8	4850	1.82	-1.71	17.66	206	250 ± 8
J052214.24-715731.2	4500	1.93	-0.46	17.01	1530	250 ± 2
J052242.48-672330.4	7222	4.00	-0.73	18.08	94	260 ± 19
J052300.09-701831.8	4288	0.58	-1.68	17.86	233	264 ± 9
J052338.56-724600.5	4500	2.00	-1.13	18.12	9149	239 ± 4
J052444.03-695619.5	4757	1.83	-0.60	18.00	312	263 ± 5
J052744.65-710033.8	4750	2.65	-1.87	17.49	148	174 ± 7
J052756.36-700434.0	4500	1.16	-1.08	17.62	824	246 ± 8
J052816.85-693017.0	8246	1.00	0.50	17.61	9045	275 ± 3
J052856.67-674237.3	5620	1.88	-2.13	17.98	135	212 ± 17
J052906.64-682013.3	5075	2.29	-2.50	17.37	519	234 ± 10
J052918.18-702516.4	5439	2.28	-0.94	99.99	64	274 ± 8
J053024.31-704555.8	10809	2.00	0.50	99.99	143	265 ± 16
J053108.81-701759.4	5865	2.59	-1.53	99.99	189	289 ± 8
J053136.67-710650.8	10500	2.00	0.50	16.74	632	277 ± 1
J053140.01-710911.0	5774	2.50	-2.50	15.29	967	266 ± 20
J053246.45-671028.3	7628	3.50	0.50	99.99	372	195 ± 13
J053255.47-672944.4	5606	3.00	-2.50	99.99	455	180 ± 22
J053327.17-700951.5	4867	2.00	-1.17	18.00	8371	276 ± 6
J053447.57-715908.0	4500	1.69	-1.04	99.99	396	262 ± 2
J053545.26-705720.8	6900	3.50	0.50	18.17	102	230 ± 7
J053605.89-713053.5	4750	2.71	-0.55	99.99	63	287 ± 8
J053956.85-703214.6	5750	0.50	-1.62	99.99	4019	256 ± 13
J054024.67-702722.7	4500	1.58	-0.09	17.69	598	262 ± 1
J054046.53-704322.2	5656	0.50	-1.54	15.82	1002	269 ± 4
J054236.18-714621.5	4500	2.66	-1.50	17.88	123	338 ± 23
J054237.91-712917.0	6036	3.00	-1.21	17.89	201	367 ± 7
J054311.96-695808.6	11500	2.50	0.50	99.99	96	232 ± 18
J054354.82-693352.9	5248	3.00	-2.09	17.21	590	309 ± 13
J054506.60-710509.1	7626	4.00	-1.18	99.99	132	201 ± 10
J054643.30-701209.2	4628	1.00	-0.86	17.28	415	295 ± 6
J054738.16-695106.7	5799	3.00	-2.50	16.30	562	357 ± 9
J045451.08-700739.8	5518	3.50	-0.99	99.99	91	277 ± 17
J050823.36-691706.1	5222	2.64	-0.66	17.09	365	290 ± 6
J052738.69-705219.0	6009	0.97	-2.14	15.54	1806	278 ± 7
J052754.75-714036.4	4765	2.43	-0.36	99.99	98	264 ± 15
J053209.95-713117.2	6091	3.50	-0.82	99.99	161	261 ± 15
J054139.18-702208.2	5982	1.00	-0.89	17.15	465	253 ± 11

Table B1: continued.

Name	T_{eff} (K)	$\log g$	[Fe/H]	V (mags)	$(L_{\text{ob}}/L_{\odot})$	RV (km/s)
J054533.77-702126.6	5052	2.58	-0.62	17.52	283	273 ± 3
Candidates with [Fe/H] = -0.50						
J053241.04-695751.5	5005	2.16	-0.5	99.99	174	244 ± 4
J045239.31-711345.8	7500	3.0	-0.5	99.99	139	300 ± 8
J045338.12-695139.9	7253	3.5	-0.5	17.07	215	200 ± 14
J045537.16-661403.9	27947	3.5	-0.5	15.89	517	332 ± 10
J050151.70-703941.9	32178	4.63	-0.5	15.06	891	200 ± 21
J050414.05-701015.9	31000	4.24	-0.5	16.39	1931	284 ± 14
J050829.25-674232.5	7250	1.0	-0.5	99.99	209	289 ± 21
J051143.88-715105.7	12000	2.5	-0.5	17.29	199	323 ± 14
J052022.20-724604.3	6477	2.5	-0.5	99.99	124	285 ± 18
J052129.82-723148.1	7630	4.0	-0.5	99.99	119	236 ± 22
J052238.63-712206.5	10000	2.0	-0.5	16.42	608	316 ± 22
J052412.04-715449.9	7148	3.5	-0.5	99.99	252	282 ± 19
J052438.81-680653.9	10500	2.0	-0.5	18.13	126	287 ± 19
J053244.04-681131.6	7629	2.89	-0.5	99.99	73	348 ± 19
J054238.36-693324.6	6813	2.91	-0.5	99.99	68	276 ± 32
J054546.43-710225.1	10500	2.0	-0.5	99.99	149	265 ± 15
J054947.47-684636.5	7625	3.07	-0.5	99.99	116	269 ± 15
J055521.66-694235.1	8124	2.0	-0.5	99.99	118	302 ± 10
J053031.62-712257.7	7631	4.0	-0.5	99.99	105	295 ± 28
J054115.32-695809.9	8303	1.0	-0.5	99.99	849	282 ± 18

Notes: T_{eff} , $\log g$, and [Fe/H] are estimated using the STP (see Section 6.1). V is the optical V -band magnitude and L_{ob}/L_{\odot} is the observed luminosity (see Section 3). RV is the estimated heliocentric velocity (see Section 5).

**APPENDIX C: THE FINAL SAMPLE OF HIGH
PROBABILITY POST-AGB, POST-RGB AND
YSO CANDIDATES**

Figures C1 – C3 show the SEDs of the objects before and after de-reddening (see Section 8, for full details).

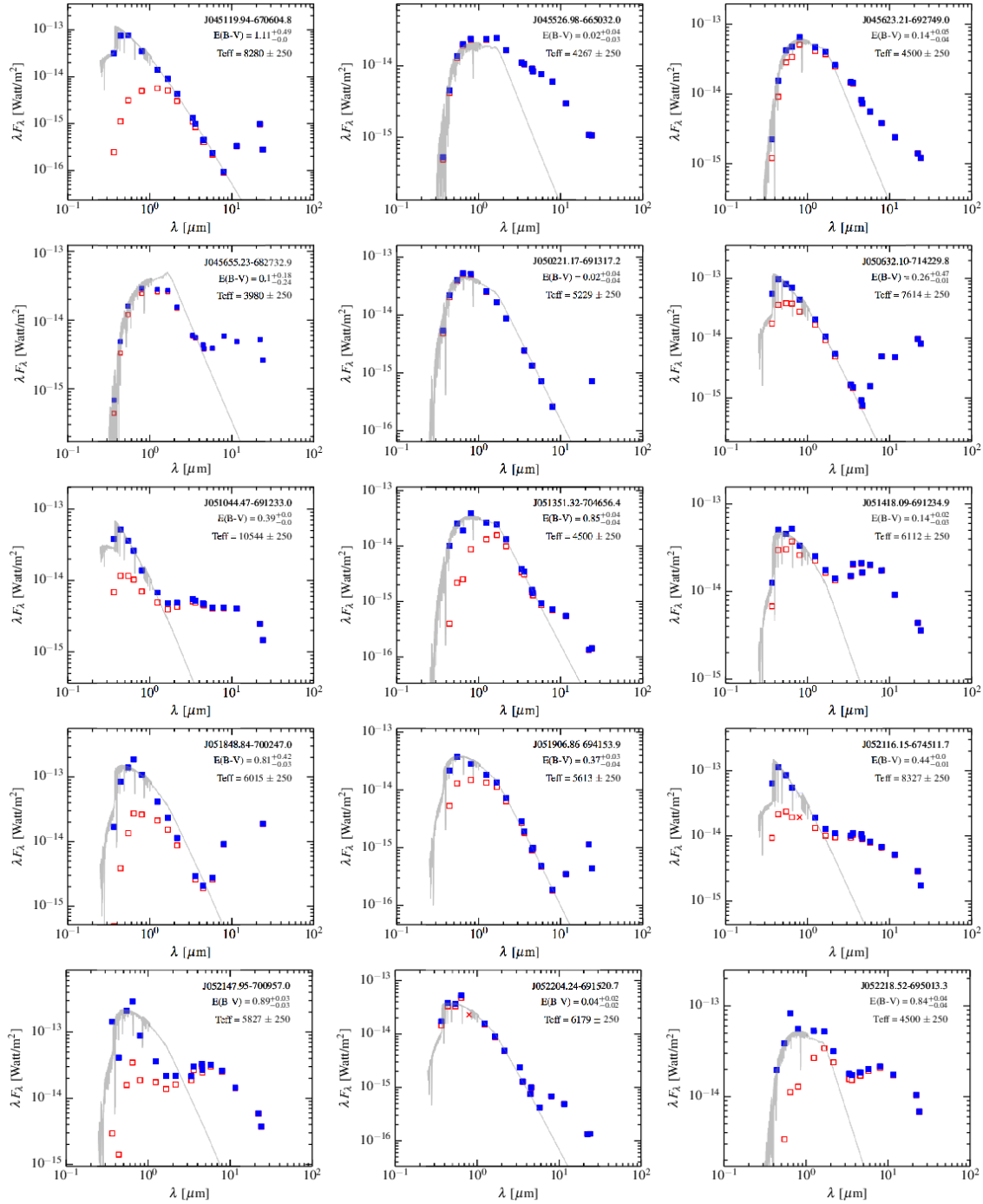


Figure C1. SEDs of the post-AGB candidates. The red open squares represent the original broadband photometry. The blue filled squares represent the dereddened broadband photometry. Up to a wavelength of 10500Å, we over-plot (grey solid-line) the flux-calibrated Munari synthetic spectrum which is estimated to have the best-fit to the observed spectra (see Section 6.1). From 10500Å onwards we over-plot the corresponding low-resolution flux distribution from from the corresponding appropriate ATLAS9 atmospheric model (Castelli & Kurucz 2004). The SED plots also show the name of the individual object, the estimated $E(B-V)$ value with error bars (see Section 6.2) and the estimated T_{eff} value.

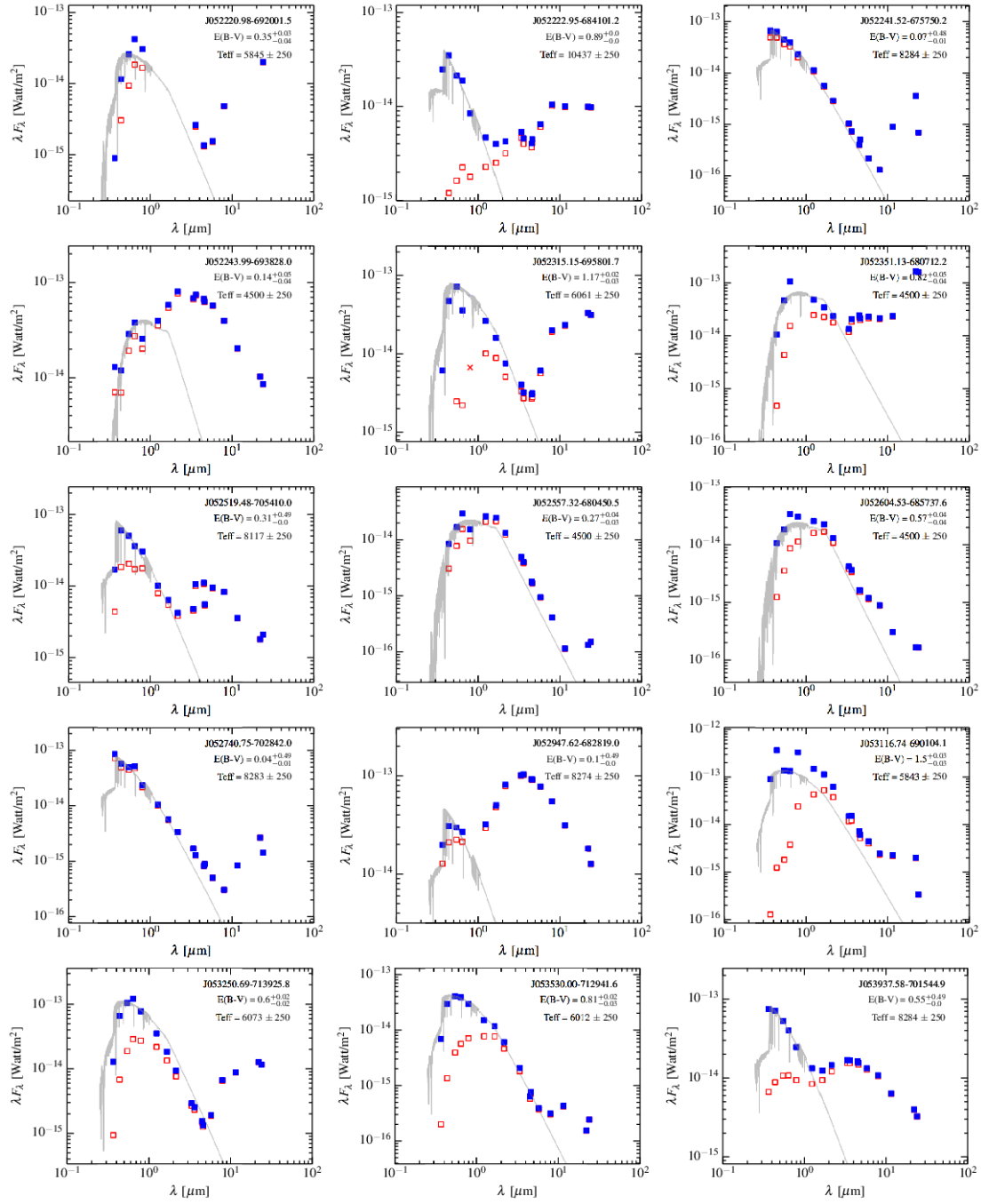


Figure C1. Figure C1 continued.

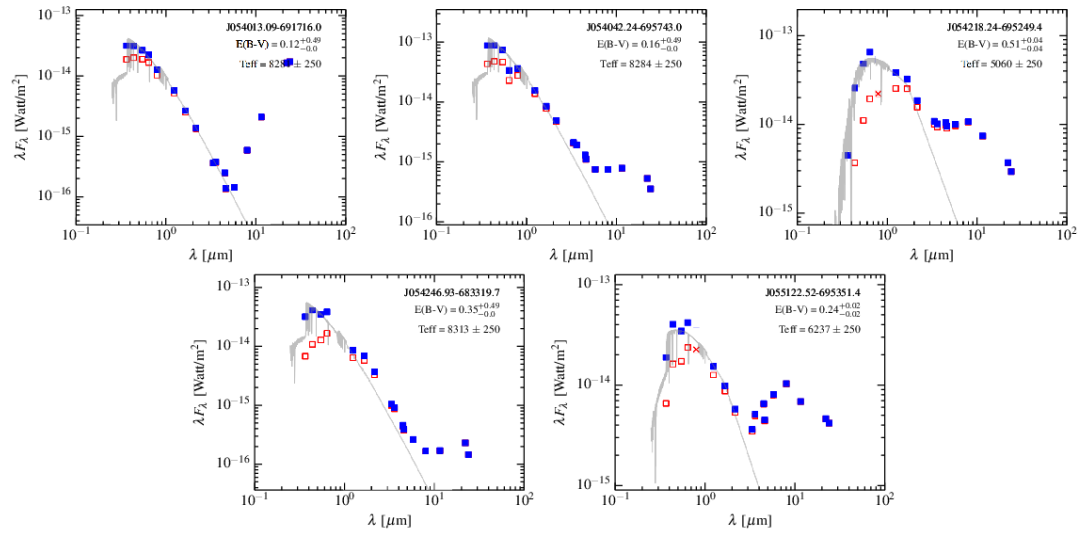


Figure C1. Figure C1 continued.

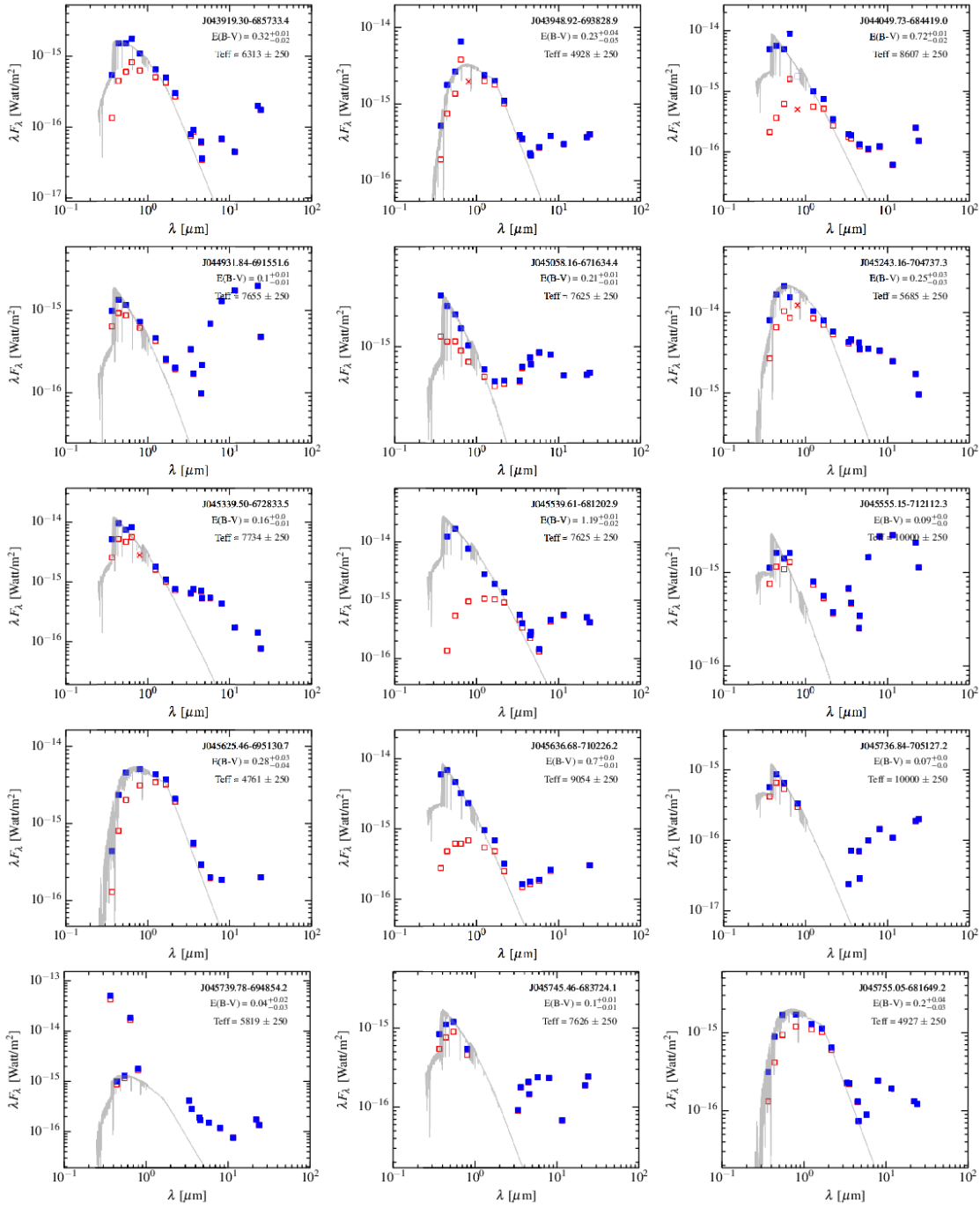


Figure C2. Same as Figure C1, but for the post-RGB candidates.

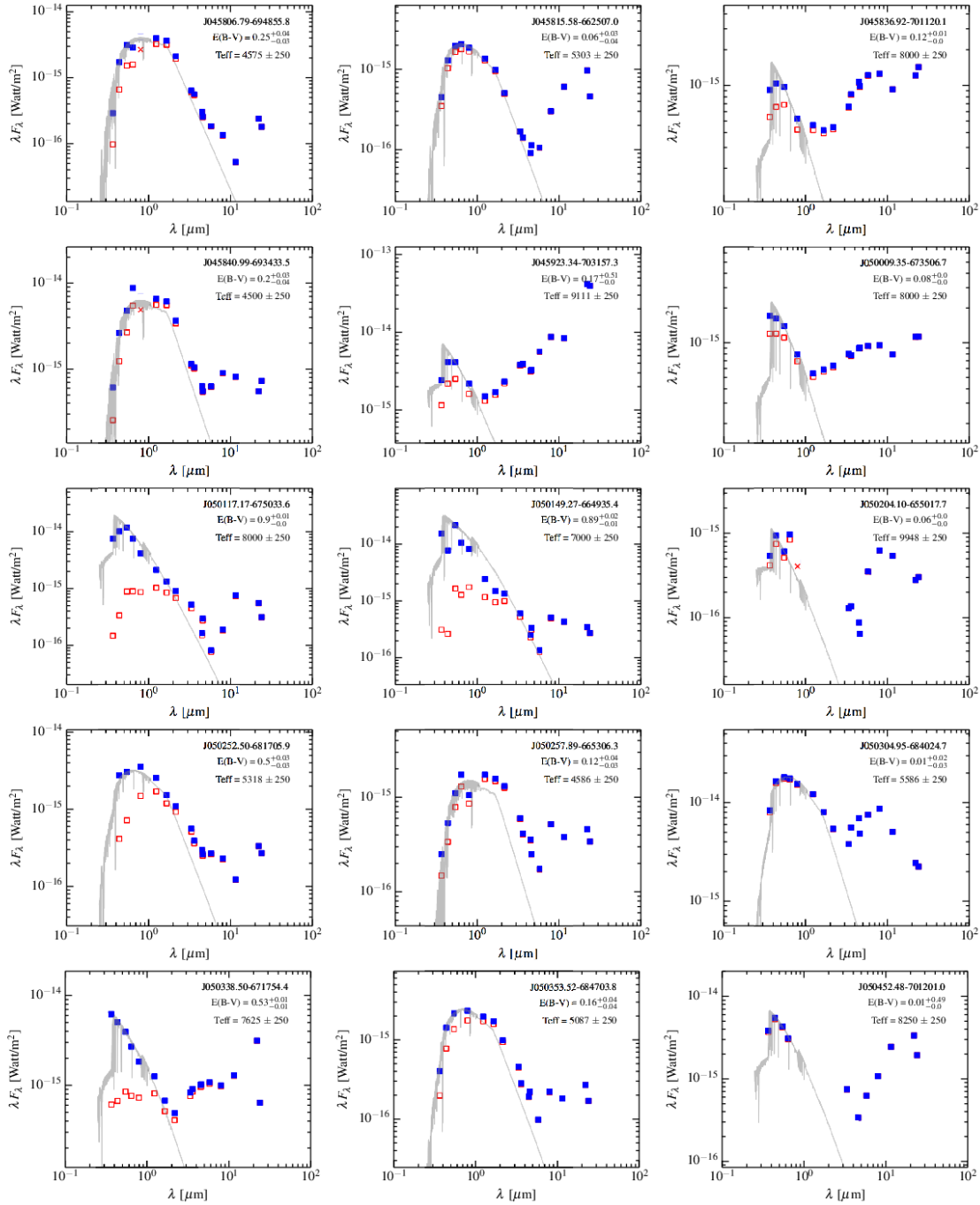
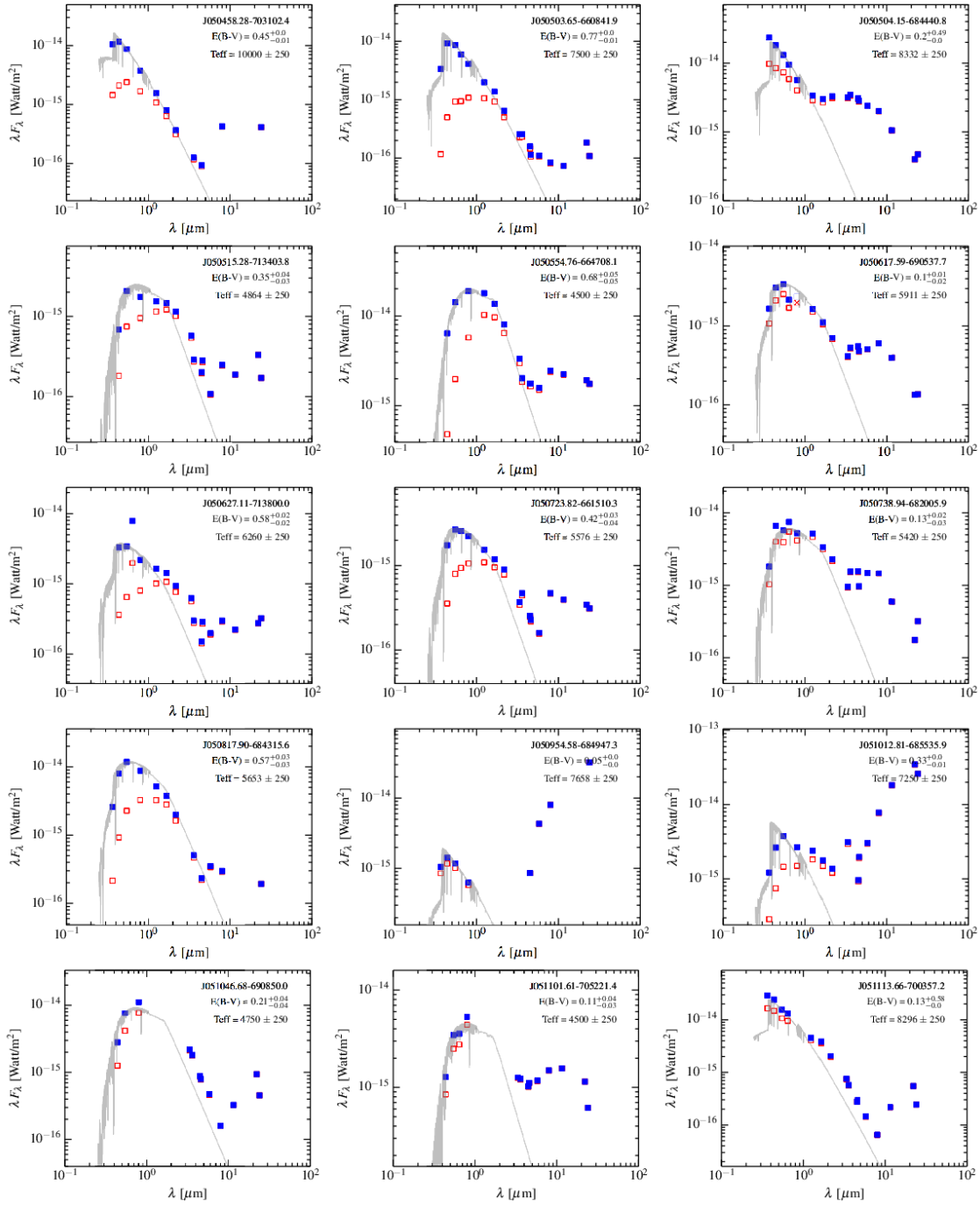


Figure C2. Figure C2 continued.



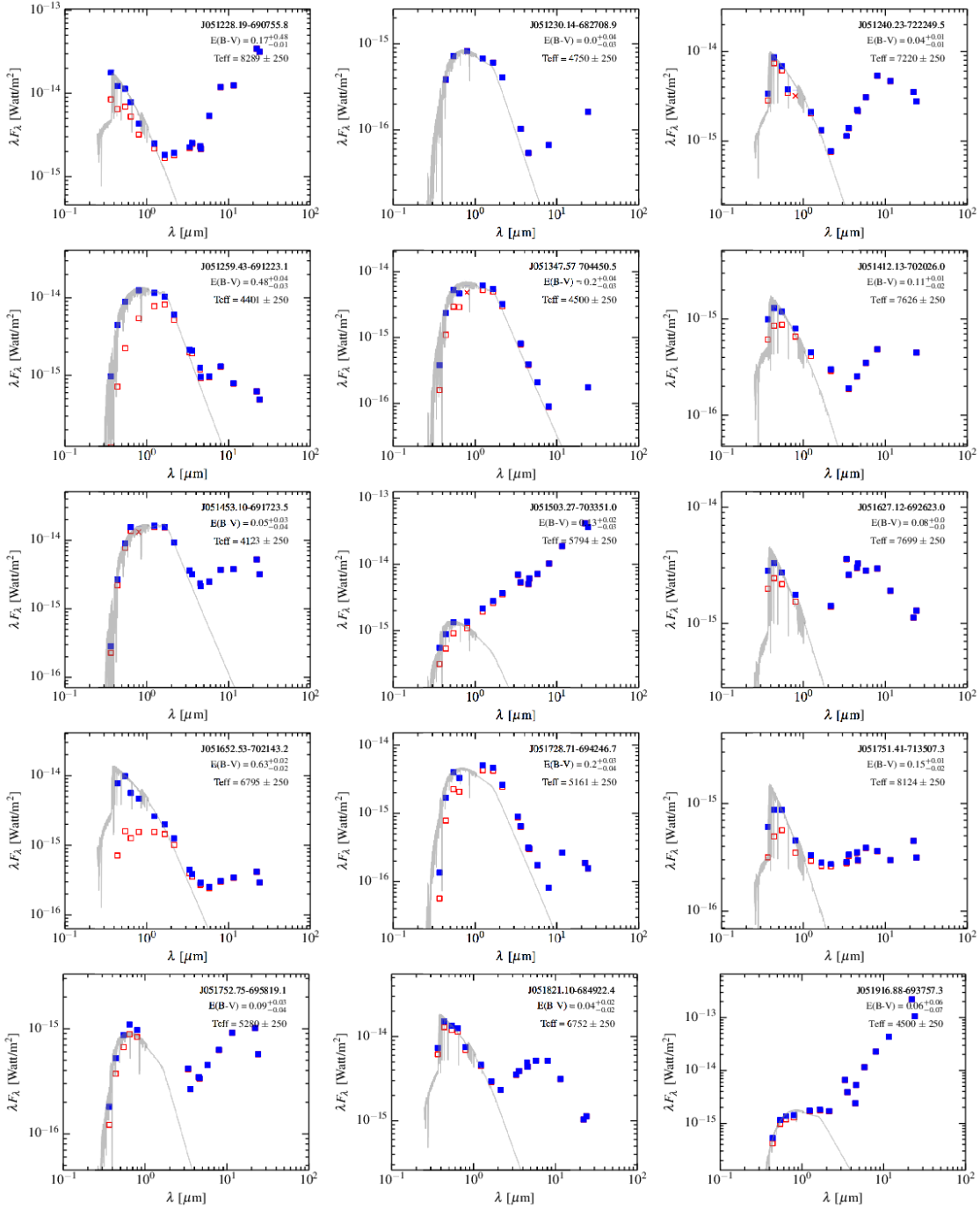


Figure C2. Figure C2 continued.

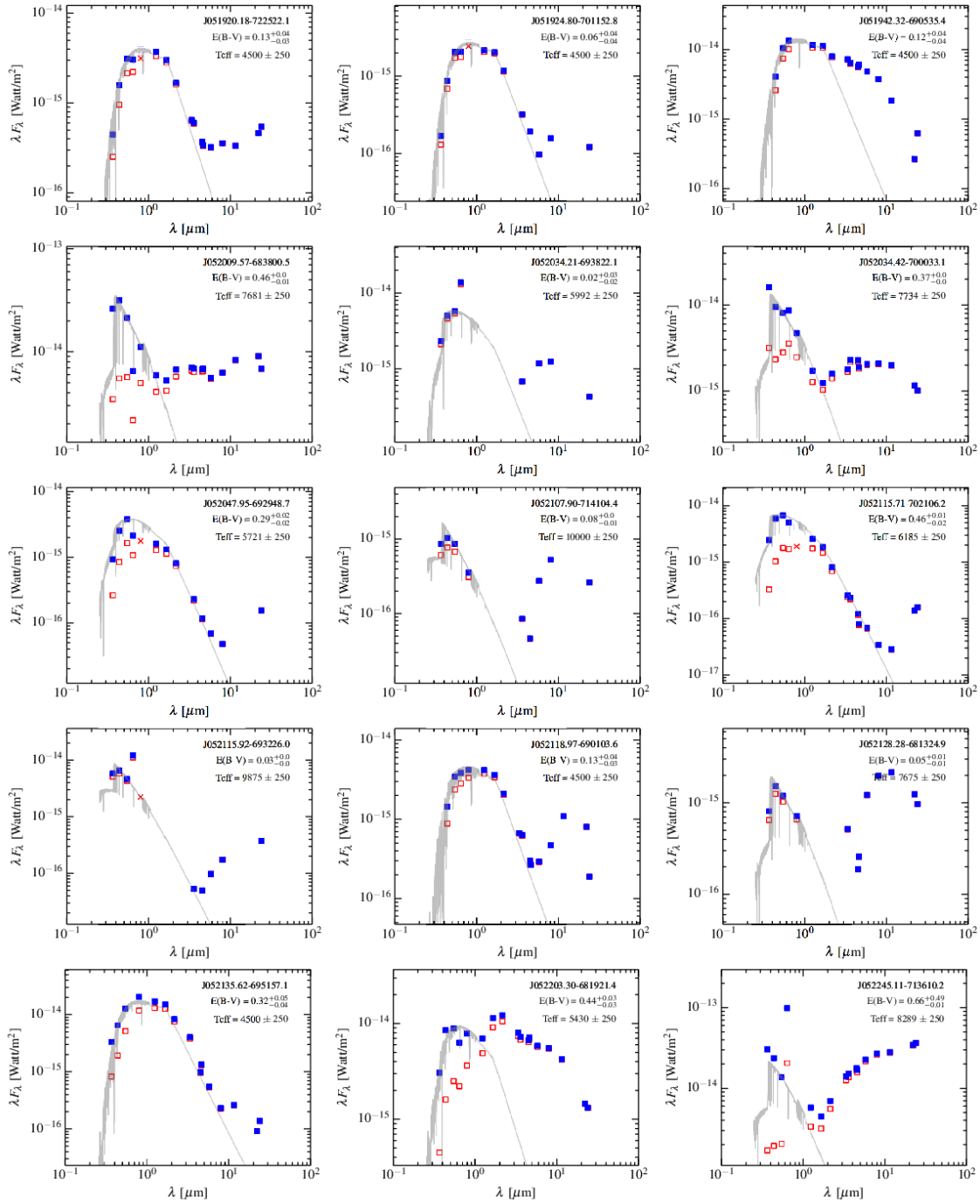


Figure C2. Figure C2 continued.

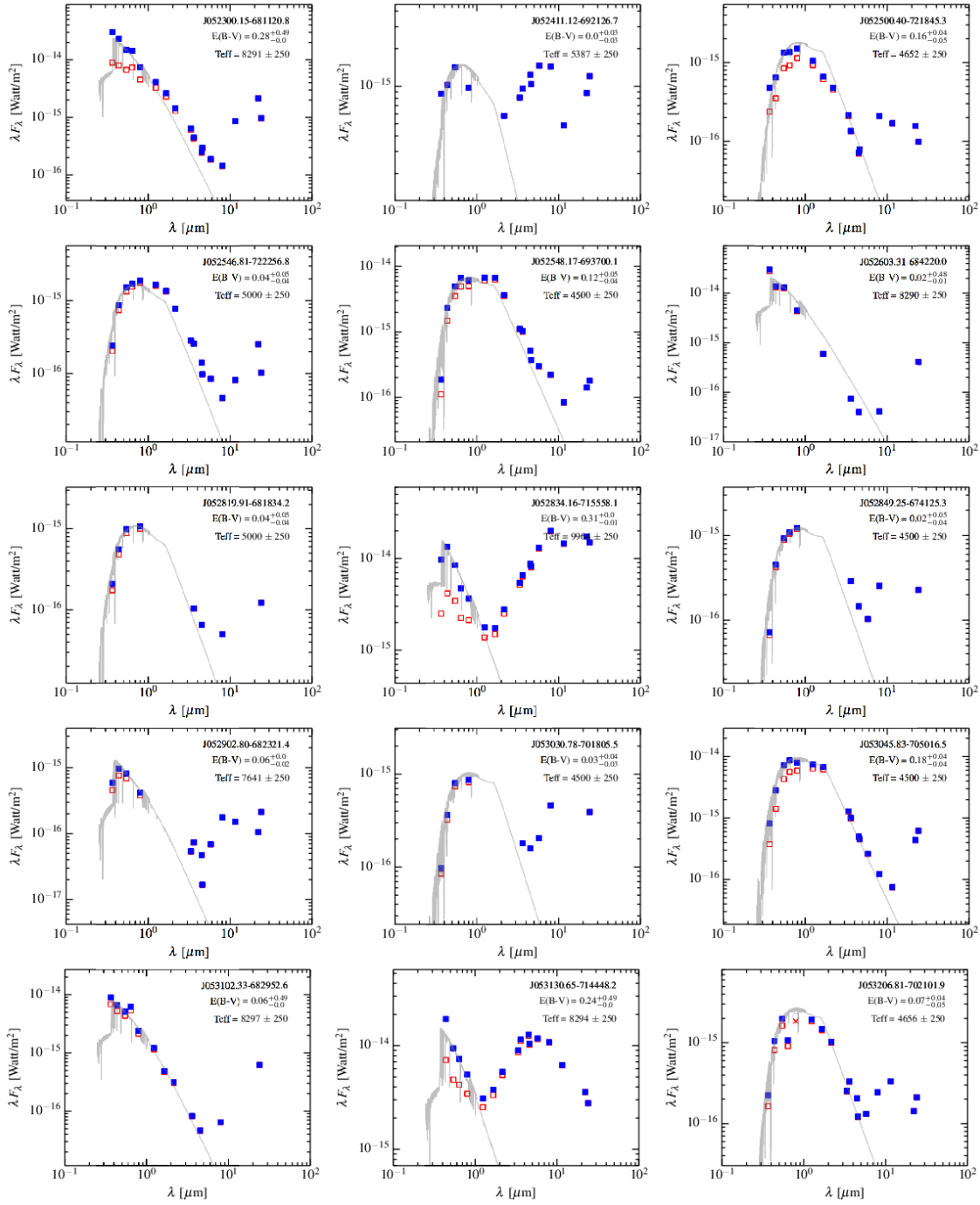


Figure C2. Figure C2 continued.

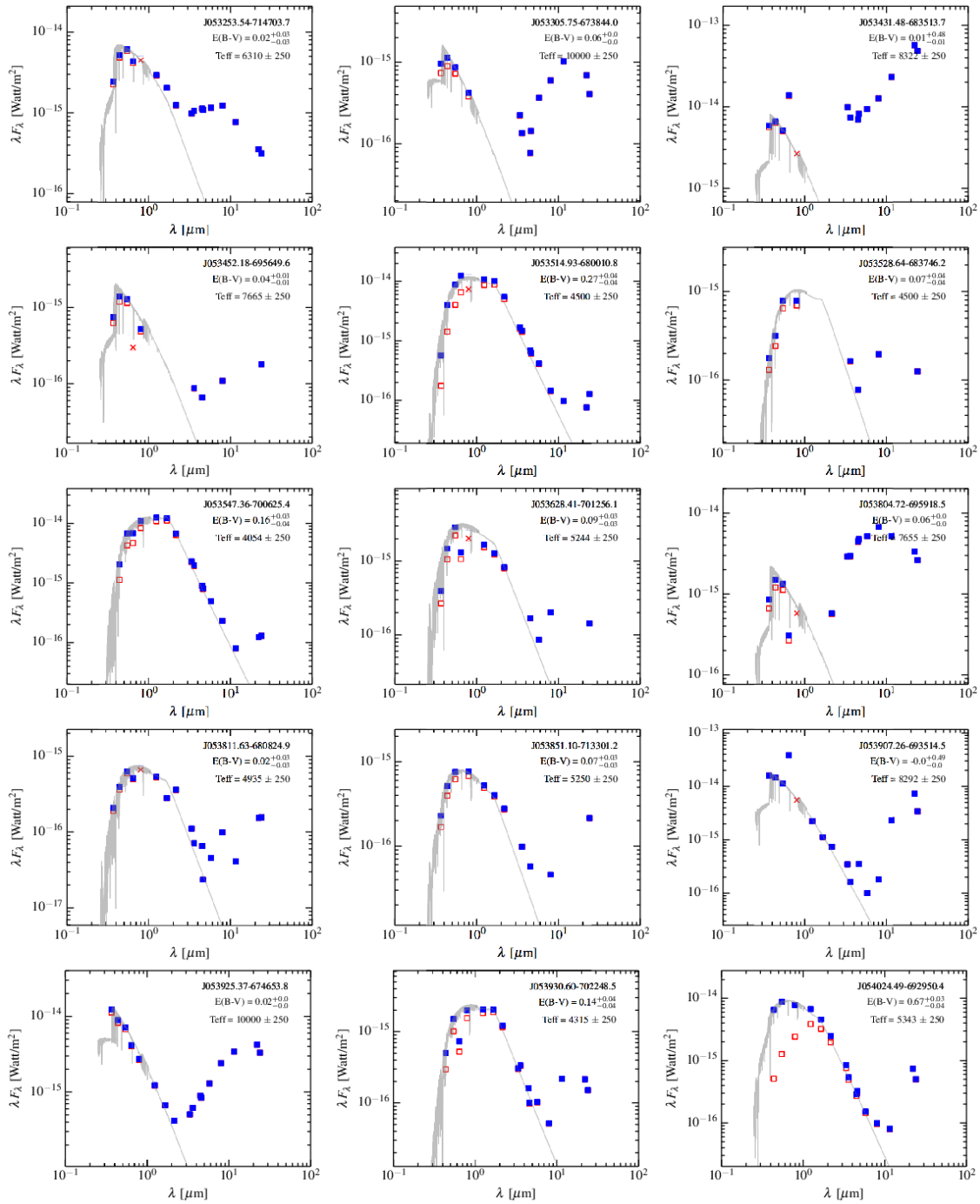


Figure C2. Figure C2 continued.

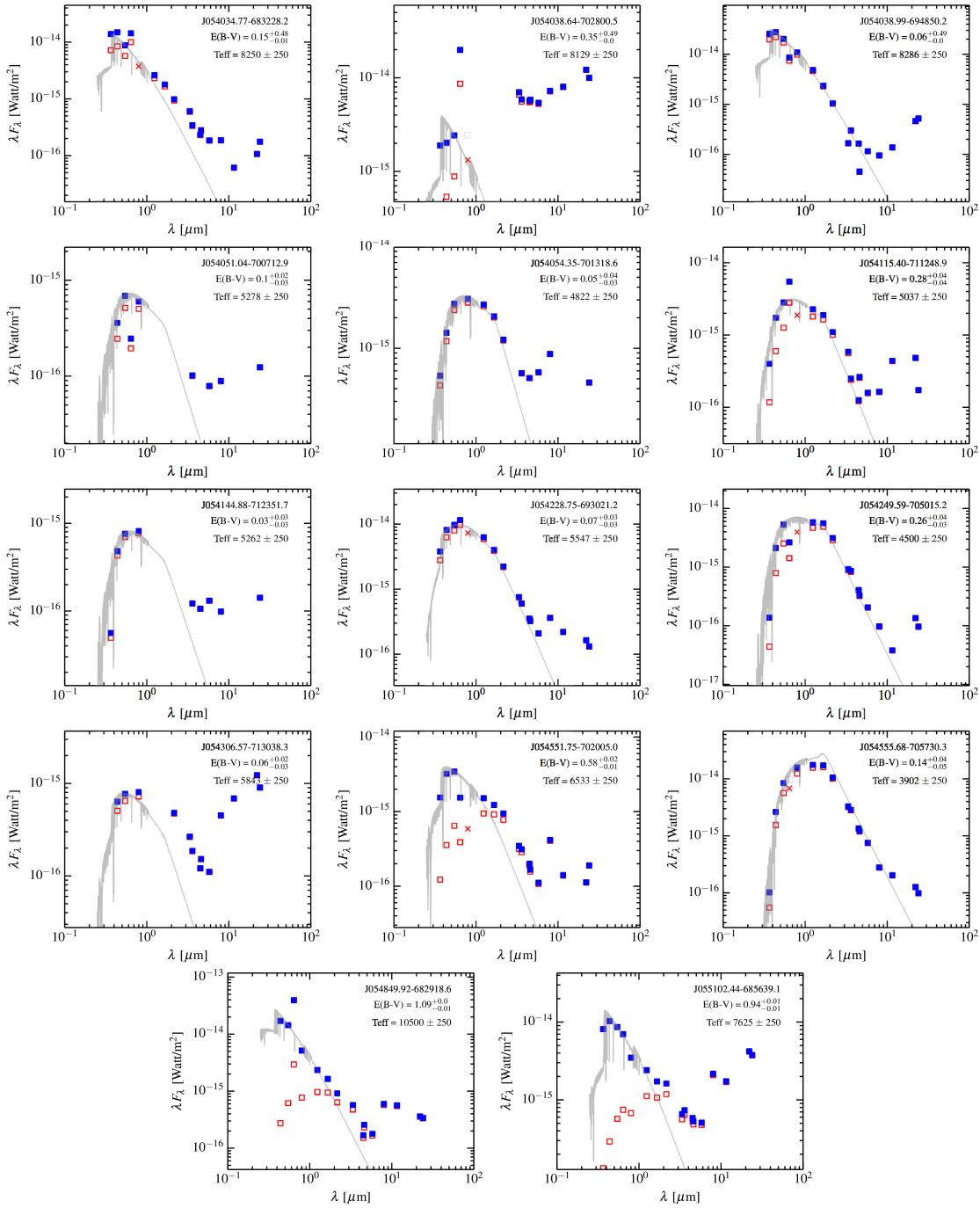


Figure C2. Figure C2 continued.

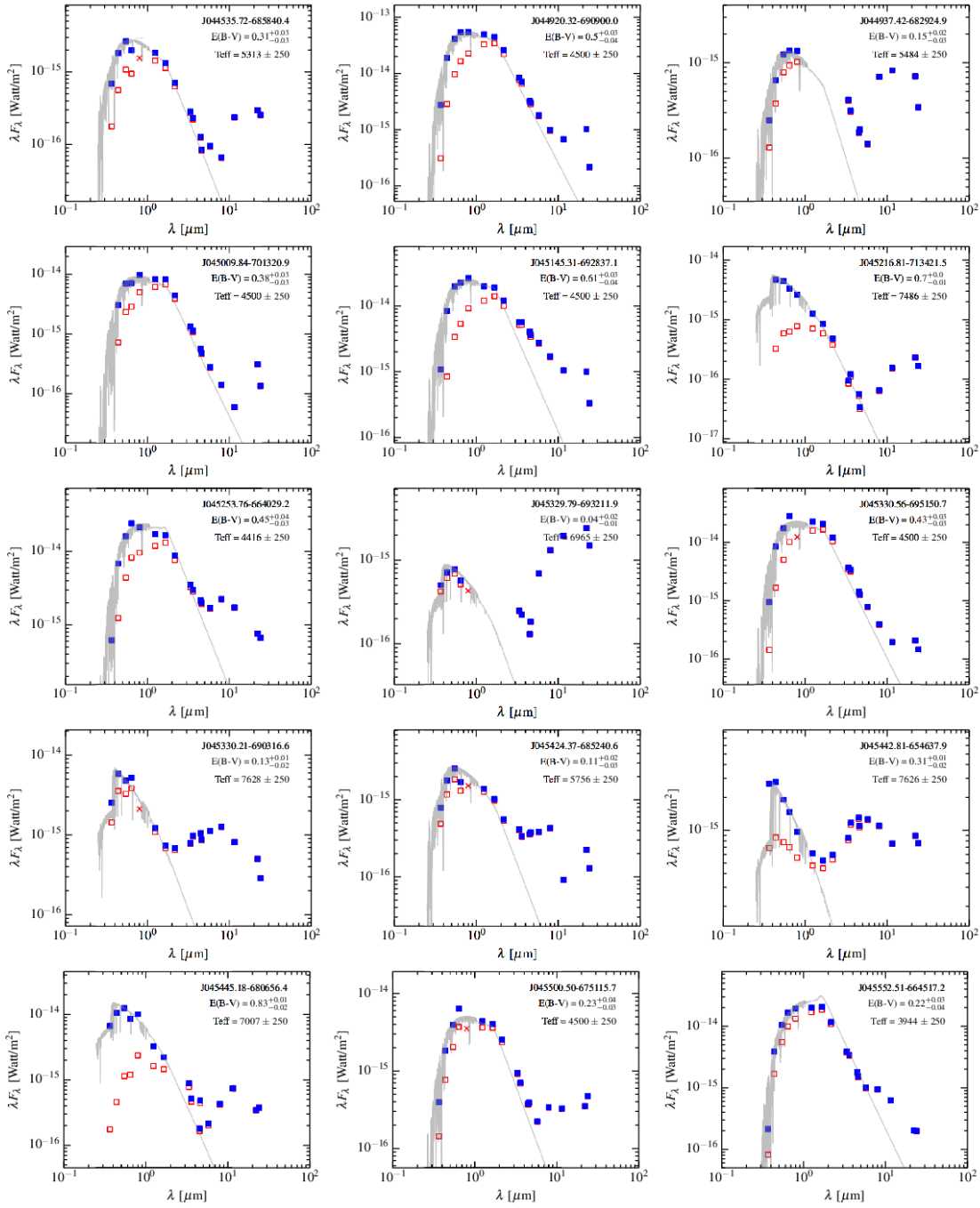


Figure C3. Same as Figure C1, but for the YSO candidates

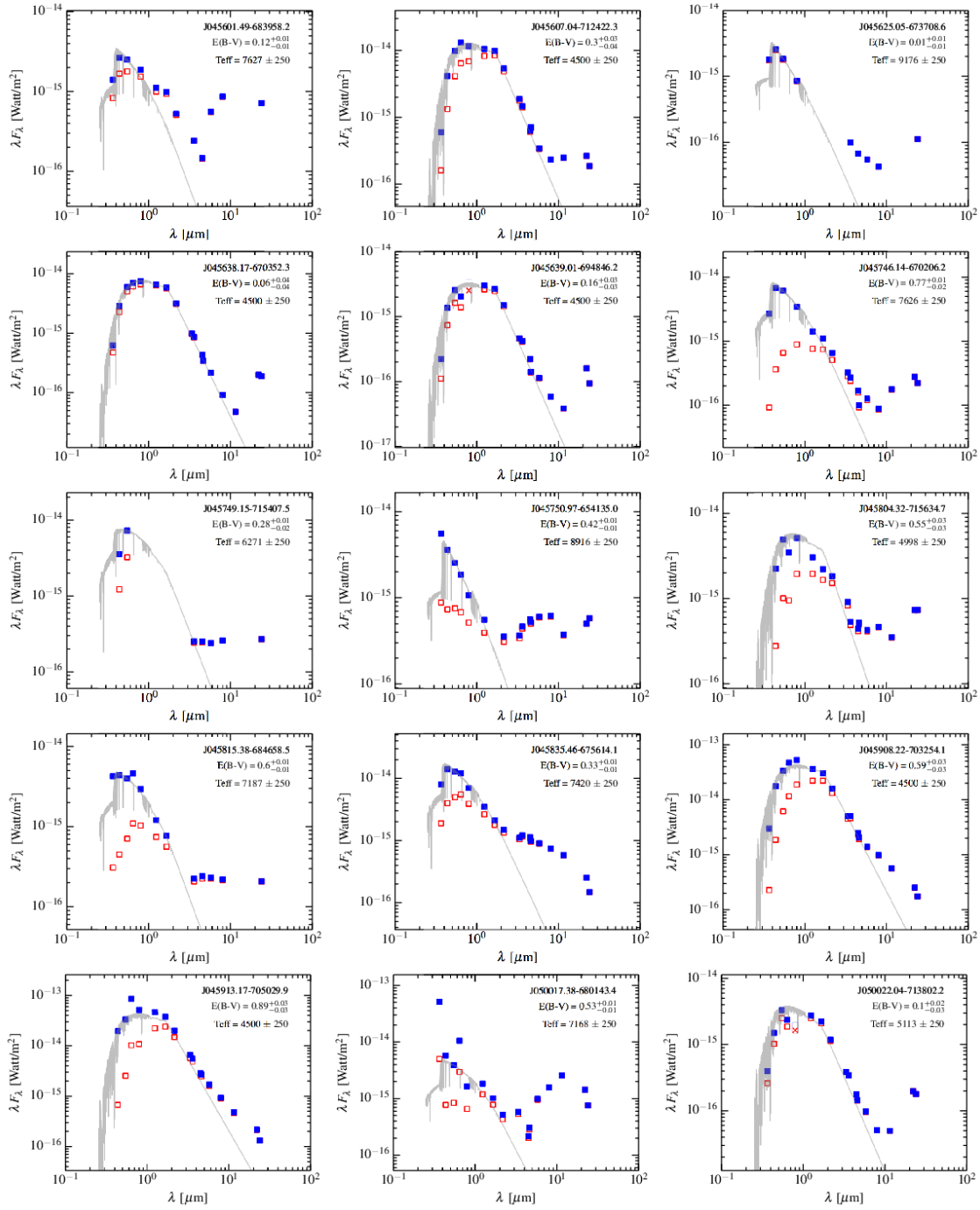


Figure C3. Figure C3 continued.

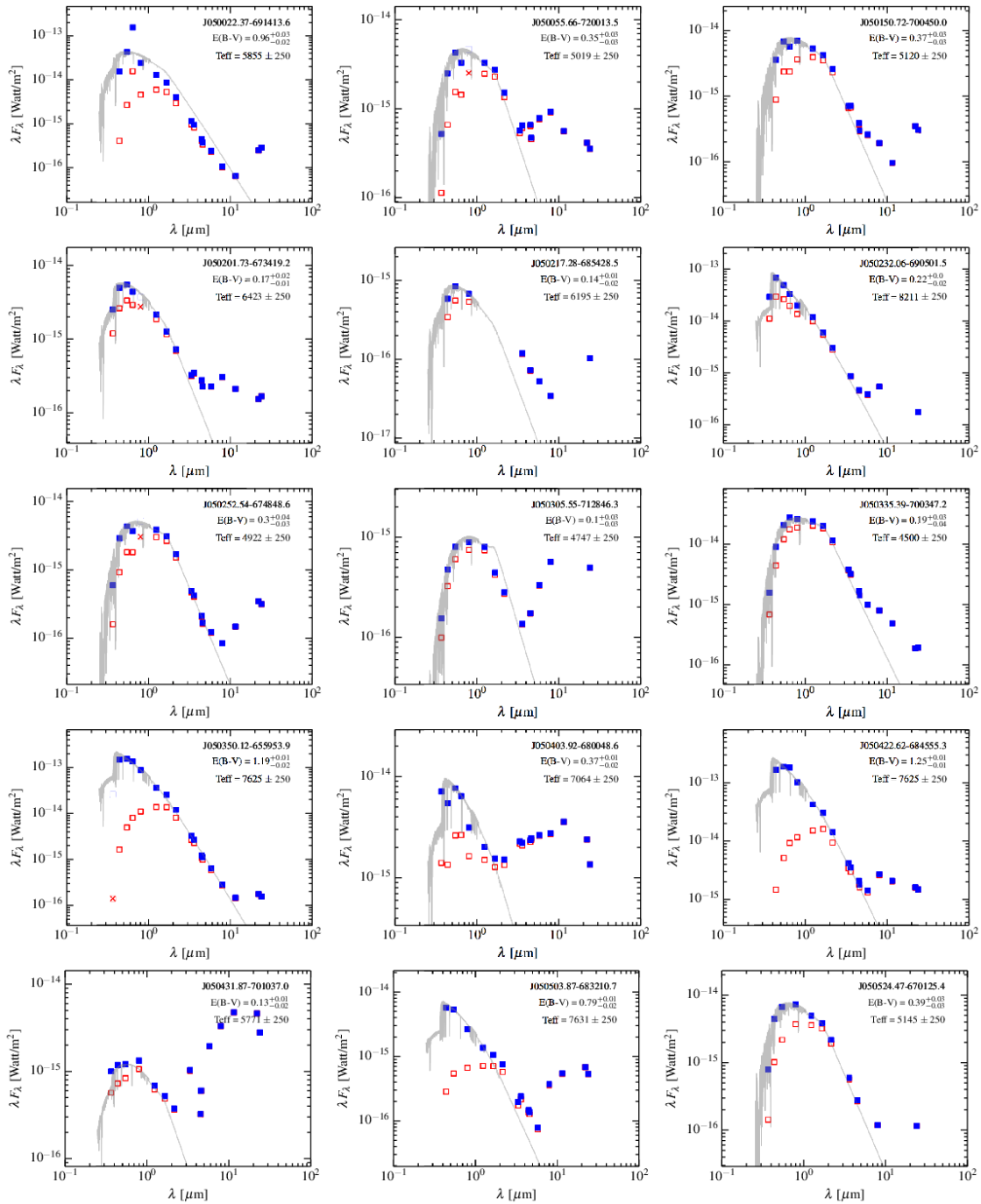


Figure C3. Figure C3 continued.

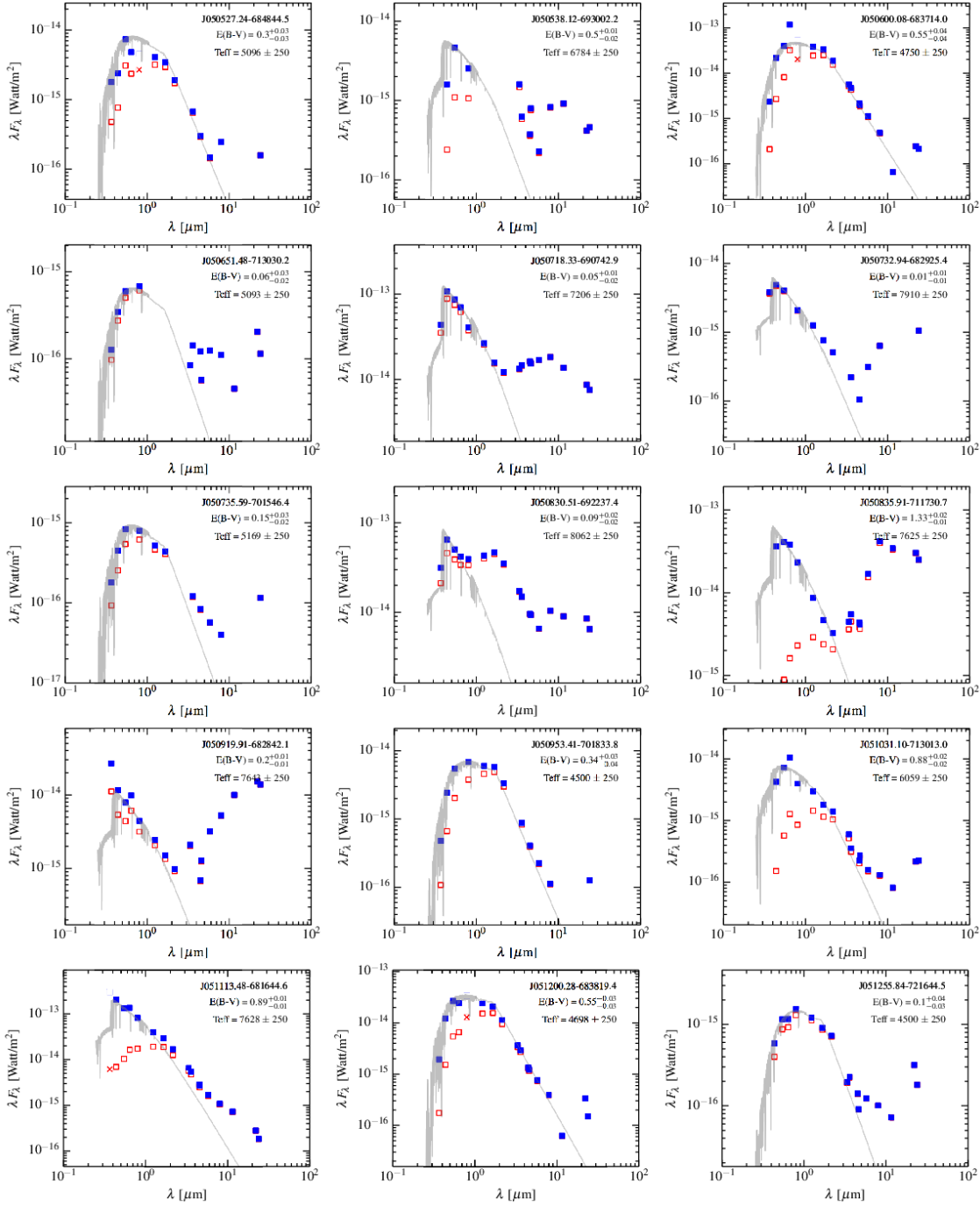


Figure C3. Figure C3 continued.

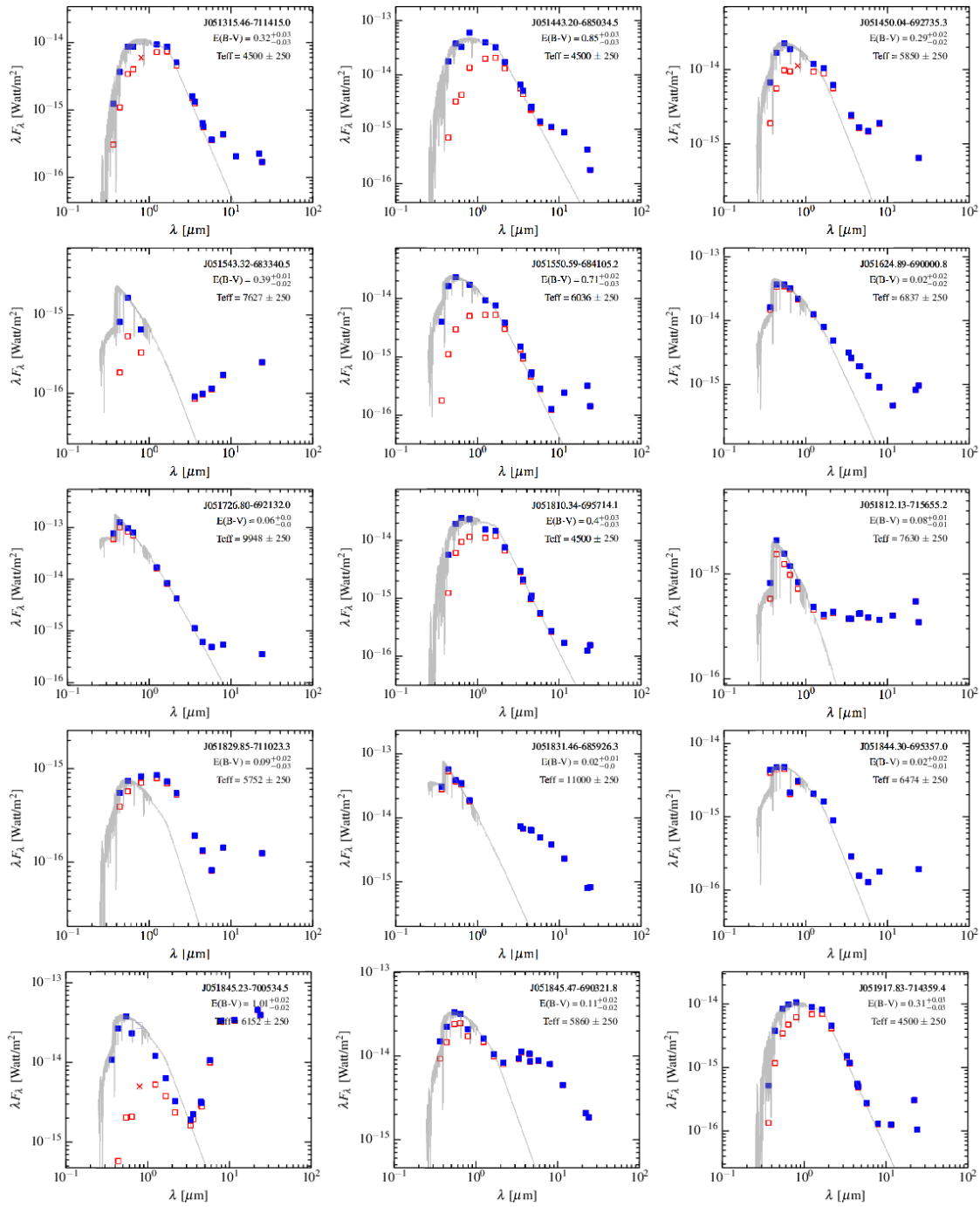


Figure C3. Figure C3 continued.

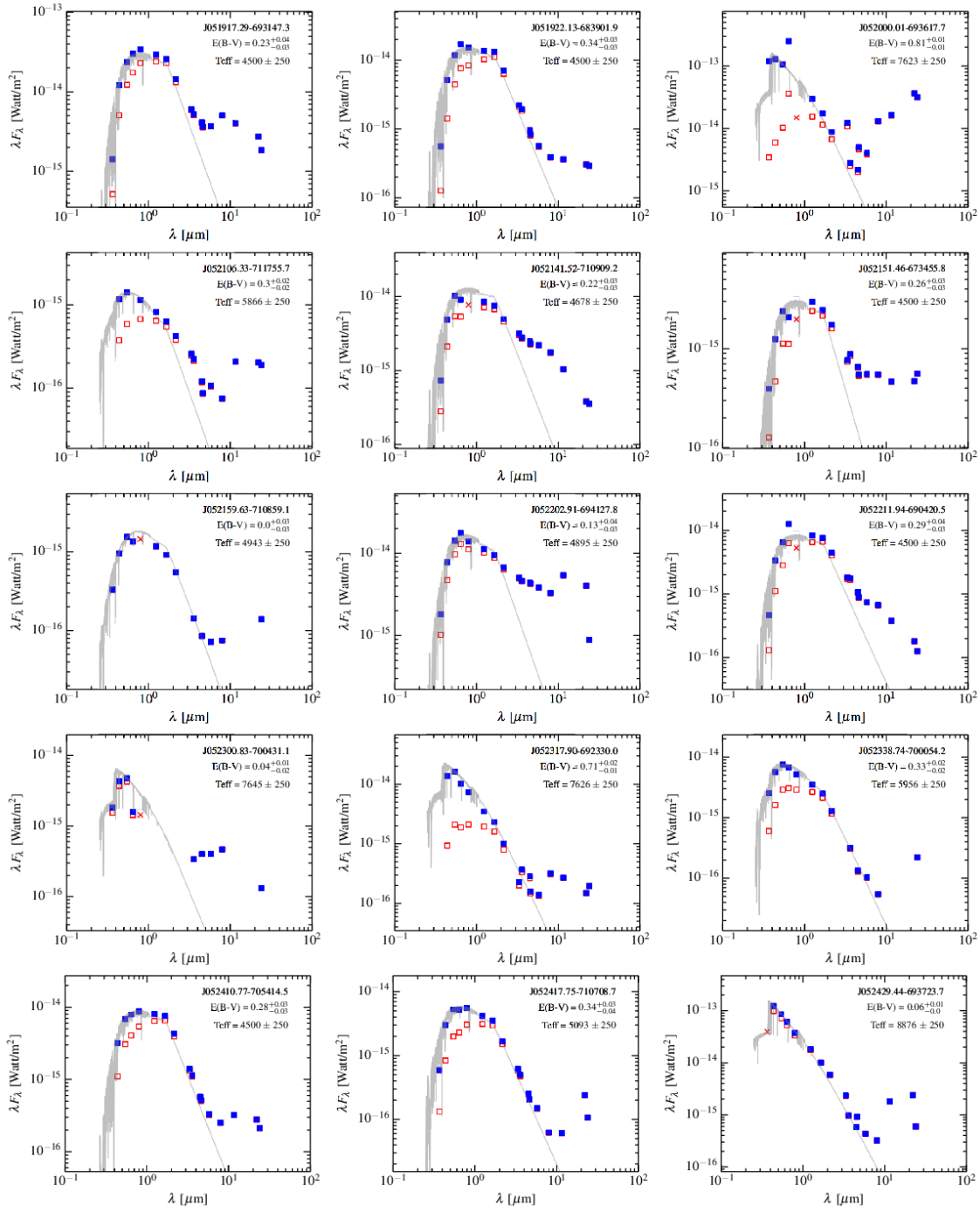


Figure C3. Figure C3 continued.

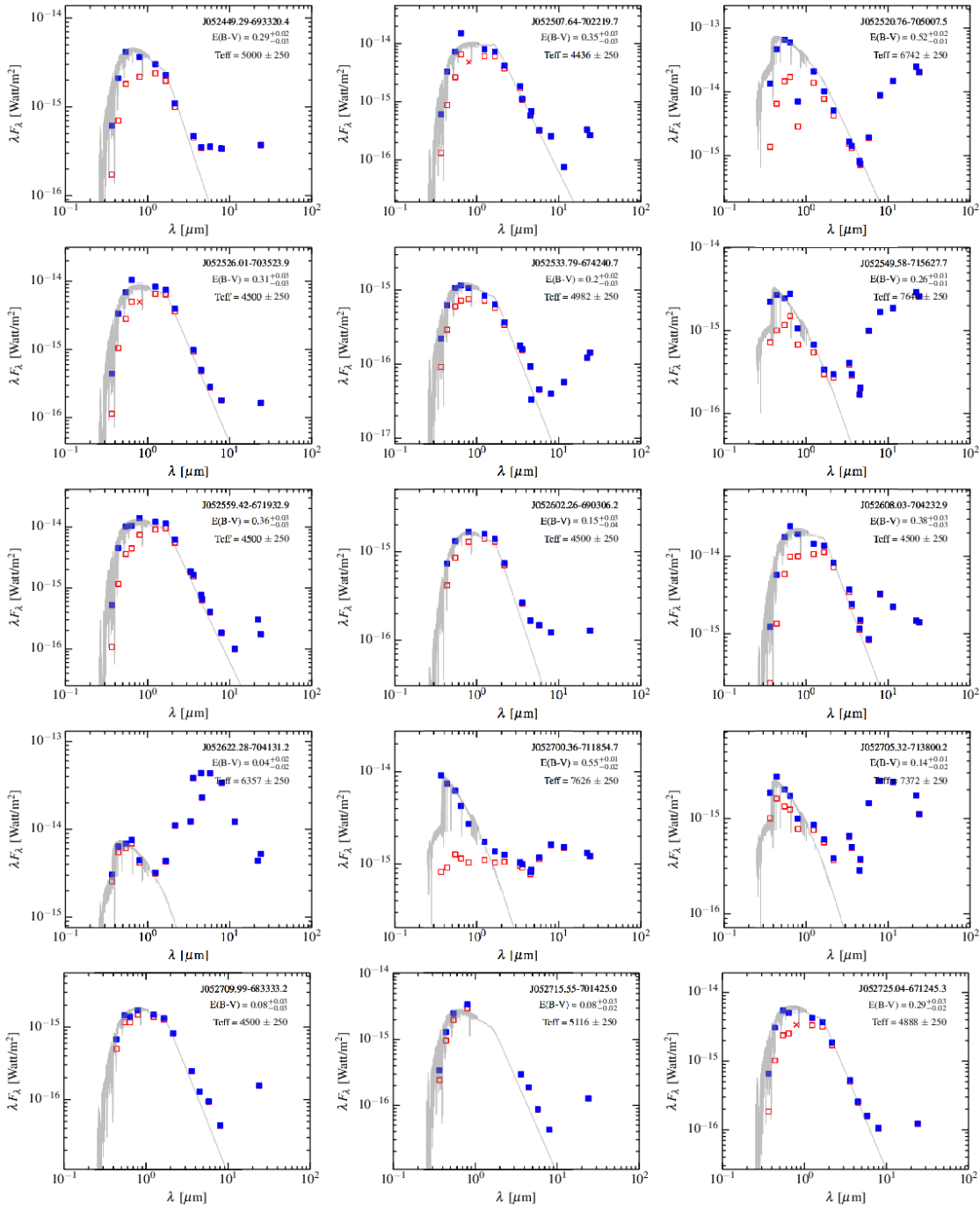


Figure C3. Figure C3 continued.

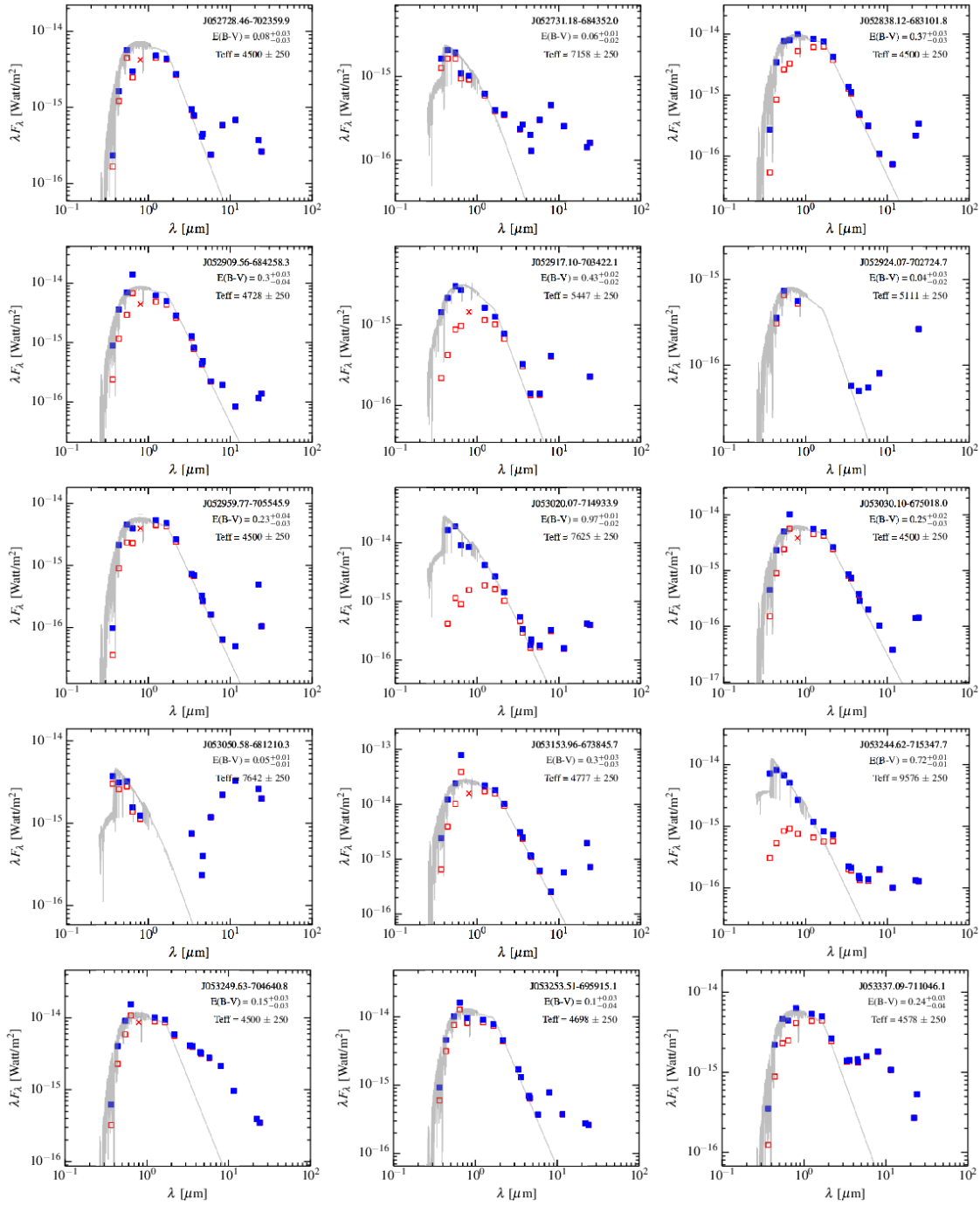


Figure C3. Figure C3 continued.

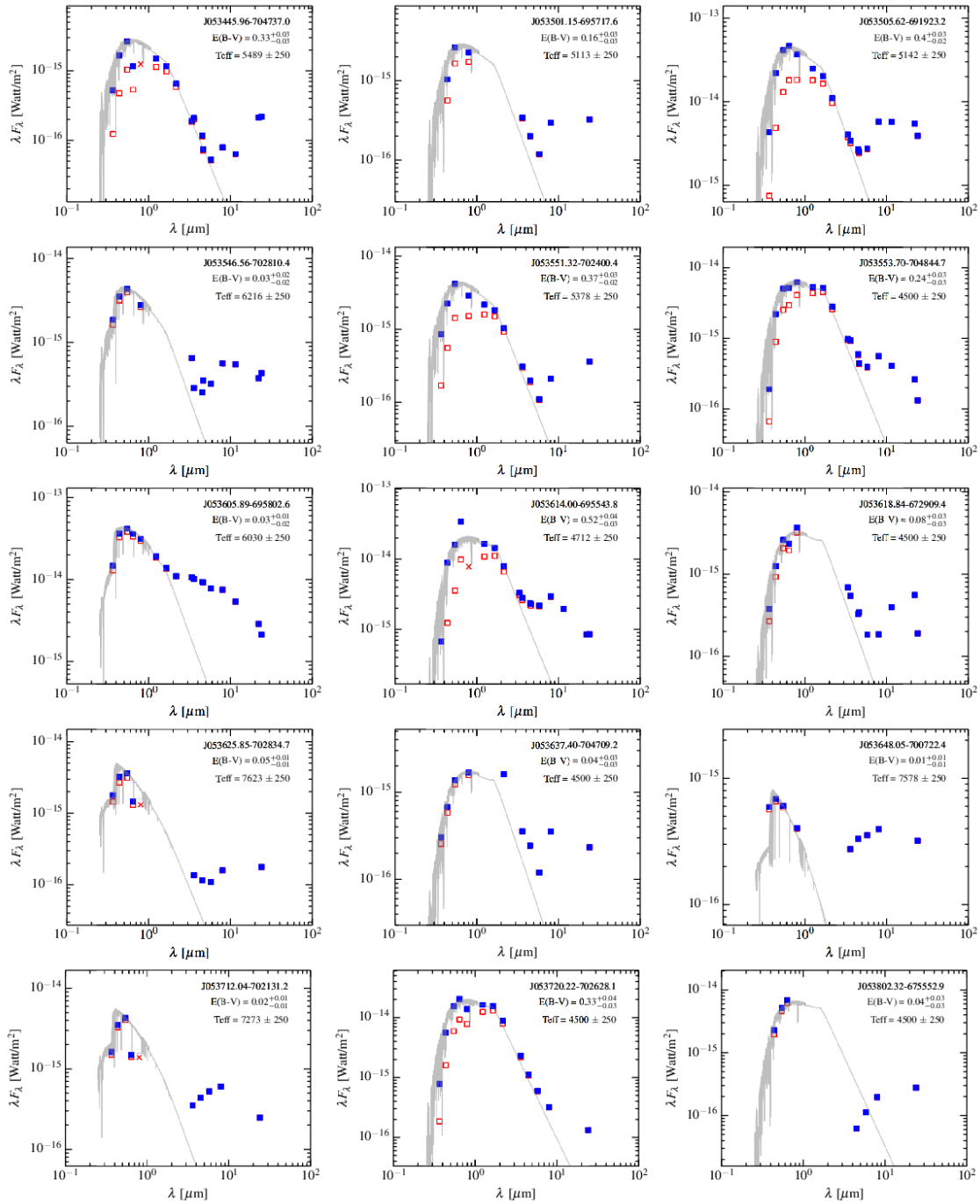


Figure C3. Figure C3 continued.

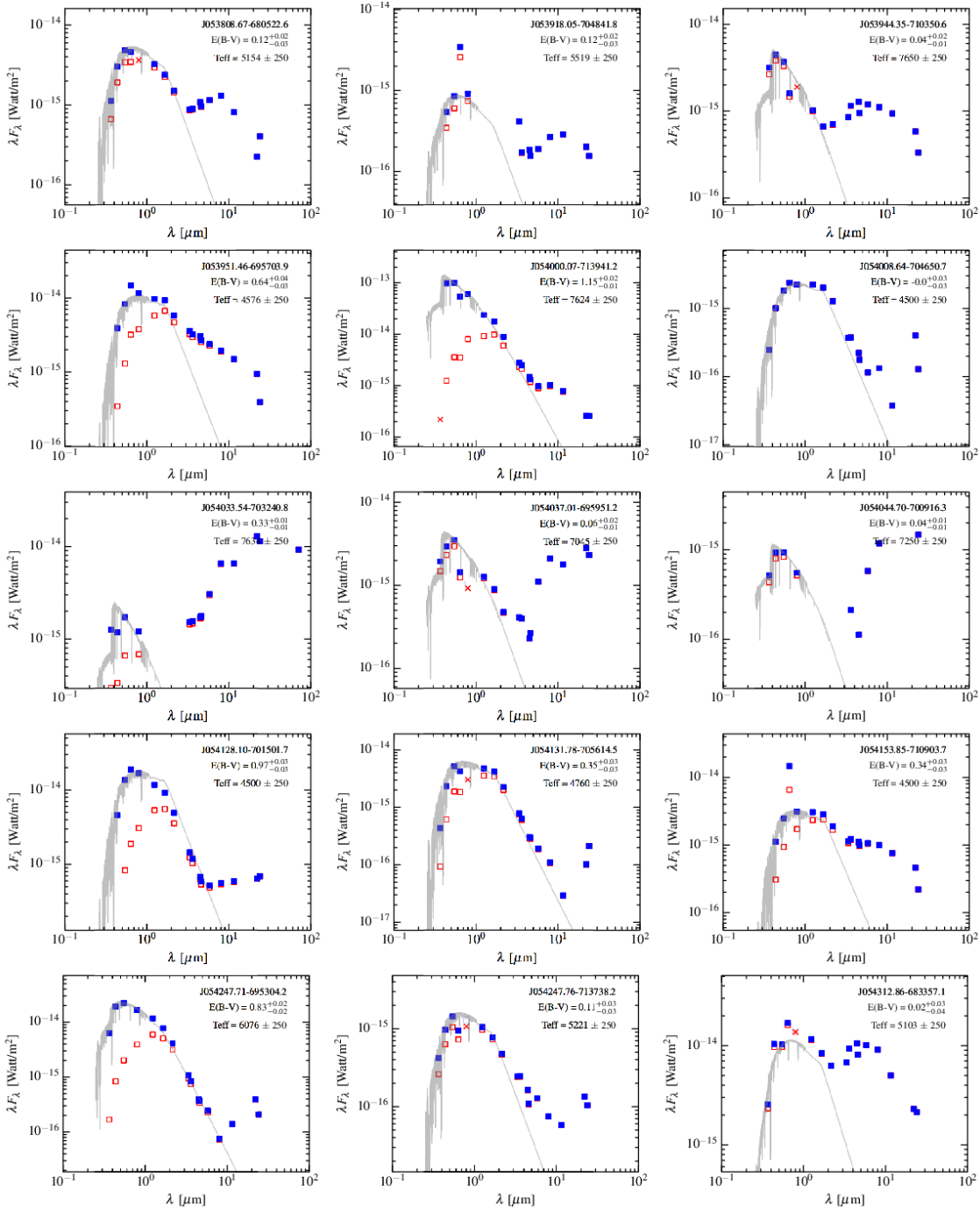


Figure C3. Figure C3 continued.

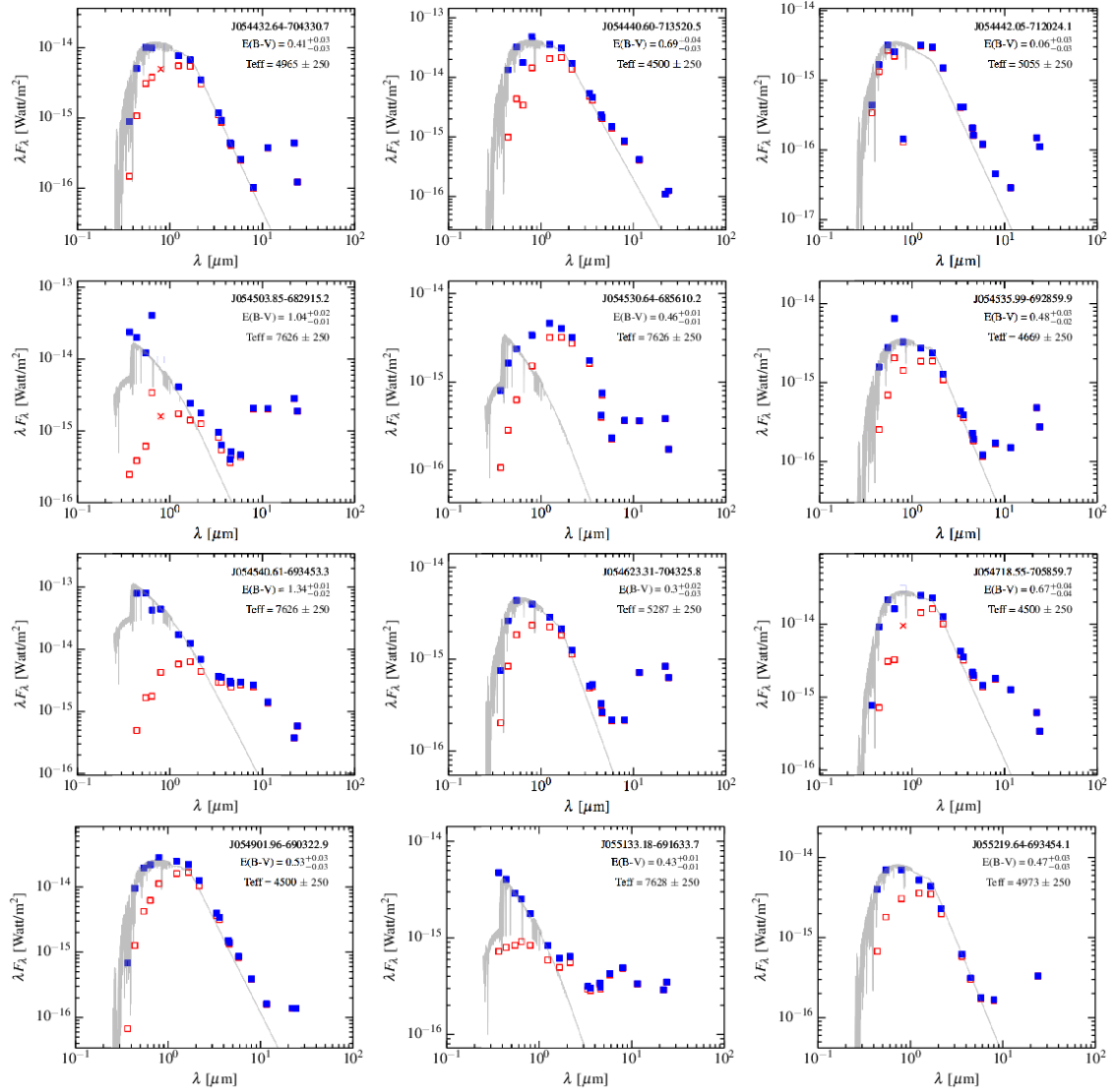


Figure C3. Figure C3 continued.